

DEVELOPMENT AND IMPLEMENTATION OF NOVEL FLOW CONTROL
TECHNIQUES FOR NONSLENDER DELTA WINGS

A THESIS SUBMITTED TO
THE GRADUATE SCHOOL OF NATURAL AND APPLIED SCIENCES
OF
MIDDLE EAST TECHNICAL UNIVERSITY

BY

ALPER ÇELİK

IN PARTIAL FULFILLMENT OF THE REQUIREMENTS
FOR
THE DEGREE OF DOCTOR OF PHILOSOPHY
IN
MECHANICAL ENGINEERING

JUNE 2017

Approval of the thesis:

**DEVELOPMENT AND IMPLEMENTATION OF NOVEL FLOW CONTROL
TECHNIQUES FOR NONSLENDER DELTA WINGS**

submitted by **ALPER ÇELİK** in partial fulfillment of the requirements for the degree of **Doctor of Philosophy in Mechanical Engineering Department, Middle East Technical University** by,

Prof. Dr. Gülbin Dural Ünver
Dean, Graduate School of **Natural and Applied Sciences**

Prof. Dr. R. Tuna Balkan
Head of Department, **Mechanical Engineering**

Assoc. Prof. Dr. Mehmet Metin Yavuz
Supervisor, **Mechanical Engineering Dept., METU**

Examining Committee Members:

Assoc. Prof. Dr. Cüneyt Sert
Mechanical Engineering Dept., METU

Assoc. Prof. Dr. M. Metin Yavuz
Mechanical Engineering Dept., METU

Assoc. Prof. Dr. Oğuz Uzol
Aerospace Engineering Dept., METU

Assoc. Prof. Dr. Selin Aradağ Çelebioğlu
Mechanical Engineering Dept., TOBB-ETÜ University

Asst. Prof. Dr. Ekin Özgirgin Yapıcı
Mechanical Engineering Dept., Çankaya University

Date: 22.06.2017



I hereby declare that all information in this document has been obtained and presented in accordance with academic rules and ethical conduct. I also declare that, as required by these rules and conduct, I have fully cited and referenced all material and results that are not original to this work.

Name, Last name: Alper ÇELİK

Signature :

ABSTRACT

DEVELOPMENT AND IMPLEMENTATION OF NOVEL FLOW CONTROL TECHNIQUES FOR NONSLENDER DELTA WINGS

Çelik, Alper

PhD, Department of Mechanical Engineering

Supervisor : Assoc. Prof. Dr. Mehmet Metin Yavuz

June 2017, 181 pages

Understanding and controlling the physical phenomenon behind the aerodynamics of low to moderate swept delta wings has been a challenge for researchers during the last few decades, which is stimulated by their widespread use in unmanned combat air vehicles (UCAVs) and micro air vehicles (MAVs). Although delta wings are capable of generating high lift and stable flight performance at high angle of attack, the problems related to lack of conventional flow control surfaces compel the researchers to explore new means of flow control techniques on delta wings. In the current study, it is aimed to control the flow structure of low swept delta wing with sweep angle of $\Lambda=45^\circ$ using novel passive flow control techniques. The experiments are conducted in a low speed wind tunnel using the techniques of laser-illuminated flow visualization, surface pressure measurements, and particle image velocimetry (PIV). Three different passive flow control methods are developed and investigated including bioinspired edge modification, bioinspired material modification, and passive bleeding, where the details of each are described in the paragraphs below.

Bioinspired edge modifications are studied based on similarities between delta wing shapes and cetacean flukes. Reynolds number is varied within the range of

$10^4 < Re < 2.5 \times 10^4$ and the attack angles are $4 \leq \alpha \leq 12$. The results indicate that the edge modification deteriorates the flow structures compared to the base wing planform within the operational range tested in the current study.

Passive bleeding, using the inherent pressure difference between the suction and pressure side of the wing, is studied to investigate its effect on the flow structure of a 45 deg swept delta wing. Three different bleeding configurations are tested to identify the effectiveness of the control technique for a broad range of attack angles $6 \leq \alpha \leq 16$ deg at Reynolds numbers $10^4 < Re < 10^5$. The results indicate that all bleeding configurations alter the flow field over the planform, where a proper bleeding induces significant improvement on the overall flow pattern. At sufficiently high angle of attack the recovery of the vortical structures with significant increases in the magnitude of suction pressure coefficient $-C_p$, which implies the elimination of three-dimensional surface separation is achieved. On the contrary, at low attack angles, the bleeding causes reduction in the magnitudes of suction pressure coefficient $-C_p$ in general, indicating a loss in suction performance of the planform.

The bioinspired material modification study is based on flexion ratio concept inspired from animal propulsion. For this purpose, the experiments are conducted for a broad range of Reynolds numbers $10^4 \leq Re \leq 10^5$ and attack angles $8 \leq \alpha \leq 30$ deg using four different 45 deg swept delta wings of flexion ratios $a/S = 0.3, 0.5, \text{ and } 0.7$ along with a base planform. The results indicate that the partial flexibility of the delta wing does not induce notable variation in the flow structure over the wing within the Reynolds number ranges tested in the current study.

Keywords: Nonslender delta wing, Low sweep angle, Leading edge vortex, Three-dimensional surface separation, Passive flow control, Edge Modification, Bioinspiration, Biomimicking, Bleeding.

ÖZ

DÜŞÜK OK AÇILI DELTA KANATLAR İÇİN YENİLİKÇİ AKIŞ KONTROL YÖNTEMLERİ GELİŞTİRİLMESİ VE UYGULAMASI

Çelik, Alper

Doktora, Makina Mühendisliği Bölümü

Tez Yöneticisi : Doç. Dr. Mehmet Metin Yavuz

Haziran 2017, 181 sayfa

Düşük ve orta ok açılı delta kanatlar üzerindeki akışın anlaşılması ve kontrolü, bu planformaların insansız savaş uçakları ve mikro hava araçları gibi kullanım alanlarının ortaya çıkması nedeniyle son yıllarda pek çok araştırmacı için ilgi çekici bir alan haline gelmiştir. Delta kanatlar yüksek hücum açılarında yüksek kaldırma kuvveti oluşturup kararlı bir uçuş sağlamaktadır; ancak konvansiyonel akış kontrol yüzeylerinin olmaması delta kanatlar üzerinde uygulanabilecek yeni akış kontrol yöntemlerinin oluşturulması gerekliliğini ortaya çıkarmıştır. Bu çalışmada, ok açısı 45 derece olan delta kanat üzerinde oluşan akış yapılarının yenilikçi pasif yöntemlerle kontrol edilmesi amaçlanmıştır. Deneyle; düşük hızlı rüzgâr tüneline, parçacık görüntülemeli hız ölçüm tekniği, yüzey basınç ölçümleri ve lazer aydınlatmalı duman görüntüleme yöntemleri kullanılarak yapılmıştır. Biyo-ilhamlı kenar değişiklikleri, biyo-ilhamlı malzeme değişiklikleri ve pasif akıtma yöntemleri olmak üzere detayları aşağıda anlatılan üç farklı pasif akış kontrolü geliştirilmiş ve incelenmiştir.

Biyo-ilhamlı kenar değişikliği çalışmaları için delta kanatlarla geometri benzerliği olan memeli kuyruk şekli esas alınmıştır. Yapılan değişikliklerin etkisi Reynolds

sayısı $10^4 < Re < 2.5 \times 10^4$ aralığında ve hücum açıları $4 < \alpha < 12$ derece olarak alınmıştır. Sonuçlar, planform üzerinde uygulanan kenar değişikliklerinin kanatların stall performansını mevcut çalışma aralığında beklenenin aksine düşürdüğünü göstermiştir.

Çalışmanın diğer bir bölümünde, 45 derece ok açısına sahip delta kanat üzerindeki akış yapılarının pasif akıtma tekniği ile kontrolü hedeflenmiştir. Çalışılan kontrol tekniğinin etkisini belirleyebilmek için oluşturulan üç farklı kanat geometrisi geniş bir çalışma aralığını temsil eden hücum açıları $6 \leq \alpha \leq 16$ derece ve Reynolds sayıları $10^4 < Re < 10^5$ arasında referans kanatla karşılaştırılmıştır. Sonuçlar pasif akıtmanın kanat üzerindeki akışı etkilediğini ve doğru akıtma yöntemiyle kanat üzerindeki akış yapılarında yüksek ölçüde iyileşme sağlanacağını göstermektedir. Referans kanadın üzerindeki akışın yüzeyden ayrıldığı yüksek hücum açılarında, doğru akıtma şekliyle üç boyutlu akış ayrılmasının geciktirildiği ve girdaplı yapıların geri kazanılması ile emme basınç katsayısı $-C_p$ 'nin yükseldiği gözlenmiştir. Düşük hücum açılarında ise pasif akıtma emme basınç katsayısı $-C_p$ 'de düşüş yaratmıştır.

Düşük ok açılı delta kanatlar üzerindeki akışın kontrolü için yapılan bir diğer çalışmada ise hayvanların biyo-ilhamlı kısmi esnek kanatlarla çalışılmıştır. Bu amaçla, deneyler geniş bir çalışma aralığı olan Reynolds sayısı $10^4 \leq Re \leq 10^5$ ve hücum açısı $8 \leq \alpha \leq 30$ derecede esneme oranı $a/S = 0.3, 0.5, \text{ ve } 0.7$ olan üç farklı 45 derece ok açılı delta kanatla yapılmıştır. Elde edilen sonuçlar, uygulanan kısmi esnekliğin çalışılan Reynolds sayısı ve hücum açıları için akış yapılarını anlamlı şekilde değiştirmedeğini göstermiştir.

Anahtar Kelimeler: Düşük ok açılı delta kanat, düşük ok açısı, hücum kenarı girdabı, üç-boyutlu akış ayrılması, pasif akış kontrolü, kenar değişikliği, Biyo-ilham, Biyo-benzetim, akıtma.



To my parents

ACKNOWLEDGMENTS

I would like to express my sincere gratitude to my thesis supervisor, Dr. Mehmet Metin Yavuz, for his guidance, support and distinguished supervision throughout these years. Dr. Yavuz is one of the friendliest supervisor with an extremely open-mind. I am grateful to him for sharing his both academic and life experiences with me.

My deepest gratitude goes to Prof. Dr. Cahit Eralp who passed away in 2010, and gave me the opportunity to be a part of academic world and share his experience with me. His impact on my life is substantial and unforgettable.

Words cannot express how grateful I am to my parents Ayşe Çelik and Ferudun Çelik, my sisters Derya Çelik and Eda Çelik Erdilli for their support throughout my academic life.

I would like to express very special thanks to my uncle Şenol Candaş who has been a great support in my life from my childhood to this day.

Including the last 5 years of my PhD study, the time I spent in METU which is more than a decade, has been most precious with my dear friends Halil Ünay, Gülay Oskay Ünay, Enes Bahar. Endless appreciation and thanks to them for being in my life and for taking care of me through hard times. I would also like to express my sincere thanks to Seher Ayatollahi Bahar for her kindness, hospitality in a period of turmoil.

I would like to thank my friends Cenk Çetin, Gökay Günacar, Gizem Şencan and Burak Gülsaçan for their help in Fluid Mechanics Lab and friendship. Experimenting is a team work and I was lucky enough to have them around. A

very special thank you to Ali Karakuş and Mahmut Murat Göçmen who both supported me with their friendship, scientific chats and coding abilities.

Dearest friends from youth, Berkan Baki, Murat Can Şalvarcı, Gökhan Kaya, Özmen Serdar, Uğur Haliloğlu, Orhan Kemal Yücesan, Eray Baydar and Eray Yanmış made my days in Trabzon easier after my hard decision on leaving Lehigh. I am indebted to all of them. I would also like to thank Haydar Uzuner for being supportive through all these years both in Trabzon and Ankara.

I would also like to thank my dear friends Isa Kavas and Elif Altuntop Kavas for everything they contribute to my life. Their support through these years were invaluable.

L1 has a very special place in my life now. I am very grateful to each of them for letting me be a part of their friendly environment. It was most welcoming and most appreciated. Thanks to Utku Civelek, Sezil Solta, Berat Can Cengiz, Cemre Cengiz, Anıl Öztürk, Müge Öztürk, Özge Güven and Okan Arslan.

Many thanks to Özgür Cem Ceylan and Gencer Koç for always being available for friendly chats, advice and support.

I thank all my colleagues in Tubitak Uzay for supporting me during last two years of this study. Their patience allowed me to be more productive.

I would like to thank my thesis progress committee members Oğuz Hoca and Cüneyt Hoca for their valuable advices, guidance and support. Their positive feedbacks encouraged me to do more all through this work.

The technical assistance of Mr. Rahmi Ercan and Mr. Mehmet Özçiftçi are gratefully acknowledged.

TABLE OF CONTENTS

ABSTRACT	v
ÖZ.....	vii
ACKNOWLEDGMENTS	x
TABLE OF CONTENTS	xii
LIST OF FIGURES	xv
LIST OF TABLES	xxi
NOMENCLATURE.....	xxii
CHAPTERS	
1. INTRODUCTION.....	1
1.1 Motivation of the Study.....	4
1.2 Aim of the Study	4
1.3 Structure of the Thesis	5
2. LITERATURE SURVEY.....	11
2.1 Flow Structures over Delta Wings	11
2.1.1 Vortex Structure	11
2.1.2 Vortex Breakdown.....	12
2.1.3 Shear Layer Instabilities	13
2.1.4 Shear Layer Reattachment.....	14
2.2 Flow Control Techniques on Delta Wings	14
2.2.1 Active Control	15
2.2.2 Passive Control.....	17

3. EXPERIMENTAL SET-UP AND TECHNIQUES.....	35
3.1 Wind Tunnel	35
3.1.1 Wind Tunnel Characterization	36
3.2 Flow Measurement Techniques	36
3.3 Experimental Matrices and Delta Wing Models.....	44
3.4 Uncertainty Estimates	50
4. EFFECT OF EDGE MODIFICATIONS ON FLOW STRUCTURE OF A NONSLENDER DELTA WING -PART I	75
4.1 Results and Discussions.....	75
4.2 Conclusion	83
5. EFFECT OF EDGE MODIFICATIONS ON FLOW STRUCTURE OF A NONSLENDER DELTA WING -PART II.....	93
5.1 Results and Discussions.....	93
5.2 Conclusion	96
6. EFFECT OF PASSIVE BLEED ON FLOW STRUCTURE OVER A NONSLENDER DELTA WING	103
6.1 The Effect of Bleeding on Flow Structure at $Re = 10^4$	104
6.2 The Effect of Bleeding on Flow Structure at $Re = 10^5$	107
6.3 The Effect of Bleeding on Surface Pressure Measurements: <i>Reynolds</i> <i>Number Dependence</i>	109
6.4 The Effect of Bleeding on Pressure and Velocity Fluctuations	112
6.5 Conclusion	114
7. EFFECT OF FLEXION RATIO ON FLOW STRUCTURE OVER A NONSLENDER DELTA WING	125
7.1 The Effect of Flexion Ratio on Flow Structure at $Re = 10^5$	125

7.2 The Effect of Flexion Ratio on Flow Structure at $Re = 2 \times 10^4$	127
7.3 The Effect of Flexion Ratio on Flow Structure at $Re = 10^4$	128
7.4 Additional Discussion on the Results of Flexion Ratio Study	130
7.5 Conclusion	131
8. CONCLUSION	143
8.1 Summary and Conclusions	143
8.2 Recommendations for Future Work	145
REFERENCES	149
APPENDIX A	163
APPENDIX B	165
APPENDIX C	169
CURRICULUM VITAE	179

LIST OF FIGURES

FIGURES

Figure 1-1 Schematic representation of shear layer and leading edge vortices over a delta wing [3].....	7
Figure 1-2 Schematics demonstrating increase in axial core velocity (top) and non-dimensional mean axial core velocities(bottom) [15].....	8
Figure 1-3 Dual-vortex structure observed over a nonslender delta wing[16]	8
Figure 1-4 Delta wing vortex formation: main delta wing flow features (a) and vortex bursting characteristics (b) [5].	9
Figure 1-5 Schematic streamline patterns for (a) reattachment over nonslender wings and (b) with no reattachment on wing surface on slender [3].	9
Figure 2-1 Shear-layer separation and formation of leading edge vortex [99] [100].	23
Figure 2-2 Illustration of vortex lift contribution to lift coefficient according to Palhaums vortex lift theory [17]	23
Figure 2-3 Axial vorticity patterns of a dual vortex structure [3].	24
Figure 2-4 Illustration of bubble, double helix and spiral type breakdown from top to bottom respectively [23]	24
Figure 2-5 Visualization of both spiral and bubble vortex breakdown on a slender delta wing [15].	25
Figure 2-6 PIV measurement results of shear layer sub-structures for a 38.7 deg swept delta wing [7]	25
Figure 2-7 Effectiveness of (left)steady and unsteady blowing (right) blowing-suction methods [3].	26
Figure 2-8 Effect of suction on vortex breakdown location (a)without suction (b) with suction [54].	26
Figure 2-9 Bleed through the airfoil [63].....	27

Figure 2-10 Overview of the objects and their corresponding functions in nature [70].	27
Figure 2-11 Planform of flukes from representative cetacean species [101].	28
Figure 2-12 Fluke dimensions of planform (top) and cross sectional view (bottom) [101].	29
Figure 2-13 Comparison of lift coefficient and L/D ratio of rigid and flexible wings of different stiffness [102].	29
Figure 2-14 Trust coefficient as a function of heave for a inflexible, flexible and highly flexible wing [96].	30
Figure 2-15 Comparison of lift coefficients for rigid and flexible delta wings of different sweep angle [34].	31
Figure 2-16 Comparison of effect of flexibility on half wing and full wing[34].	32
Figure 2-17 Flexion morphospace (top) and patterns of propulsor bending by variety of animals moving steadily through air and water (bottom) [98].	33
Figure 2-18 Generality of bending patterns across a variety of animal categories [98].	34
Figure 3-1 View from wind tunnel facility (top) and test section (bottom).	54
Figure 3-2 Wing model, mount and test section assembly.	55
Figure 3-3 Wind tunnel calibration graph.	55
Figure 3-4 Examples of flow visualization results a) laser illuminated smoke visualization, b) tuft visualization[6], c)dye visualization [6], d) surface oil visualization[107].	56
Figure 3-5 Schematics of cross flow laser-illuminated smoke visualization experiment set-up.	57
Figure 3-6 Classes of pulsed-light velocimetry.	57
Figure 3-7 Flow chart of PIV experiment : acquisition, processing, post-processing and analysis.	58
Figure 3-8 Schematic representation of the cross flow PIV experiment set-up	59
Figure 3-9 Possible methods for pulse-coding and framing methods in Particle Image Velocimetry [103].	60

Figure 3-10 Data transfer routes of a 2D PIV system.....	60
Figure 3-11 Comparison of FFT correlator with Hart correlator on results at 16x16 and 32x32 interrogation windows via streamlines, velocity vectors and non-dimensional axial vorticity contours from top to bottom respectively.	61
Figure 3-12 Schematics of how to calculate vrms data from original tecplot vector file.	62
Figure 3-13 Manufactured wings for bio-inspired edge-modification experiments.	63
Figure 3-14 Experiment matrices for edge modification experiments Part-I (up) and Part II (bottom).	64
Figure 3-15 Overview of the wing models and measurement planes for bio-inspired edge modification experiments for Part I.	65
Figure 3-16 Overview of the wing models and measurement planes for additional bio-inspired edge modification experiments for Part II.	66
Figure 3-17 Manufactured wings for passive bleed experiments.	67
Figure 3-18 Details of bleeding configurations of B, E and BE planforms.	68
Figure 3-19 Experiment matrix for passive bleed experiments.	69
Figure 3-20 Overview of the experimental set-up and with delta wing and laser sheet locations for passive bleed experiments.	70
Figure 3-21 Geometric details of flexion experiment wings with examples of manufactured wings.	71
Figure 3-22 Experimental matrix for flexion ratio concept experiments.....	72
Figure 3-23 Overview of the planform with laser sheet orientations for cross flow PIV experiments.....	73
Figure 4-1 Surface flow smoke visualizations for base wing (BW), modified dolphin fluke (MDF), and dolphin fluke (DF) planforms for Reynolds numbers $Re = 104$, $Re = 1.5 \times 10^4$, $Re = 2 \times 10^4$ and $Re = 2.5 \times 10^4$ at attack angle of $\alpha = 4^\circ$	85
Figure 4-2 Comparison of surface and cross flow smoke visualizations for base wing (BW) and dolphin fluke (DF) planforms for $Re = 1.5 \times 10^4$ at attack angle of $\alpha = 4^\circ$	86

Figure 4-3 Surface flow smoke visualizations for base wing (BW), modified dolphin fluke (MDF), and dolphin fluke (DF) planforms for Reynolds numbers $Re = 104$, $Re = 1.5 \times 10^4$, $Re = 2 \times 10^4$ and $Re = 2.5 \times 10^4$ at attack angle of $\alpha = 6^\circ$	87
Figure 4-4 Surface flow smoke visualizations for base wing (BW), modified dolphin fluke (MDF), and dolphin fluke (DF) planforms for Reynolds numbers $Re = 104$, $Re = 1.5 \times 10^4$, $Re = 2 \times 10^4$ and $Re = 2.5 \times 10^4$ at attack angle of $\alpha = 8^\circ$	88
Figure 4-5 Surface flow smoke visualizations for base wing (BW), modified dolphin fluke (MDF), and dolphin fluke (DF) planforms for Reynolds numbers $Re = 104$, $Re = 1.5 \times 10^4$, $Re = 2 \times 10^4$ and $Re = 2.5 \times 10^4$ at attack angle of $\alpha = 10^\circ$	89
Figure 4-6 Comparison of surface and cross flow smoke visualizations for base wing (BW) and dolphin fluke (DF) planforms for $Re = 104$ at attack angle of $\alpha = 10^\circ$	90
Figure 4-7 Surface flow smoke visualizations for base wing (BW), modified dolphin fluke (MDF), and dolphin fluke (DF) planforms for Reynolds numbers $Re = 104$, $Re = 1.5 \times 10^4$, $Re = 2 \times 10^4$ and $Re = 2.5 \times 10^4$ at attack angle of $\alpha = 12^\circ$	91
Figure 4-8 Vortex breakdown locations for attack angle of $\alpha = 4^\circ, 6^\circ$ and 8° at $Re = 104$, $Re = 1.5 \times 10^4$, $Re = 2 \times 10^4$ and $Re = 2.5 \times 10^4$	92
Figure 5-1 Surface flow smoke visualizations for BW, DF, OL, OT and OTE planforms for Reynolds numbers $Re = 104$ at attack angle of $\alpha = 4^\circ$	97
Figure 5-2 Surface flow smoke visualizations for BW, DF, OL, OT and OTE planforms for Reynolds numbers $Re = 2.5 \times 10^4$ at attack angle of $\alpha = 4^\circ$	98
Figure 5-3 Surface flow smoke visualizations for BW, DF, OL, OT and OTE planforms for Reynolds numbers $Re = 104$ at attack angle of $\alpha = 12^\circ$	99
Figure 5-4 Surface flow smoke visualizations for BW, DF, OL, OT and OTE planforms for Reynolds numbers $Re = 2.5 \times 10^4$ at attack angle of $\alpha = 12^\circ$...	100
Figure 5-5 Comparison of whole planforms, at $Re = 1 \times 10^4$ and $Re = 2.5 \times 10^4$ at attack angles $\alpha = 4^\circ$ and $\alpha = 12^\circ$	101
Figure 6-1 Patterns of time-averaged velocity vectors V , streamlines Ψ and constant contours of non-dimensional axial vorticity $\omega C/U$ at angle of attack $\alpha = 6$ deg for $Re = 104$: $\omega C/U_{min} = 7$, $\Delta \omega C/U = 2$	116

Figure 6-2 Patterns of time-averaged velocity vectors V , streamlines Ψ and constant contours of non-dimensional axial vorticity $\omega C/U$ at angle of attack $\alpha = 10$ deg for $Re = 104$: $\omega C/U_{min} = 7$, $\Delta\omega C/U = 2$	116
Figure 6-3 Patterns of time-averaged velocity vectors V , streamlines Ψ and constant contours of non-dimensional axial vorticity $\omega C/U$ at angle of attack $\alpha = 16$ deg for $Re = 104$: $\omega C/U_{min} = 7$, $\Delta\omega C/U = 2$	117
Figure 6-4 Surface -flow and half span cross -flow smoke visualizations for Base, B, E and BE planforms for $Re = 104$ at angle of attack $\alpha = 6$ deg.....	118
Figure 6-5 Patterns of time-averaged velocity vectors V , streamlines Ψ and constant contours of non-dimensional axial vorticity $\omega C/U$ at angle of attack $\alpha = 6$ deg for $Re = 105$: $\omega C/U_{min} = 7$, $\Delta\omega C/U = 2$	119
Figure 6-6 Patterns of time-averaged velocity vectors V , streamlines Ψ and constant contours of non-dimensional axial vorticity $\omega C/U$ at angle of attack $\alpha = 10$ deg for $Re = 105$: $\omega C/U_{min} = 7$, $\Delta\omega C/U = 2$	119
Figure 6-7 Patterns of time-averaged velocity vectors V , streamlines Ψ and constant contours of non-dimensional axial vorticity $\omega C/U$ at angle of attack $\alpha = 16$ deg for $Re = 105$: $\omega C/U_{min} = 7$, $\Delta\omega C/U = 2$	120
Figure 6-8 $-C_p$ distributions of half span Base, B, E and BE planforms at angle of attacks $\alpha = 6, 10$ and 16 deg at $Re = 3.5 \times 10^4$ (left) and $Re = 105$ (right)...	121
Figure 6-9 Comparison of surface and cross flow smoke visualizations at $Re = 3.5 \times 10^4$ with constant contours of non-dimensional axial vorticity patterns $\omega C/U$ and $-C_p$ distribution at $Re = 3.5 \times 10^4$ and $Re = 105$ for Base (left) and B (right) planforms. $\omega C/U_{min} = 7$, $\Delta\omega C/U = 2$	122
Figure 6-10 Patterns of constant contours of non-dimensional axial vorticity $\omega C/U$ ($\omega C/U_{min} = 7$, $\Delta\omega C/U = 2$) and constant contours of non-dimensional root mean square of vertical velocity $w_{rms}U$ ($w_{rms}/U_{min} = 0.08$, $\Delta w_{rms}/U = 0.015$) at $Re = 3.5 \times 10^4$ and $Re = 105$ for Base and B planforms for attack angle $\alpha = 16$ deg.	123
Figure 6-11 Patterns of constant contours of non-dimensional root mean square of vertical velocity $w_{rms}U$ ($w_{rms}/U_{min} = 0.08$, $\Delta w_{rms}/U = 0.015$) and non-dimensional root mean square of pressure fluctuations C_p, rms for Base, B, E and BE planforms at $Re = 3.5 \times 10^4$ for attack angles $\alpha = 6$ deg and $\alpha = 16$ deg..	124
Figure 7-1 Patterns of time-averaged velocity vectors V , streamlines Ψ and constant contours of non-dimensional axial vorticity $\omega C/U$ and patterns of constant contours of non-dimensional root mean square of vertical velocity) at	

angle of attack $\alpha = 12$ deg for $Re = 105$: $\omega C/U_{min} = 7$, $\Delta\omega C/U = 2$, $w_{rms}/U_{min} = 0.08$, $\Delta w_{rms}/U = 0.015$ 133

Figure 7-2 Patterns of time-averaged velocity vectors V , streamlines Ψ and constant contours of non-dimensional axial vorticity $\omega C/U$ and patterns of constant contours of non-dimensional root mean square of vertical velocity) at angle of attack $\alpha = 24$ deg for $Re = 105$: $\omega C/U_{min} = 7$, $\Delta\omega C/U = 2$, $w_{rms}/U_{min} = 0.08$, $\Delta w_{rms}/U = 0.015$ 134

Figure 7-3 Patterns of time-averaged velocity vectors V , streamlines Ψ and constant contours of non-dimensional axial vorticity $\omega C/U$ and patterns of constant contours of non-dimensional root mean square of vertical velocity) at angle of attack $\alpha = 30$ deg for $Re = 105$: $\omega C/U_{min} = 7$, $\Delta\omega C/U = 2$, $w_{rms}/U_{min} = 0.08$, $\Delta w_{rms}/U = 0.015$ 135

Figure 7-4 Patterns of time-averaged velocity vectors V , streamlines Ψ and constant contours of non-dimensional axial vorticity $\omega C/U$ at angle of attack $\alpha = 8$ deg for $Re = 2 \times 104$: $\omega C/U_{min} = 8$, $\Delta\omega C/U = 4$ 136

Figure 7-5 Patterns of time-averaged velocity vectors V , streamlines Ψ and constant contours of non-dimensional axial vorticity $\omega C/U$ at angle of attack $\alpha = 10$ deg for $Re = 2 \times 104$: $\omega C/U_{min} = 8$, $\Delta\omega C/U = 4$ 137

Figure 7-6 Patterns of time-averaged velocity vectors V , streamlines Ψ and constant contours of non-dimensional axial vorticity $\omega C/U$ at angle of attack $\alpha = 12$ deg for $Re = 2 \times 104$: $\omega C/U_{min} = 8$, $\Delta\omega C/U = 4$ 138

Figure 7-7 Patterns of time-averaged velocity vectors V , streamlines Ψ and constant contours of non-dimensional axial vorticity $\omega C/U$ at angle of attack $\alpha = 14$ deg for $Re = 2 \times 104$: $\omega C/U_{min} = 8$, $\Delta\omega C/U = 4$ 139

Figure 7-8 Patterns of time-averaged velocity vectors V , streamlines Ψ and constant contours of non-dimensional axial vorticity $\omega C/U$ at angle of attack $\alpha = 12$ deg for $Re = 104$: $\omega C/U_{min} = 5$, $\Delta\omega C/U = 5$ 140

Figure 7-9 Deflection types encountered during experiments..... 141

Figure 7-10 Comparison of vorticity levels of base planform to downward deflected flap (upper row) and upward deflected flap (bottom row) [111] 142

Figure 7-11 Wing with carbon-fiber epoxy rods [112]. 142

LIST OF TABLES

TABLES

Table 1 Uncertainty values for the pressure measurements for passive bleed experiments for all planforms at the maximum and the minimum Reynolds numbers for attack angles $\alpha = 6, 10$ and 16 deg.....	52
Table 2 Uncertainty values for the PIV measurements for passive bleed experiments for all planforms at the maximum and minimum Reynolds numbers for attack angles $\alpha = 6$ and 16 deg.....	53
Table 3 Uncertainty values for the PIV measurements for flexion ratio concept experiments for base planform and planform $a/S = 0.7$ at the maximum and minimum Reynolds numbers for attack angles $\alpha = 12$ and 30 deg.....	53

NOMENCLATURE

Λ	Sweep angle
C	Chord length
s	Semi span length
α	Angle of attack
Re	Reynolds number based on chord length
U	Free stream velocity
V	Velocity vector
u	Streamwise velocity
w	Vertical velocity
ω	Vorticity
Ψ	Streamfunction
x	Chordwise distance from wing apex
y	Spanwise distance from wing root chord
p	Surface pressure
\bar{p}	Average surface pressure
p_{RMS}	Root mean square of the surface pressure
p_{∞}	Static pressure of the flow
p_{dyn}	Dynamic pressure of the flow
C_p	Dimensionless pressure coefficient
$C_{p,RMS}$	Root mean square of the pressure coefficient
ρ	Fluid density
ν	Fluid kinematic viscosity
N	Number of samples in a measurement
PIV	Particle Image Velocimetry
ω_i	Uncertainty estimate of a variable i
u_i	Relative uncertainty estimate

CHAPTER 1

INTRODUCTION

Flow control over nonslender delta wings draw increasing attention in recent years due its common usage in unmanned air vehicles (UAV) and micro air vehicles (MAV). Desire for improved performances for UAVs and MAVs compels researchers to extend their knowledge on both flow physics and flow control mechanisms over nonslender delta wings. Although pioneering studies on aerodynamics of delta wings dates back to 1960's [1], there still exists great territories to explore. Nonslender delta wings, sweep angle less than 55 deg, have great potential in terms of high maneuverability, high flexibility, and low structural-weight-to-take-off-weight ratio, however, problems related to aerodynamics performance and flow instability remain unresolved.

Delta wings are classified as slender so-called high swept where the sweep angle is higher than 55 degrees and nonslender so-called low swept where the sweep angle is smaller than 55 degrees. On both type of wing, the flow over the planform is dominated by vortical structures. Flow over a delta wing separates from the leading edge to roll up into a coherent vortex structure which is fed by discrete vortices emanating through the leading edge[2] and Figure 1-1 demonstrates this phenomenon. The stream wise time-averaged core velocity of the vortex structure may go up 3 to 5 times of free stream velocity and induces strong suction areas which are accounted as a major contributor to lift force as sweep angle increase [3]. Figure 1-2 illustrates the typical jet-like velocity distribution across a vortex core and its mean value compared to free stream velocity. However, as sweep angle decreases, the core velocities decrease accompanied with lower lift contributions, lower stall angles and lower maximum lift coefficients. The vortices over nonslender delta wings appear closer to the wing surface compared

to slender delta wings [4], which lead to an interaction between the boundary layer and the vortex [5], resulting in a second primary vortex structure as shown in Figure 1-3, and a more sensitive flow to Reynolds number.

In exchange for the benefits of vortices, an increased lift force on planforms, delta wings suffer from instabilities such as vortex breakdown, shear layer instabilities, vortex wandering, vortex shedding and vortex oscillations. Among all the instabilities, vortex breakdown is addressed and investigated as a major phenomenon affecting the aerodynamic performance of delta wings. Vortex breakdown occurs at higher angle of attacks, where the coherent vortex core experiences an abrupt expansion due to pressure gradient encountered and swirl level, and loses the jet like velocity profile in the vortex-core, which results in undesired loss of lift force. Moreover, when breakdown location moves over the planform, buffeting, structural response to unsteady flow, is observed due to high velocity fluctuations. Figure 1-4 represents the main flow structures over a delta wing planform, with vortex breakdown characteristics.

Reattachment of the separated shear layer to wing planform is another major phenomenon over the delta wing planforms, contributing to both vortical coherence and instabilities depending on the attack angle. The separated shear layer doesn't reattach to wing planform on slender delta wings except for very low incidences. However, the vortical coherence over nonslender delta wings strongly depends on the location and strength of the reattachment. The schematics of reattachment over both slender and nonslender delta wings are presented in Figure 1-5. As the angle of attack increases, the vortex breakdown location moves towards the apex, accompanied with the inboard movement of reattachment line for nonslender wings. At this point, maximum velocity fluctuations are observed not under the vortex breakdown location but along the reattachment line, which is just outboard the wing root chord and associated to substantial buffeting observed prior to stall [6]. At sufficiently high angle of attacks, the vortex breakdown location reaches to apex, the reattachment line on nonslender delta wings locates

over the wing root chord, and the flow completely separates from the planform and leads to stall. In order to characterize these phenomenon over the nonslender planforms, increasing number of efforts have been conducted in the last few decades including the studies focusing on the topological representations [18,19], Reynolds number effect [9], leading and trailing edge effect [21-23], and effect of planform orientation [24 ,25].

The vital role of the stable vortices on aerodynamics of delta wing planforms requires challenging flow control strategies. The most common aims of the flow controls over delta wings are to prevent separation, delay stall or delay vortex breakdown locations. The control strategies over slender delta wings targets to prevent or delay vortex breakdown since the lift gain due to vortices has primary importance, and vortex breakdown over the planform is the primary source of buffeting on slender delta wings. However, on nonslender delta wings, vortices have lower contribution to lift force and the breakdown occurs on planform even for low attack angles. Moreover, the reattachment of the separated shear layer is identified as one of the major source of instabilities [6]. Hence the control target is mainly prevention of separation and enhancing the reattachment of separated shear layer.

In literature, active or passive means of flow control methods are applied on delta wings to avoid the aforementioned undesired phenomenon on planforms. Using control surfaces, blowing or suction of air from various locations on the planform surface, steady or unsteady excitations applied to flow domain are the most common methods studied in literature[6]. Passive control methods do not require any energy input to flow field, are relatively easy to apply and consists the scope of this present study. Most common passive flow control methods in literature are geometry modifications and material modifications some of which are inspired from nature.

1.1 Motivation of the Study

Complex flow patterns over modern Micro Air Vehicles (MAV), Unmanned Combat Air Vehicles (UCAV) and Unmanned Air Vehicles (UAV) experience challenging conditions during steady and unsteady flight. Since the produced lift force and the stability of the planforms strongly depend on these structures, understanding and controlling the flow features over these planforms under extreme conditions are necessities. Different control approaches have been applied to alter the flow structure with interests in preventing stall and delaying vortex breakdown. Passive flow control methods require no energy input to flow field and is relatively easier compared to active flow control methods. However passive flow control method applications on nonslender delta wings are rather limited in extent and are inadequate in terms of practical applications. The main motivation of this study is to develop and implement novel passive flow control methods to control flow structures over nonslender delta wings and to report their effectiveness.

1.2 Aim of the Study

The aim of the study was to develop and implement novel flow control techniques for flow structure on $\Lambda=45^\circ$ swept delta wing. Three different passive flow control methods were developed and investigated including bioinspired edge modification, bioinspired material modification, and passive bleeding. Bioinspired edge modifications are studied based on the apparent geometrical similarities between delta wing shapes and cetacean flukes, where various leading and trailing edge configurations are tested. Passive bleeding, using the inherent pressure difference between the suction and pressure side of the wing to control the flow structures, is studied via directing the high pressure air through the passages on planform in different directions over the suction surface. The bioinspired material modification is studied on flow structure of a nonslender delta wing by implementing partially flexible wings inspired from flexion ratio concept, which

is based on the bending rules of animal propulsion. The experiments were conducted in a low speed wind tunnel using laser-illuminated flow visualization, surface pressure measurements, and particle image velocimetry (PIV). Broad ranges of Reynolds numbers and attack angles for each study, which fell into $4^\circ < \alpha < 30^\circ$ for attack angle and $10^4 < Re < 10^5$ for Reynolds number, were tested. Five different edge modifications, three different bleeding configurations, and three different partially flexible wings were used and compared with the base wing.

1.3 Structure of the Thesis

This thesis is composed of eight main chapters. Chapter 1 provides introductory information on delta wings and summarizes the aim and the motivation of the current study.

Chapter 2 presents the detailed literature review including the general flow features over delta wings focused on nonslender delta wings, flow control techniques, and subheading dedicated to the previously conducted studies on each novel method implemented in the present study.

The technical details of the experimental set-up and the measurement systems used in the current study along with the experimental matrix for each method are described in Chapter 3.

Chapter 4 and 5 presents the results of laser-illuminated smoke visualization for bio-inspired edge-modifications.

Chapter 6 presents and discusses the results of passive bleeding experiments. An extensive investigation is conducted via laser-illuminated smoke visualization, pressure measurements and PIV experiments.

Chapter 7 demonstrates and discusses the PIV results of application of flexion ratio concept wing planforms.

Chapter 8 provides the conclusions throughout the study including the recommendations for possible future work.



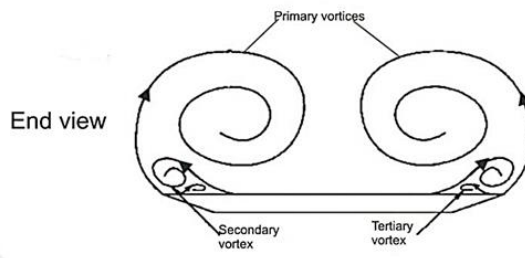
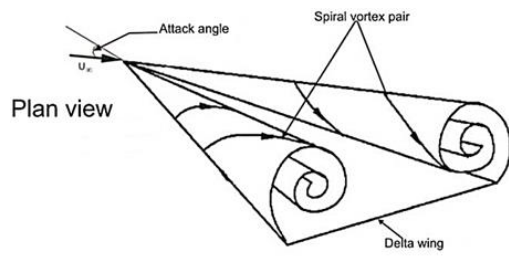


Figure 1-1 Schematic representation of shear layer and leading edge vortices over a delta wing [3].

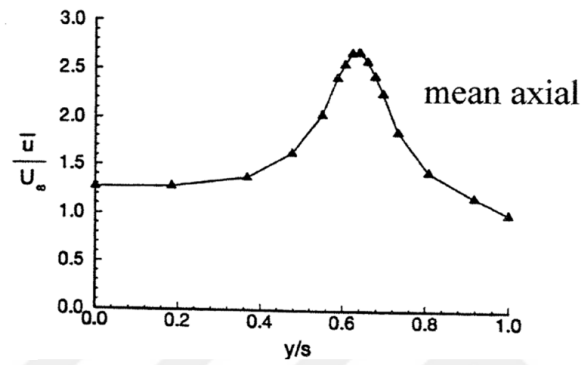
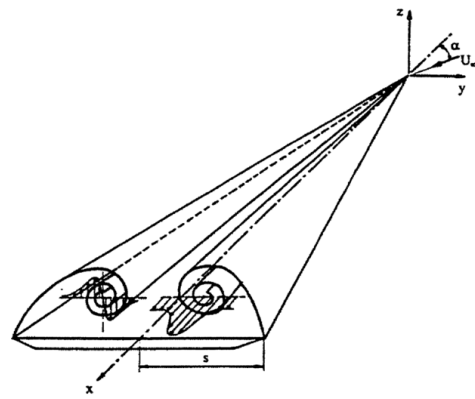


Figure 1-2 Schematics demonstrating increase in axial core velocity (top) and non-dimensional mean axial core velocities(bottom) [15].

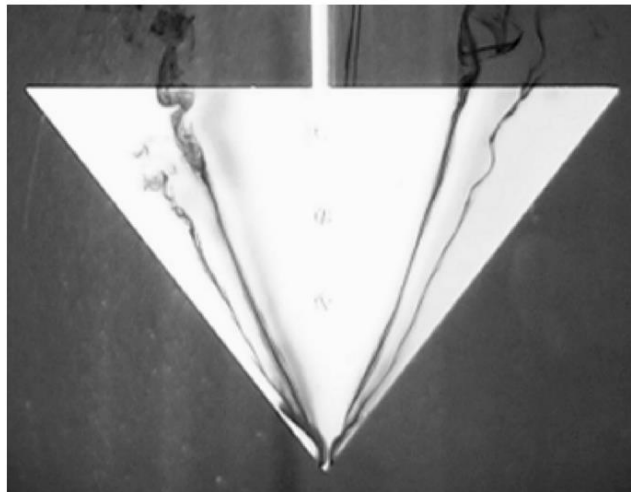


Figure 1-3 Dual-vortex structure observed over a nonslender delta wing[16] .

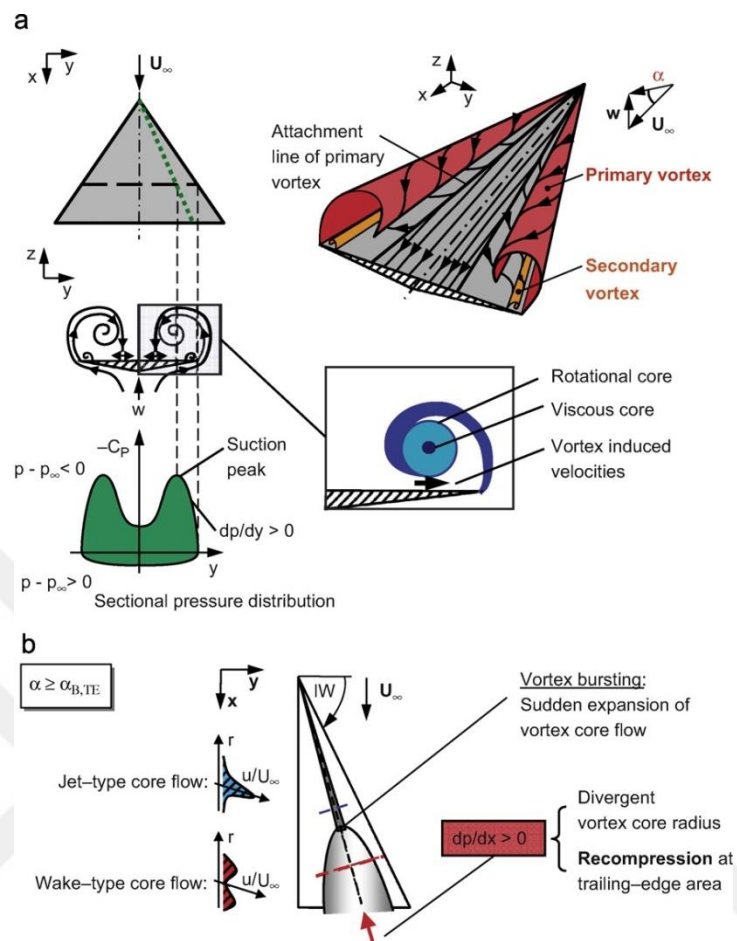


Figure 1-4 Delta wing vortex formation: main delta wing flow features (a) and vortex bursting characteristics (b) [5].

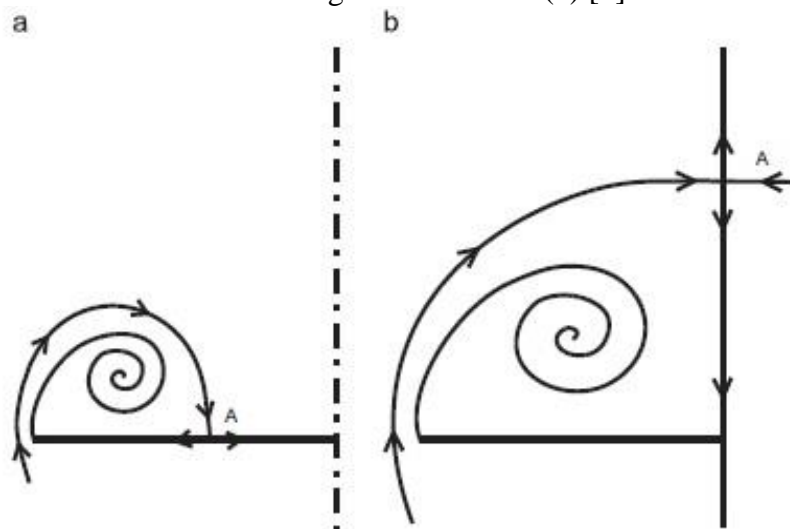


Figure 1-5 Schematic streamline patterns for (a) reattachment over nonslender wings and (b) with no reattachment on wing surface on slender [3].



CHAPTER 2

LITERATURE SURVEY

This chapter covers the essential literature related to the delta wing flow physics and the flow control mechanisms over delta wings as well as the detailed literature on the control techniques that were applied in this study.

2.1 Flow Structures over Delta Wings

2.1.1 Vortex Structure

For a slender delta wing the flow is dominated by a primary vortex, formed by roll-up of vortex sheets. These sheets are created by the separation of flow from the leading edge of the wing. Figure 2-1 illustrates the visualization of separated shear layer rolling up to form the vortex in the top row and the discrete vortical structures forming the primary vortex in the bottom row. These vortex structures enhance the lift force on delta wing. Polhamus predicted analytically that the contribution of vortices to lift may be as high as the potential lift for high swept delta wings [17]. Figure 2-2 presents a chart where the ratio of potential lift to vortex lift can be observed. Velocities in the core of vortex of a slender wing may go up to 4-5 times the free-stream velocities [3] which means a decrease in surface pressure. As a result, an enhanced suction region exists on the wing planforms.

For a nonslender delta wing, leading edge separation and vortex formation are observed with one major difference compared to slender delta wings for low angle of attacks. The vortex core on a nonslender delta wing forms closer to wing

surface compared to slender wings. This difference creates a major change in the flow structure. Basically, the interaction of the primary vortex with the boundary layer on wing may create a second vortex structure with same rotation direction. This structure, consisting two vortices with same rotation direction, is called “dual vortex structure” and observed in low Reynolds numbers and only in low angle of attacks. Figure 2-3 illustrates a numerical result showing a dual vortex structure on half span. Another major consequence of the location of the vortex core is the Reynolds number sensitivity of flow structures on nonslender delta wings, which is not observed on slender delta wings.

2.1.2 Vortex Breakdown

Vortex breakdown, the sudden expansion of vortex core, is one of the major topic that researchers have paid attention for the last several decades on delta wing studies [1], [18]–[22]. The vortical flow over the wing planform significantly contributes to lift force especially for slender delta wings. The deterioration of the vortical structures leads loss of low pressure field on the suction side of planform and eventually leads a decrease in lift force. Although the vortical flow contribution to lift force is smaller on nonslender delta wings, another consequence of vortex breakdown, i.e., buffeting may still cause problems on flow. Vortex breakdown phenomenon is not a special phenomenon observed only on delta wings, but it can be observed in all kinds of swirling flows.

In one of the earliest work on vortex breakdown, the observation and the explanation of the vortex breakdown are given as follows:

“... giving impression that an imaginary spherical body has been placed on the axis of the vortex, around which the fluid is obliged to flow. In practice, the imaginary object is a bubble which takes the form of a slightly elongated sphere of stagnant fluid downstream of which conditions similar to those ahead of it are restored for a short distance until a second breakdown occurs.” [23]

Different explanations of the vortex breakdown phenomenon based on hydrodynamic instability, wave propagation and flow stagnation are summarized in several review articles[19], [24].

There are seven different disruption of vortex core, three of which are widely encountered, i.e., spiral, double helix and axisymmetric (bubble) on delta wing flows. Figure 2-4 demonstrates these common vortex breakdown types. Both experiments and theoretical explanations show that pressure gradient and swirl level are the two main parameters affecting the existence and movement of vortex breakdown [15]. For the case of a delta wing both parameters depend on the wing geometry.

Dominant form of the breakdowns observed on delta wings are spiral type breakdowns. However, bubble type breakdown is also observed. Indeed, these observations are considered as a base for the view that bubble type breakdowns are a form of spiral breakdown forms and may shift from one form to another[25]. Figure 2-5 demonstrates an instance where both forms are observed over a slender delta wing. Smoke or dye visualization experiments are the most common methods in literature to visualize the breakdown phenomenon[26], [27].

2.1.3 Shear Layer Instabilities

The shear layer separated from the leading-edge, which then rolls up to form primary vortex, convects its own instabilities into flow. Gad-el-Hak and Blackwelder [2] showed that primary vortices on delta wings were created by coupling of smaller vortices in the separated shear layer from leading edge. The generation of these smaller vortices are attributed to Kelvin- Helmholtz instability. Other studies [25], [28] confirmed this idea. Yavuz et al [7] revealed shear layer sub-structures by near surface PIV measurements and both vorticity and root-mean-square velocity results indicated that there were small scale fluctuating structures exist along the leading edge. Figure 2-6 illustrates these sub-structures.

This shear layer instability and secondary flows also lead vortex core to wander around a mean location[3].

2.1.4 Shear Layer Reattachment

Flow reattachment is another phenomenon that has vital importance on delta wing aerodynamics characteristics. The separated shear layer attaches to suction side of the wing on both slender and non-slender type delta wings. On slender delta wings reattachment to surface do not exists or the reattachment location is on the symmetry line of the wing, whereas on non-slender delta wings reattachment phenomenon occurs outboard of the symmetry line compared to slender delta wings [3]. The comparative schematics of this phenomenon was given in Figure 1-5. One of the most important aspect of shear layer reattachment is that it is diagnosed to be the main source of buffeting on non-slender delta wings, where it is the instabilities due to vortex breakdown on slender wings [29], [30]. Ozgoren et al. [31] studied the relation between surface buffeting and velocity fields and revealed that the buffeting over the wing is due to unsteady nature of the velocity field, i.e., the fluctuations of normal velocity components over wing planform. Hence it is important to control shear layer reattachment on nonslender delta wings in terms of surface buffeting.

2.2 Flow Control Techniques on Delta Wings

Flow control strategies on delta wing flows are based on delaying or eliminating flow separation, stall, and vortex breakdown, enhancing flow reattachment and vortex formation, or manipulating the shear layer in desired manner. Gursul et al [6] reviewed the flow control mechanisms on slender and nonslender delta wings extensively. Mitchell and Delery [32] also reviewed the flow control strategies with an emphasis on delaying vortex breakdown. Flow control can be done either actively or passively. Active flow control methods require an additional energy

input to the flow field and can be done by blowing or suction of air from the edges or surfaces of the wing, small aspect ratio jets, low or high frequency excitations, plasma actuators and flow surface morphing[6]. Passive control strategies include geometry modifications or material modifications and have the advantage of not requiring an energy input. Common passive control methods can be listed as modification of leading edge [10], modification of trailing edge [33], using elastic materials in planform structure[34] and using flaps[35].

2.2.1 Active Control

Literature has a vast amount of studies on active flow control techniques. Some of the major techniques are to be discussed in this section.

Boundary layer and flow separation control by using acoustic waves is one of the active flow control techniques in literature [36]–[38]. These studies show that fully separated flow at stall conditions can be attached, even if it is partially, to the surface and hence the lift can be increased. However, the stall angle cannot be changed [36]. Another founding via studies is that the main parameter effecting the attachments is not the level of forcing but the frequency of waves and forcing location is [37].

To control the flow structure over the delta wings, momentum addition or subtraction by means of air blowing, suction or jet injection can be applied, and these methods are investigated in the literature by leading edge blowing [22], [39]–[43], trailing edge blowing[44]–[46], surface blowing[47]–[49], fore body blowing [50] along vortex core blowing[51] leading edge/surface suction [52]–[54], jet inject[55], [56].

Moreover, blowing, suction and jet injection can be done in a steady or in an unsteady manner though unsteady blowing has a higher effectiveness [6]. Figure 2-7 illustrates the comparison of steady and unsteady excitations and the results of

control at different locations of wing. Blowing from the leading edge inherently has major effects on vortical structures since the leading edge vortices are fed by the separation which takes place here. Blowing can be performed towards the surface, towards the edge or with coanda effect. These interventions create different effects on flow structures. In the most general way, blowing increases circulation in the flow which increases the strength of vortices in flow and lift force for small incidences. For moderate incidences however, it leads premature vortex breakdown [57]. With coanda, a completely attached flow can be generated at low incidences, eliminating leading edge vortices. For moderate incidences, however, the effect of coanda is not clear [6]. Blowing parallel from leading edge also leads a substantial lift enhancement [58].

Along the core blowing accelerates the axial flow in core and modifies pressure gradient favorably [59]. Trailing edge jet injection also delays vortex breakdown. Since vortex breakdown occurs earlier on nonslender delta wings relative to slender case, the effectiveness of jet decreases with decreasing sweep angle [56].

Suction from the trailing edge reduces the strength of the swirl level and circulation by removing some of the vorticity shed from leading edge and moves the vortex breakdown location downstream for a slender wing [52]–[54]. Figure 2-8 illustrates how surface suction delays vortex breakdown location on a slender delta wing.

Using flaps, as in any other case of control technique is open to novelty. The flaps can be used in the apex [60], through the leading edge [61] or at the trailing edge [35], [62]. All these studies show that using a flap can delay vortex breakdown. A recent study on effects of Gurney flaps on nonslender delta wings shows that the use of flaps improve the induced drag, whereas due to increase in form drag, the overall performance is neutral [35].

2.2.2 Passive Control

2.2.2.1 Bleeding

Bleeding is a relatively simple flow control tool, using the inherent pressure difference between high pressure surface and low pressure surface of the wing by an active or passive manner. Figure 2-9 illustrates a simple bleeding model on an airfoil [63] where the air is directed from pressure side aft to suction side fore. In other words, bleeding could be viewed as an alternative method for blowing or jet injection. Bleeding can be applied passively or actively, in which actuators are used to open-close the bleed holes. One of the pioneering study is presented by Lachmann [64] on slotted wings and ailerons in 1920s . A In the review paper Tanner presents the base bleed as a drag reduction method [65]. Hunter et al [66] studied the effect of passive porosity on tailless fighter aircrafts numerically and showed that passive porosity had a potential to be used as a control effector. Carpenter and Porter [67] investigated the effect of passive porosity theoretically on boundary-layer instability control and obtained a stabilizing effect. Bauer and Hensch [68] investigated the effect of passive porosity experimentally on tangent-agive forebodies. It is shown that porous forebodies eliminates the asymmetric forces experienced by solid bodies. Kearney and Glezer [63] investigated the effect of bleed on a 2-D VR-7 airfoil in static and dynamic conditions from pre to post stall conditions and showed that active bleeding was effective in altering the distributions of aerodynamic forces and moments. Hu et al [69] investigated the effect of passive bleeding in low aspect ratio wings. They studied different slot geometries and showed that the method could be used for eliminating roll oscillations without any loss in aerodynamic performance. Moreover, in the study it is concluded that locating the bleed slots near the leading edge, distorts the separated shear layer, which emanates from the leading edge and form vortices.

2.2.2.2 Bio-Inspiration

Through 4 billion years, nature evolved in many ways to overcome the challenges encountered. From micro scale to macro scale, life exists in many forms in different environments; cetaceans, crustacean and other species; life under high pressure ocean surfaces to microorganisms, from flying animals to swimming insects. All these life forms developed a unique solution against the problems which challenged their existence. From very early on, mankind tried to understand and copy nature to generate solutions for their own problems. Biomimetic or mimicking from nature or biology means biologically inspired design [70]. Figure 2-10 reviews the living organism and their selected functions used in biomimicking studies in literature [70].

With the modern era, scientists and engineers investigated natural fliers and swimmers for both academic and commercial reasons. Vast amount of knowledge is available about flow physics of these organism in biology literature with little or no emphasis on how technology may benefit. Moreover, newly introduced measurement techniques, such as PIV, helps scientists and engineers to draw a full picture of the flow physics around these living organisms. Hence, the interdisciplinary studies dramatically increased for the last decades in order to benefit from the design strategies of nature. 1990s introduced micro air vehicles (MAV) technology which shares similar properties with natural fliers in terms of dimensions, weight and speed and flight regime [71], accelerated the co-operation of biologists and engineers.

2.2.2.2. a Geometry Modifications

There have been numerous studies on the hydrodynamics and aerodynamics of the wings/tails of animals in literature[71]–[76]. However, the engineering applications of the insight gained from these studies are quite limited. Very few

studies have considered passive control methods based on naturally inspired geometry modifications on delta wings. Leading edge tubercles on flippers of humpback whales are shown to be quite effective in delaying stall [77], [78]. Straight sharp leading edges of non-slender delta wings of 50° are modified into a sinusoidal forms inspired from humpback whales and it is concluded that even for small protuberances on leading edge, flow topology alters significantly [79] and recovery of reattachment is achieved with sinusoidal leading edges at high angle of attacks where three-dimensional separation is observed for the straight leading edge planform. Study on a 52° swept delta wing with sinusoidal leading edge shows that there exists multiple leading edge vortices, each shed from the geometric peaks on leading edge [80]. These vortices are relatively weaker in strength than the dual vortices observed on a straight leading edge wing, however they last longer without breakdown. It is concluded that these multiple vortex structures may be the reason for delaying stall.

In the present study, it is aimed to control the flow structure and particularly to delay stall on a non-slender delta wing by passive control, i.e. geometry modification inspired by nature. Due to the planform similarity with delta wings, cetacean flukes are chosen for mimicking in geometry modification. Figure 2-11 demonstrates the variety of fluke shapes of cetaceans and the geometric similarity between the planform shape of modern delta wing aircrafts and the flukes are obvious. Sweep angle of flukes may change from 5° to 47° [72]. The definitions of sweep, chord on fluke geometry is presented in Figure 2-12.

Comparing flying animals with swimming animals, it is observed that flying animals, which move in a low-density medium, evolved to have high lift forces whereas for a swimming animals, which move in a higher density medium, evolved to minimize the generated drag. However it is indicated that there exists methods that animals living in these different mediums use in common, such as leading edge vortices (LEV) to delay stall [81]. In addition, although the flukes are used to generate thrust in general, they are evolved to act as hydrofoils and

have moderate aspect ratio, low sweep, and flexibility which enable them to obtain high lift to drag ratios [72]. The stall condition is witnessed on whale flukes around 20° of attack angle under steady flow conditions, which can be extended to over 30° when the fluke oscillation is applied [82]. Flow control mechanisms of swimming animals including geometry modifications are studied and reviewed in literature [83], [84]. The hydrofoil shape of fluke of a narwhal and its hydrodynamic behavior is investigated and concluded that complex relationships among drag, lift, delay in stall, and thrust production depend on various parameters such as sweep angle, aspect ratio, thickness ratio, and shoulder position [85]. Moreover, while flukes oscillate, they experience chambering which can allow functioning without stall [82].

2.2.2.2.b. Flexion Ratio-Flexible Wings

Aero-hydro dynamics around flexible materials can be considered as a recent topic compared to aero-hydrodynamics around rigid materials as most of the current flight technology depends on rigid geometries. However, due to increasing need of higher maneuverability, higher lift force, delaying stall, search for different strategies raised the use of flexible materials. For large scale objects flexibility is considered to be an unwanted property [86]. However, for small sized objects at low Re number, flows are not limited in terms of geometry compared to larger objects.

Flexible propulsors such as flukes, whose propulsive efficiencies are around 0.75-0.9, are expected to be used to increase thrust production and propulsive efficiency of the commercial rigid counterparts whose efficiencies are around 0.7 [87]. Chordwise flexibility, which leads an increase in leading edge suction [88], increases propulsive efficiency by %20 [89][88], indirectly increases thrust component of lift with a trade of small decrease in thrust.

Flyers such as birds use their flexible wings and feathers to adjust their wings for desired flight conditions [71]. Bats use comparably more complex tools such as flexible membranes, flexible bones and two dozens of independently controlled joints to adjust the wings for the desired flight performances including changing the chamber of the wing, flying both in negative and positive angle of attack [90]. Recently bat-inspired membrane wing studies draw an increasing attention due their high maneuverability capabilities [91]–[94].

The nature's solution for flying problem may be adapted for the applications in manmade aircrafts, especially in MAVs. Stanford et al [95] reviewed the current state-of-art for membrane wings. Comparison of a lift coefficient for flexible wing with a rigid wing is presented in Figure 2-13, which shows that flexible wings have better lift coefficient characteristics under high angle of attacks. Water tunnel studies conducted over rectangular flexible wings show that spanwise flexibility leads to an increase in efficiency [96], however, extensive flexibility may adversely affect the flow and lead a decrease in efficiency as illustrated in Figure 2-14.

Gray et al [97] investigated aero elastic response of both half and full span slender delta wings and reported that second and third mode vibrations dominate the planform when the breakdown is over the wing, where for full wings only the second mode of vibration is dominant. Figure 2-15 demonstrates the results of experiments conducted on delta wings for a broad range of sweep angle and attack angles. The studies on non-slender delta wings [34] show that flexible wings may delay the stall angle for a full wing. However, experiments on half wings fail to recover flows for same conditions. Figure 2-16 demonstrates the comparison of physical response of a flexible wing to flow under different attack angles. The figure shows that the full wing experiences significant oscillations contrary to the half wing. Hence it is concluded that a second mode antisymmetric oscillation is required to benefit from flexibility.

In this particular study, it is aimed to control the flow structure and particularly to delay stall on a non-slender delta wing by passive control, i.e. material modification inspired by nature. A recent investigation [98] shows that the natural fliers and swimmers obey the same bending rules, being independent from the scale of the organism or the fluid medium. Figure 2-17 demonstrates the flexion ratio and flexion angle concept, as well as their value for a broad range of swimmers and fliers and, Figure 2-18 shows that the bending patterns, flexion ratios and flexion angles obtained, are independent from the scale of organism, the fluid medium and the taxonomic group from top to bottom respectively. Since it is impractical to design a flexible planform which experiences a second mode antisymmetric oscillation to enhance flow characteristics as aforementioned, an alternative approach for using flexibility; using the bending rules in nature is proposed and studied.

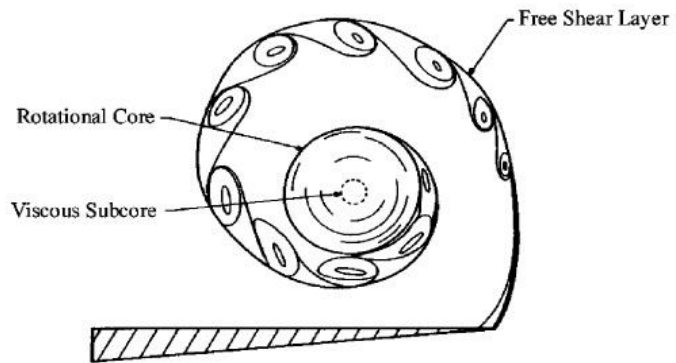
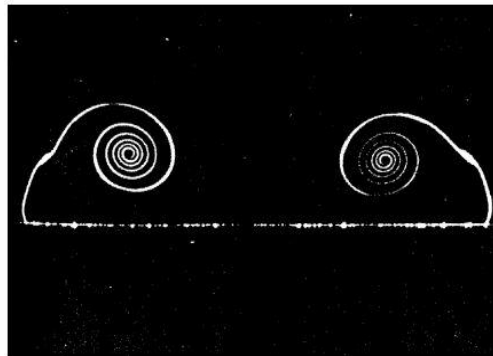


Figure 2-1 Shear-layer separation and formation of leading edge vortex [99] [100].

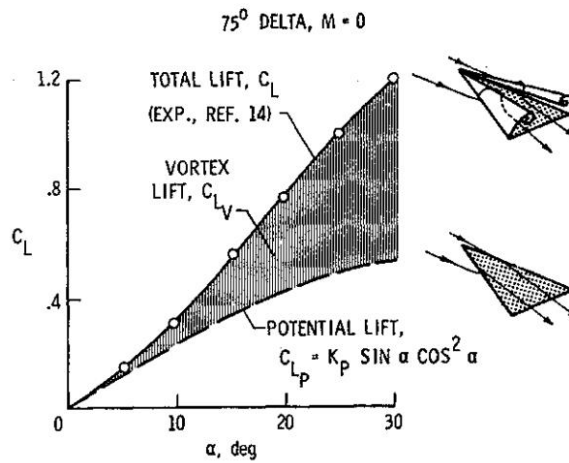


Figure 2-2 Illustration of vortex lift contribution to lift coefficient according to Palhaums vortex lift theory [17] .

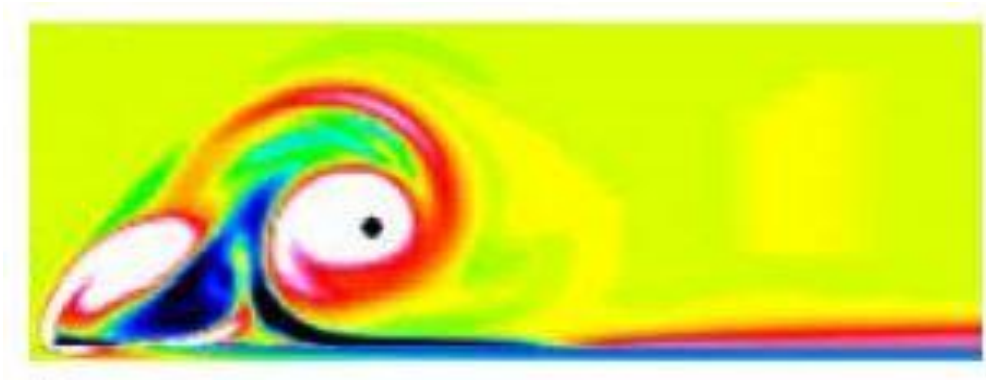


Figure 2-3 Axial vorticity patterns of a dual vortex structure [3].

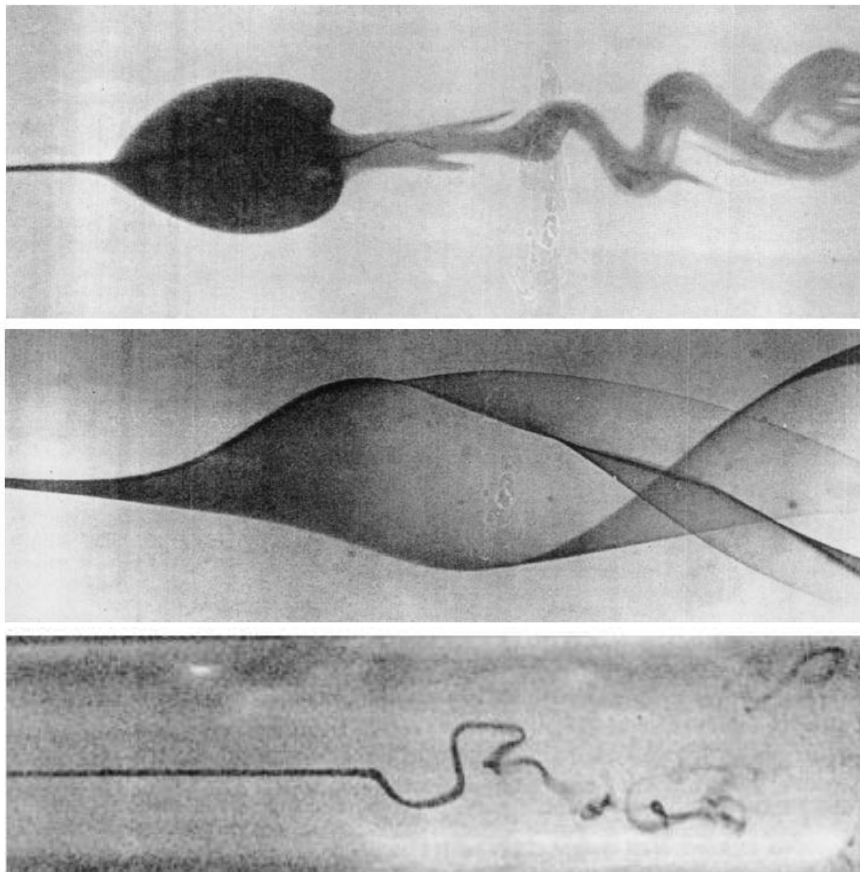


Figure 2-4 Illustration of bubble, double helix and spiral type breakdown from top to bottom respectively [23]

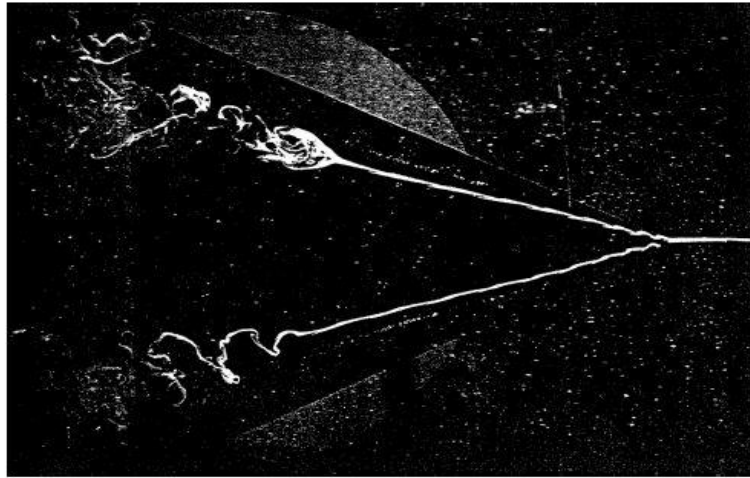


Figure 2-5 Visualization of both spiral and bubble vortex breakdown on a slender delta wing [15].

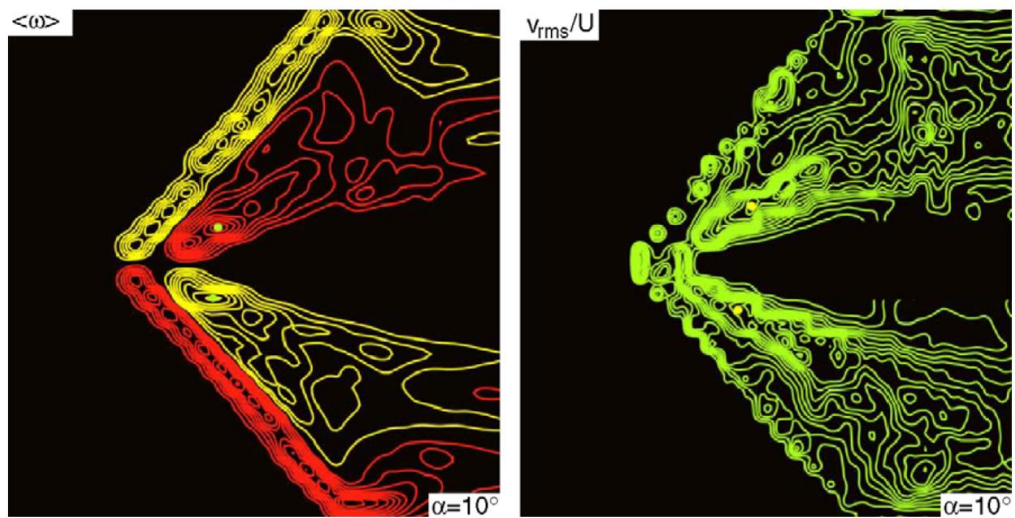


Figure 2-6 PIV measurement results of shear layer sub-structures for a 38.7 deg swept delta wing [7]

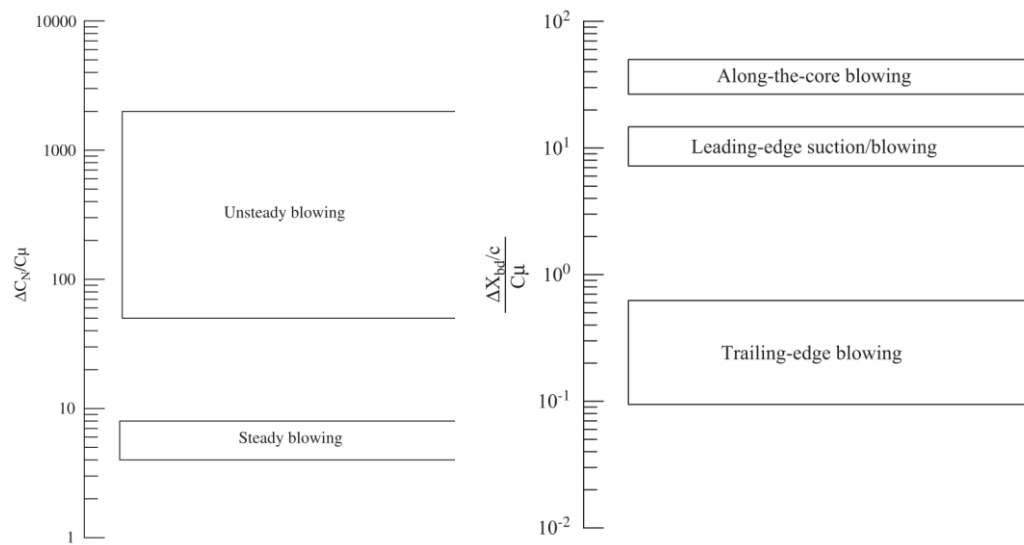


Figure 2-7 Effectiveness of (left) steady and unsteady blowing (right) blowing-suction methods [3].

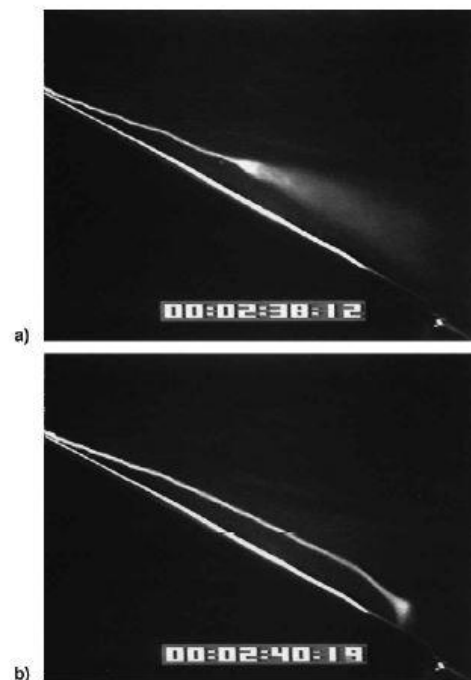


Figure 2-8 Effect of suction on vortex breakdown location (a) without suction (b) with suction [54].



Figure 2-9 Bleed through the airfoil [63]

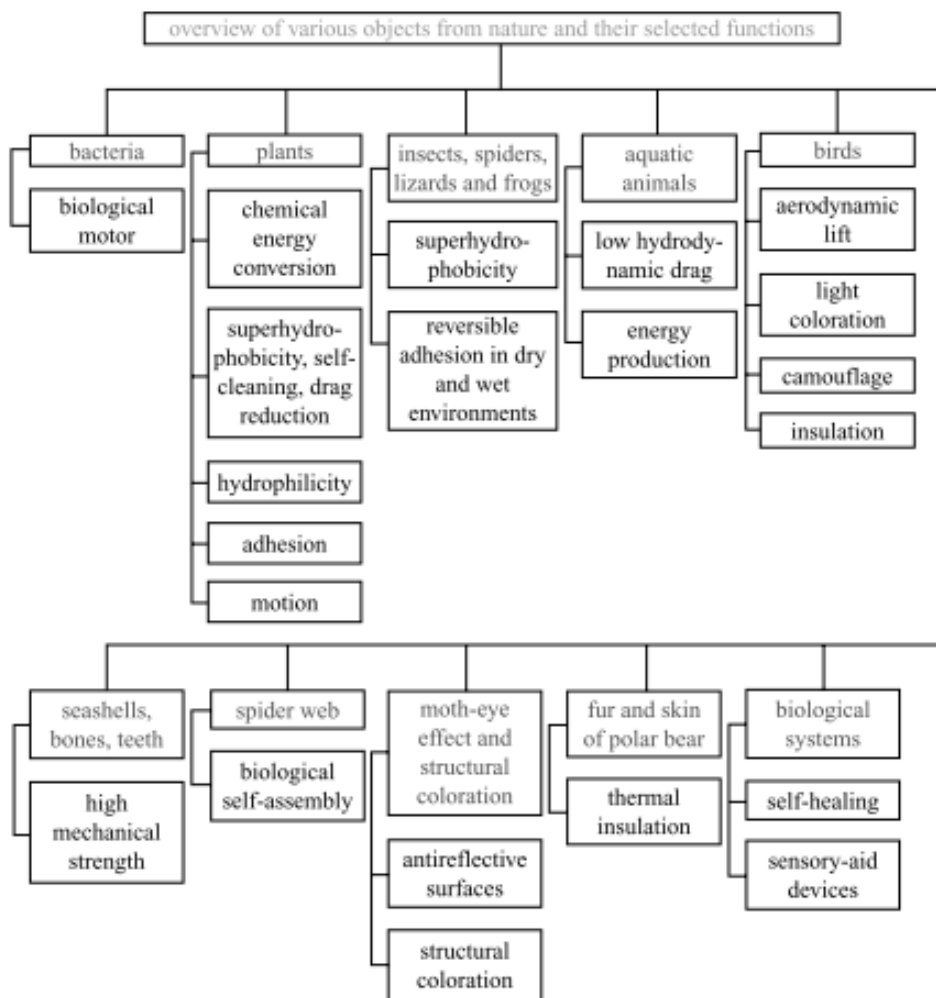


Figure 2-10 Overview of the objects and their corresponding functions in nature [70].

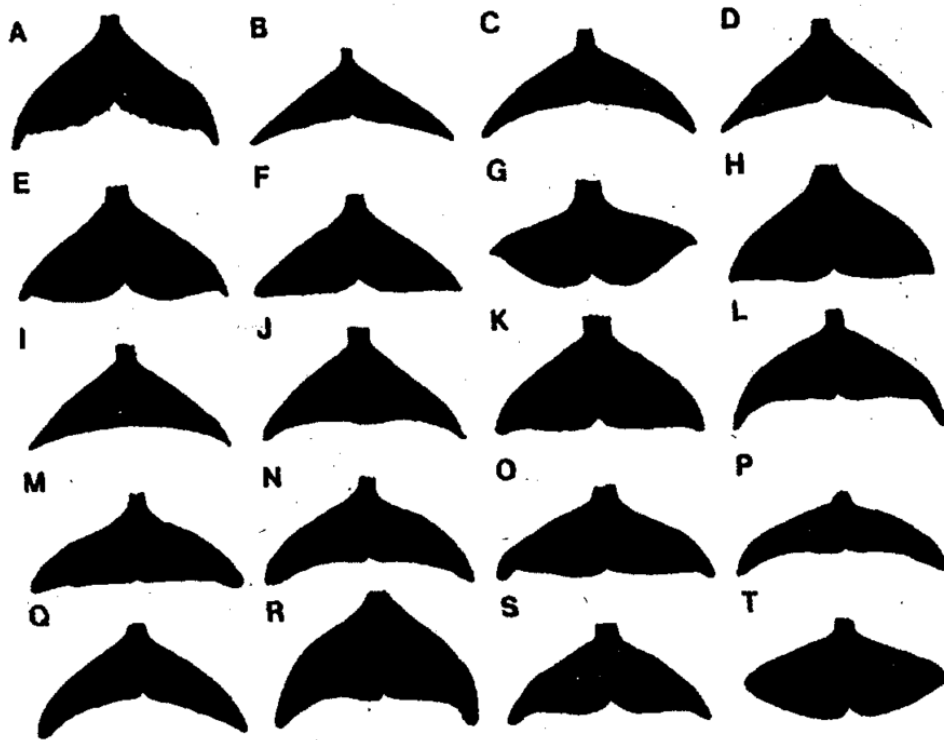


Figure 2-11 Planform of flukes from representative cetacean species [101].

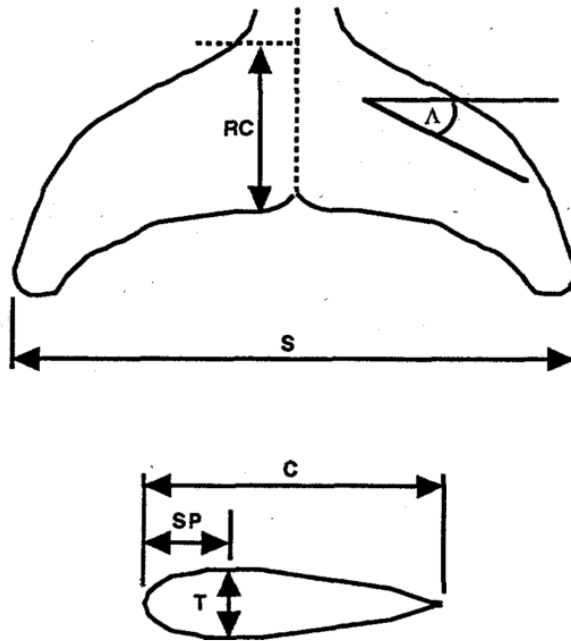


Figure 2-12 Fluke dimensions of planform (top) and cross sectional view (bottom) [101].

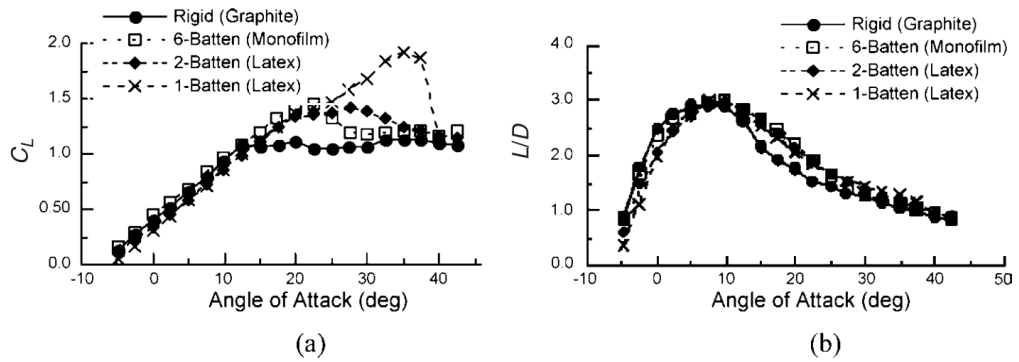


Figure 2-13 Comparison of lift coefficient and L/D ratio of rigid and flexible wings of different stiffness [102].

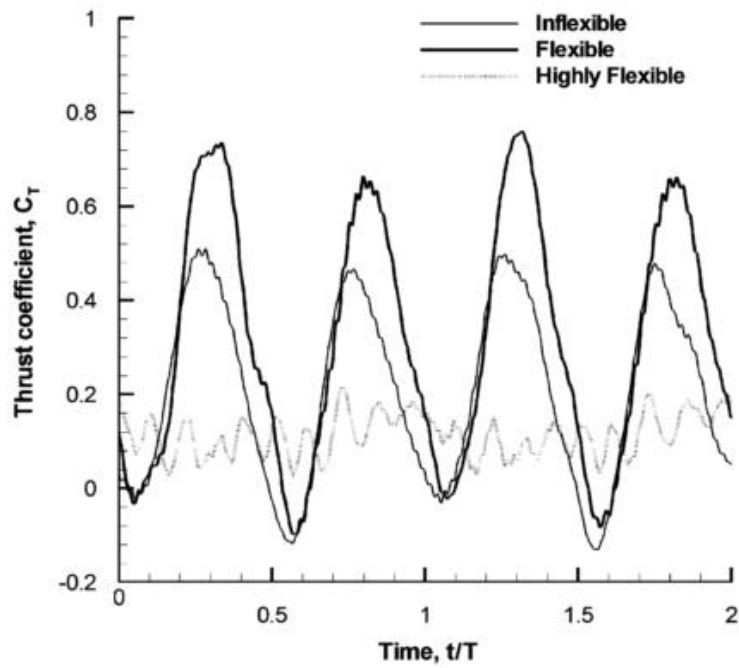


Figure 2-14 Thrust coefficient as a function of heave for a inflexible, flexible and highly flexible wing [96].

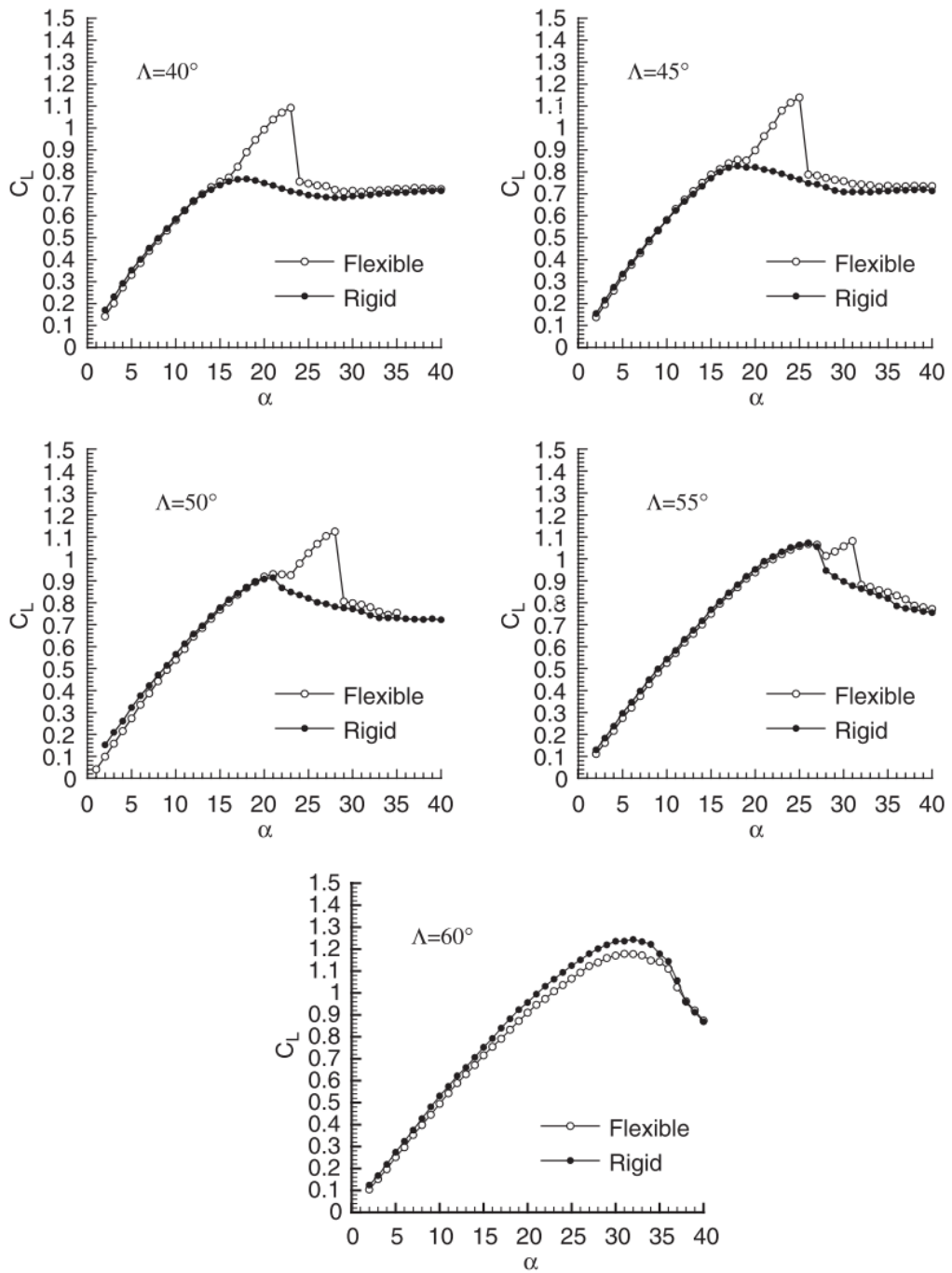


Figure 2-15 Comparison of lift coefficients for rigid and flexible delta wings of different sweep angle [34].

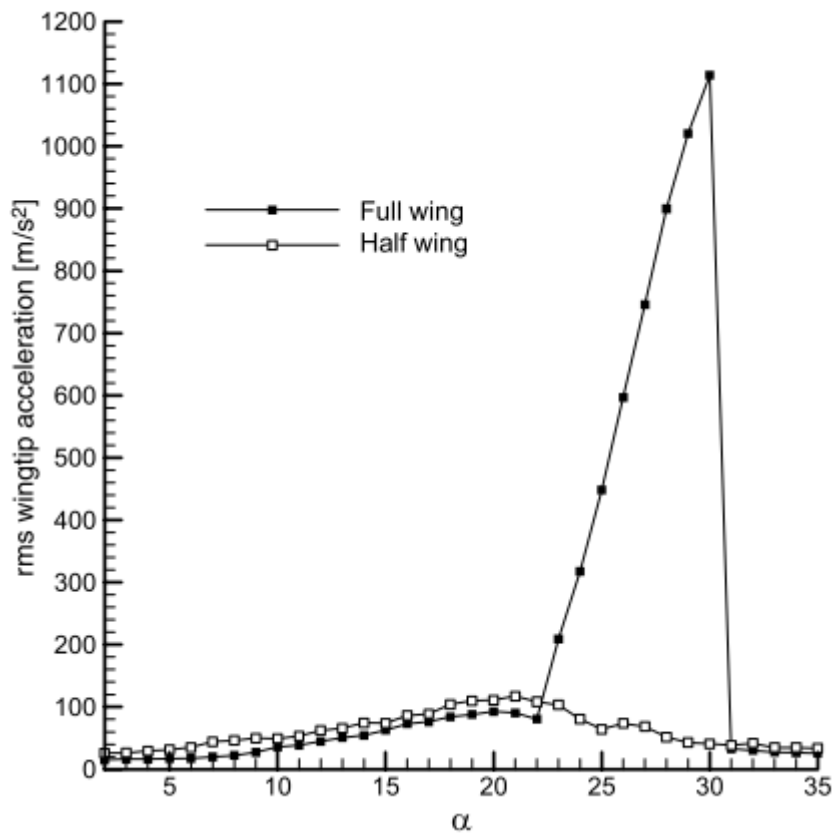


Figure 2-16 Comparison of effect of flexibility on half wing and full wing[34].

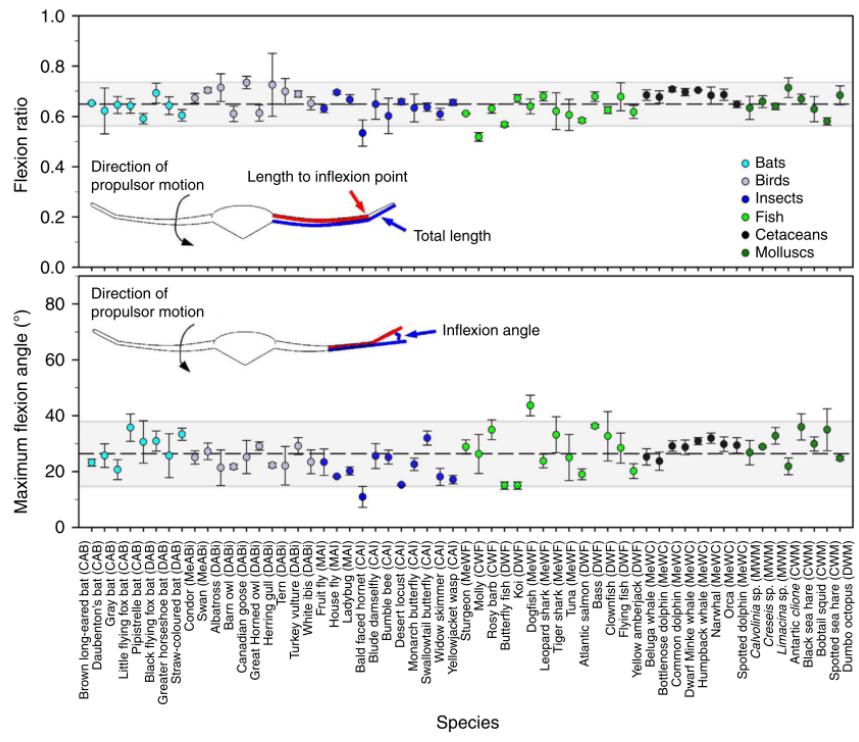
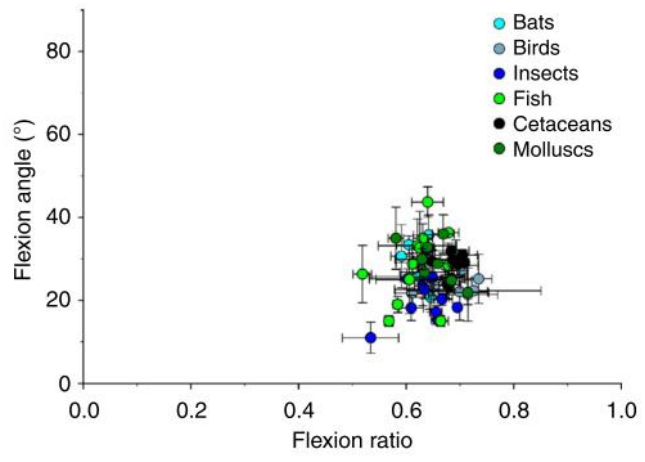


Figure 2-17 Flexion morphospace (top) and patterns of propulsor bending by variety of animals moving steadily through air and water (bottom) [98].

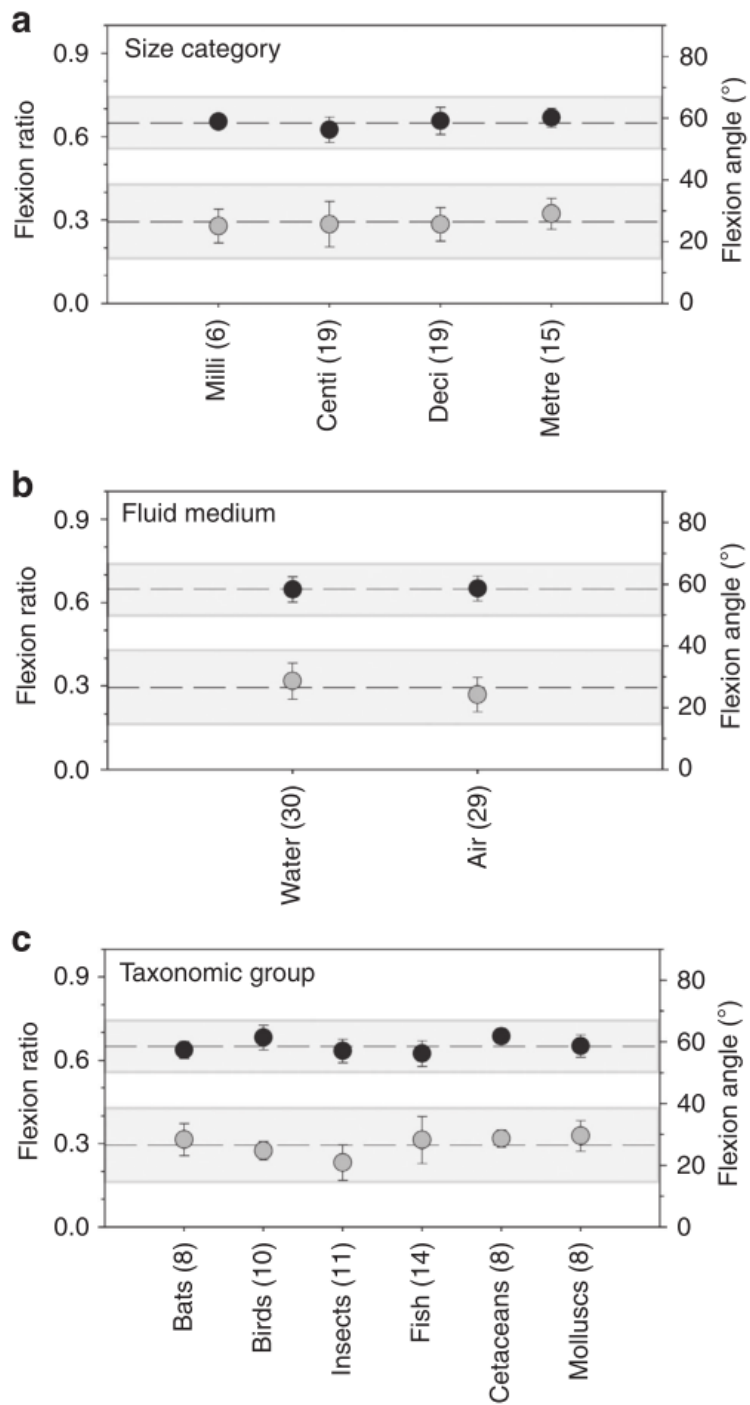


Figure 2-18 Generality of bending patterns across a variety of animal categories [98].

CHAPTER 3

EXPERIMENTAL SET-UP AND TECHNIQUES

This chapter provides the technical details of the experimental set-up and the measurement systems used in the current study along with the experimental matrix for each method.

3.1 Wind Tunnel

Experiments were conducted in a low speed, suction type, open circuit wind tunnel facility, driven by an axial fan and a 10kW AC motor, located at the Fluid Mechanics Laboratory of Mechanical Engineering Department at Middle East Technical University. The images of the laboratory and wind tunnel is demonstrated in Figure 3.1.

The wind tunnel has two entrances covered with fine grid screens. The 2700 mm long entrance section has three additional screens and a honeycomb in order to create a uniform flow with low turbulence intensity in the test section. The 2000 mm contraction cone has the ratio of 8:1.

The test section is made of plexiglass, which allows full transparency for PIV and flow visualization experiments from top, bottom and sidewalls and has dimensions of 750 mm width, 510 mm height and 2000 mm length. The test section speed can be adjusted between 1 m/s and 30 m/s by a frequency controlled fan unit. The three-dimensional drawing of the test section with a mounted wing is illustrated in Figure 3-2.

After the test section, the air is expanded and decelerated via 7300 mm long diffuser, which leads an increase in static pressure and decrease in the power required to run the tunnel.

The tests were conducted at various free stream velocities and the corresponding Reynolds numbers were calculated based on the wing chord length via Equation 3.1.

$$Re = \frac{U_{\infty} C}{\nu} \quad (3.1)$$

3.1.1 Wind Tunnel Characterization

The wind tunnel characterization was performed using Laser Doppler Anemometry (LDA), which were also compared with pitot-static tube measurements. The measurements were taken at a fixed point in the test section. The velocity calculation from the pitot-static tube was calibrated by considering the environmental conditions such as temperature, humidity and atmospheric pressure of the laboratory during experiments. Figure 3-3 shows the average velocity against tunnel power along with the turbulence intensity values. The characterization shows that the linearity of the tunnel velocity versus fan power starts above 4%. The maximum turbulence intensity obtained in the test section was 0.9%. The results of LDA and pitot-static tube measurements differed around 3%.

3.2 Flow Measurement Techniques

3.2.1 Laser-Illuminated Flow Visualization

Flow visualization method, pioneered by Leonardo da Vinci, is a widely used simple tool in order to understand the behavior of flow structures qualitatively.

The opportunity to see the patterns of flow in the region of interest would always give an insight for the solution the problems. Broadly speaking, the flow visualization is divided into two categories; surface flow visualization and flow field visualization. Surface flow visualization is performed on the surface in order to obtain critical information on flow topology such as, critical points, stagnation points, separation or attachment lines etc. Surface flow visualization can be performed by using tufts, mini-tufts, oil, china clay. Unlike surface flow visualization, flow field visualization allows to obtain qualitative data about the flow structures over the whole domain except the surface. For flow field visualization tufts, hydrogen bubbles, smoke or dye can be employed. If tracer particles such as smoke or dye are used, the particles should be neutrally buoyant. Figure 3-4 illustrates examples of laser-illuminated flow visualization, tuft visualization, dye visualization and surface visualization by oil.

In the visualization experiments of this study, a laser-illuminated smoke visualization technique was performed both for cross flow and surface flow. The schematic of cross flow visualization set-up is illustrated in Figure 3-5. A commercial smoke generator was used for the experiments. The smoke, generated by vaporizing liquid paraffin with a commercial smoke generator, was pressurized by a CO₂ pressure tank with a check valve to feed the wing at the desired amount. A diode-pumped solid-state green laser with a 532 nm wavelength and 400mW power output was used in the study for illumination to obtain a sufficient laser beam, which was converted to laser sheet by means of a cylindrical lens. A relatively thicker laser sheet, on the order of 5 mm, was obtained to have a sufficient illuminated region for surface-flow and crossflow smoke visualizations. The images were captured by Nikon 650D Digital Single Lens Reflex Camera (DSLR). The images were then post-processed (color conversion) by using the commercial software Adobe Photoshop.

3.2.2 Surface Pressure Measurements

Netscanner 9116 Intelligent Pressure Scanner was used for the surface pressure measurements. Device has 16 silicon piezoresistive pressure transducers, which allows to make up-to 16 channel pressure measurements. The measurement range of the piezoresistive pressure sensors is 0 to 2.5kPa. This device was pre-calibrated over certain pressure and temperature spans by the supplier. However, measurements with manometer were also conducted to confirm the pressure scanner results. The calibration settings of each transducer were stored in the EEPROM (Electrically Erasable Programmable Read-Only Memory). Integrated microprocessor and the temperature sensors enable the device to compensate the transducer outputs for offset, nonlinearity, sensitivity and thermal effects prior to transferring data to the computer. The system ensures a measurement resolution of $\pm 0.003\%$ FS (full scale) and accuracy of $\pm 0.05\%$ FS.

The tubing length from pressure scanner to wing is on the order of meters and may cause a damping effect in unsteady measurements. In order to be sure about the unsteady response of the scanner, the spectral analysis was performed for a periodic blowing study in the laboratory and it was observed that the fluctuations induced by periodic blowing could be captured. For all experiments, the data was recorded at a 500 Hz sampling rate for 10 seconds. The experiments were conducted several times and averaged. Initial experiments showed that averaging of 2 data sets led to saturation of results and more data sets did not create a significant change in the results. The noise of the environment was also measured with the same sampling rate and time, and subtracted from the data for each experiment.

The results of the pressure data were presented as dimensionless pressure coefficients values C_p which is calculated via Equation 3.4. For the corresponding pressure distribution charts the C_p values were shown as $-C_p$ that plotted against the dimensionless spanwise location of the pressure tabs. Pressure fluctuations are

presented in terms of $C_{p,RMS}$ values, where root mean square (RMS) values of the measured pressure data is calculated and nondimensionalized as in Equation 3.6. $C_{p,RMS}$ values were also plotted in same manner to provide information about the unsteady behavior of the pressure distribution.

$$C_p = \frac{\bar{p} - p_\infty}{\frac{1}{2}\rho U^2} = \frac{\bar{p} - p_\infty}{p_{dyn}} \quad (3.4)$$

\bar{p} : Time averaged surface pressure

p_∞ : Static pressure of the flow

p_{dyn} : Dynamic pressure of the flow

ρ : Fluid Density

U : Free Stream Velocity

$$C_{pRMS} = \frac{\sqrt{\frac{\sum_{i=1}^N (p_i - \bar{p})^2}{N}}}{p_{dyn}} \quad (3.5)$$

N : Number of samples

3.2.3 Particle Image Velocimetry (PIV) Measurements

PIV is an experimental technique, which measures the instantaneous scalars and vectors of a fluid field. Among the experimental techniques in fluid mechanics, PIV is under a broader class called pulsed-light velocimetry, in which velocities are measured by measuring the motion of small particles suspending in fluid

domain. Figure 3-6 illustrates where PIV stands among other pulsed-light velocimetry techniques [103].

In PIV system, seeding particles, which are assumed to be following the fluid streams, are illuminated by a laser sheet and images are taken from this illuminated field in short time intervals by a frame grabber controlled camera. Tracking the particles and determining their traveled distance during the pre-determined time interval allows to compute the velocity vector for the particle. Performing this calculation for the whole field of interest allows to generate velocity vector field of the region of interest.

The entire experimental procedure of a PIV measurement can be discretized for a better understanding. Once the motion is generated in fluid medium, the data acquisition is performed by using seeding, laser, and camera. After the data acquisition step, obtained raw images are processed to obtain velocity vectors. Finally the post-processing is performed including the further analysis of the obtained velocity fields. Figure 3-7 illustrates all the steps of a sample experiment from data acquisition step to post-processing step. Further information on specific steps of the procedure is also explained below.

In this study, a TSI PIV system was used and cross flow PIV experiments were employed to generate quantitative flow patterns, primarily velocity vector fields, at chordwise distance $x/C = 0.5$ for bleeding and flexion ratio studies. The PIV system consists of seeding particles, a double pulsed laser, a digital CMOS camera, a frame grabber, a synchronizer and a computer with software. The schematics of the experimental set-up is presented in Figure 3-8.

Data acquisition starts with generation of the flow and seeding the flow field with tracer particles. In this study, the flow was seeded with glycol based smoke which is expected to produce particles of diameter $1 - 3\mu m$ by using a commercial smoke generator [104]. Once the seeding is homogenous in flow field, the camera

and laser is triggered via software to capture the image pairs. The imaging process, i.e. illumination and recording, can be done in different methods and called “pulse-coding”. The possible pulse-coding strategies are shown in Figure 3-9. In this study, a double-frame double exposure imaging was used. In this imaging technique, the images taken at times t and $t + \Delta t$ are recorded as two separate images. The most important parameter in a PIV measurement is the time separation between two laser shots, Δt , which simply defines the velocity range that can be measured. In any PIV experiment the following points about seeding and Δt value should be taken into consideration during data acquisition:

- The seeding particles should be homogenous for statistical analysis.
- Interrogation areas must be large enough to represent the field, and small enough to ensure that there is no velocity gradient.
- There should be 15-20 particles in each interrogation area. Less particles will lead to a Particle Tracking Velocimetry system, higher densities will lead to particle Particle Speckle technique in which signal to noise ratio decreases (S/N).
- The separation time Δt should be large enough to represent the flow accurately and small enough to ensure that particles do not move outside of the interrogation area. As a common rule, the particles should move less than one-fourth of the interrogation window. Moreover, to avoid out-of-plane motion, the laser sheet should be four times thick of the maximum displacement.

The illumination in the experiments was provided by a dual-pulsed Q-switched Litron Nano L200-15 200mJ Nd:Yag laser system. The laser sheet thickness, the focal distance, and the orientation were generated by transmitting the laser beam through a cylindrical lens of -15 mm and a spherical lens of 1000 mm. For image acquisition, a high-speed 2K X 2K Powerview™ Plus 4-megapixel CMOS camera with a Nikon 50mm F1.8 lens was used at the rate of 15 double frames/s. The camera was located outside of the wind tunnel and thus a mirror, located at 7

times the chord distance away from the wing, was used to acquire the images. Preliminary tests were performed to ensure that the mirror had no influence upstream in the flow over the wing. TSI LaserPulse™ 610036 synchronizer was used for synchronization of laser and camera. The images captured by the camera are digitally stored by frame grabber in RAM. The data transfer routes for the explained PIV configuration is presented in Figure 3-10.

The images were processed via commercial software TSI Insight 4G with an extension package of TSI Tecplot FocusPIV to obtain velocity vectors, V . As mentioned before, the detailed flow chart of processing and post-processing is demonstrated in Figure 3-7. The patterns of instantaneous velocity vectors were evaluated by a frame-to-frame cross-correlation technique from raw images. An effective overlap of 50% was employed to satisfy Nyquist criterion. The interrogation area was 16 x 16 pixels which corresponded to the effective grid size of $\Delta/C = 0.022$ for both bleeding and flexion ratio experiments. In this study, an FFT based cross-correlation algorithm was applied to process the data (raw images). An alternative algorithm, Hart correlation was also available in the software. To understand and quantify the difference between two-different algorithms, one of the experiment results were processed by both methods and the corresponding results of time-averaged streamlines, velocity vectors and contours of non-dimensional vorticity are presented in Figure 3-11. Both algorithm resulted in very similar vector fields and stream line patterns with minor differences. The vorticity patterns were very similar and the peak values of vorticity concentration were same, independent from the algorithm. Hence either algorithm could have been used for data processing.

After processing each pair of frames with FFT cross-correlation algorithm, a post-processing operation is necessary for both removing bad vectors and creating vectors by interpolation for the interrogation windows where the initial FFT process failed to obtain velocity vectors. The post-process procedure includes vector validation and vector conditioning which could be performed either locally

or globally. In this study, local vector validation and vector conditioning was applied. For an interrogation window, local vector validation gathers information from neighboring cells and calculates a reference vector. Then the difference between the reference vector and the vector in the interrogation area is calculated and checked for a defined difference. If the difference is greater than the pre-set value, validation is failed. Local vector validation was performed by TSI Insight 4G™ software, by a median test in neighboring size of 5 x 5. After vector validation, vector conditioning was applied. The main aim of the vector conditioning is to fill the holes due to failed SNR or failed validation procedure. In the experiments of this thesis, vector conditioning was performed by TSI Insight 4G™ software using a recursive filling method in a neighboring of 3 x 3. After calculating the instantaneous velocity field V within desired conditions, vorticity and streamline patterns can be calculated based on velocity vector field for each image pair.

Completing the processing and post-processing routine for all image pairs obtained, 200 image pairs for this study, time-averaged velocity field $\langle V \rangle$ can be calculated. In this study, post-processing was performed with the Tecplot add-on produced specifically for TSI PIV software called TSI Tecplot Focus on PIV. After calculating $\langle V \rangle$, time-averaged vorticity $\langle \omega \rangle$, and time-averaged streamline patterns $\langle \Psi \rangle$ were calculated via the same software. Moreover, to obtain velocity fluctuations, which is directly related to buffeting on wing planform, [105] root-mean-square vectors were needed. However, the TSI Insight 4G™ does not have a package for root-mean-square calculation. Hence a Matlab code was generated which read the vector files created by the PIV software, calculated the v_{rms} value according to Equation 3.6 and returned to a file which could be read by Tecplot. The code is supplied in Appendix C. A schematic about how to calculate v_{rms} is presented in Figure 3-12.

$$v_{rms} = \sqrt{\left\{ \frac{1}{N} \sum_{n=1}^N [v_n(x, y) - \langle v(x, y) \rangle]^2 \right\}} \quad (3.6)$$

3.3 Experimental Matrices and Delta Wing Models

This PhD thesis consists three different novel passive flow control technique studies, namely bioinspired edge modification, bioinspired material modification, and passive bleeding. Earnshaw and Lawford [14] studied the boundary layer states over delta wings with sweep angles ranging from 55 deg to 76 deg for the Reynolds number range of $4.5 \times 10^5 < Re < 9 \times 10^5$ emphasizing that the boundary layer state strongly depends on the flow structures over the wing including leading edge vortex, three-dimensional separation, and etc. In line with this observation, the boundary layer state in the present study is expected to be both turbulent and laminar at different regions on the wing surface for different cases tested.

Each study has its own planform, experimental matrix and corresponding measurement technique. In this part the measurement techniques, the experimental matrices and the delta wing models for each study is addressed and clarified

3.3.1 Edge-Modification Experiments-Part I & Part II

In the present study, it is aimed to control the flow structure and particularly to delay stall and prevent flow separation on a non-slender delta wing by geometry modification inspired by nature. Leading edge vortices (LEVs), which is generated on wings, flukes or other propulsors, are a common tool that both flying and swimming animals use to delay stall [81]. Although flukes are used to generate thrust in general, they are evolved to act as hydrofoils and have moderate aspect ratio, low sweep, and flexibility which enable them to obtain high lift to

drag ratios [72]. Due to the planform similarity with delta wings, cetacean flukes are chosen for geometry mimicking. As mentioned before, Figure 2-11 demonstrates the variety of fluke shapes of cetaceans and the geometric similarity between the planform shape of modern delta wing aircrafts.

The effect of edge modifications were investigated for a broad range of Reynolds numbers and attack angles via laser-illuminated flow visualization experiments. Figure 3-13 presents the six different wings, made of fine polyamide PA2200, manufactured using rapid prototyping for both the first and the second part of the investigation. Experimental matrices for both parts are presented in Figure 3-14. Experiments were conducted to study the effect of attack angle from $\alpha = 4^\circ$ to $\alpha = 12^\circ$ and Reynolds number from $Re = 10^4$ to $Re = 2.5 \times 10^4$. The free stream velocities are 1.33 m/s, 2 m/s, 2.67 m/s, 3.33 m/s for $Re = 10^4, 1.5 \times 10^4, 2 \times 10^4$ and 2.5×10^4 respectively. The sketches of the planforms used in Part I are demonstrated in Figure 3-15. A 45-degree sharp edged delta wing was chosen as the reference wing configuration to compare the results of modified wings and indicated as base wing (BW). The trailing and the leading edges of the base wing were modified such that the wing configuration turn into the white-sided dolphin fluke shape obtained from the literature, which is shown in the top portion of Figure 3-15. The apex region of the geometry, which was bonded to the fluke of dolphin, was converted to the sharp 45-degree sweep geometry as seen in the mid-section of Figure 3-15. The location where the transition took place from the original fluke geometry to sharp 45-degree geometry was approximated such that the original fluke geometry information was maximized. This wing configuration was named dolphin fluke (DF). For the DF and modified dolphin fluke (MDF) planforms, the transition to fluke geometry started at 18% of the chord distance. To evaluate the effect of trailing edge modification on flow structure, a modified version of the dolphin fluke wing configuration, indicated as modified dolphin fluke (MDF), was produced. The trailing edge of the MDF planform starts at 66% of the chord distance where it has a width of 53 mm. The chord lengths of three planforms were kept same as 118 mm. The span of the base wing was 236 mm

and the maximum span of the dolphin fluke model (DF) and modified dolphin fluke model (MDF) was 151 mm. The thickness of the wings was 5mm and the leading edges of the wings were beveled on the windward side at an angle of 45° . The maximum blockage ratio occurred for the base planform at the highest attack angle of $\alpha = 12^\circ$ and is 0.6%.

The overview of the base wing model along with laser sheet orientations for surface flow visualizations and cross flow visualizations are shown in bottom part of Figure 3-15. Two different flow visualizations, cross flow and surface flow, were performed, where the laser sheet was positioned perpendicular to the test section at $x/C = 0.32, 0.55$ and 0.77 and parallel to leading edge vortex core, respectively, where C represents the chord of the wing. Images captured by a DSLR camera (Digital Single Lens Reflex Camera). For surface flow visualizations, the camera was positioned parallel to the laser sheet. For cross flow visualization, a mirror was located five cord distance downstream of the wing with an angle of 45° to free stream to take cross flow pictures with the camera located outside of the test section. The camera pictures were processed by using Adobe Photoshop for black and white conversions. Preliminary tests were performed to ensure that the mirror had no influence upstream in the flow over the wing.

After completing the first part of the study, which investigates the effect of leading and trailing edge modification together, a second set of experiments were conducted to understand the effect of individual modifications of leading edge and the trailing edge. The sketches of the planforms are demonstrated in Figure 3-16 along with the previously studied planforms. The wing configurations were named as OL (Only Leading Edge), OT (Only Trailing Edge) and OTE (Only Trailing Edge Expanded). The schematic drawings of the planforms are presented in the mid-section of Figure 3-16. OL planform had exactly the same leading edge with DF planform, with a trailing edge similar to that of Base planform, whereas OT planform had the same leading-edge configuration with Base

planform and a part of the trailing edge is cut-out to mimicked the same trailing edge shape of DF planform. OTE planform had the same leading-edge shape with Base planform, but the trailing edge was modified such that the cut-out part on OT planform is scaled-up up-to leading edge. Surface flow visualization were performed, where the laser sheet was parallel to leading edge vortex core. The overview of the base wing model along with laser sheet orientations for surface flow visualizations is shown at the bottom part of Figure 3-16. The data acquisition and the post-process of the raw data were the same with the first part of the experiments.

3.3.2 Bleeding Experiments

Bleeding is a relatively simple flow control tool, using the inherent pressure difference between high pressure surface and low pressure surface of the wing by an active or passive manner via internal passages. The high pressure air interacting with the low pressure region and cross flows over the planform has the potential to alter pressure field on suction side. As previously presented in Chapter 2, Figure 2-9 illustrates a simple bleeding model on an airfoil [63] where the air is directed from pressure side aft to suction side fore. In other words, bleeding could be viewed as an alternative method for blowing or jet injection.

To characterize and study the effect of passive bleeding over a 45 deg swept delta wing, Particle Image Velocimetry (PIV), pressure measurement and laser-illuminated flow visualization experiments were conducted. Four delta wing models of 45 deg sweep, made of fine polyamide PA2200, were manufactured using rapid prototyping and are presented in Figure 3-17. The geometric details, which are explained in detail below, with bleed hole locations are presented in Figure 3-18 and the experimental matrix is presented in Figure 3-19. Particle Image Velocimetry (PIV) experiments were conducted at attack angles $\alpha = 6, 10$ and $\alpha = 16$ deg at Reynolds numbers $Re = 1 \times 10^4$, 3.5×10^4 and $Re = 10^5$ which were based on the wing chord C . The free stream velocities were 1.1m/s,

3.9 m/s and 11.3 m/s for the corresponding Reynolds numbers, respectively. The pressure measurements were conducted at the same angle of attacks for $Re = 3.5 \times 10^4, 5 \times 10^4, 7.5 \times 10^4$ and $Re = 10^5$. Due to high uncertainty values, the pressure measurements were not conducted at $Re = 10^4$. Figure 3-20 presents the overview of the wing model including laser sheet orientations for PIV and flow visualization experiments and the pressure measurement plane.

The chord C of the all four wings were equal and 135 mm with thickness to chord ratio $t/C = 0.06$. The leading edges of the wings were beveled on the windward side at an angle of 45 deg. The top part of the Figure 3-18 illustrates the pressure side, which was same for all planforms, with a sketch of geometric details of bleed holes and their tabulated values. The suction side sketch for three bleed configurations and corresponding representative 3-D sketches are presented at the bottom part. The Base wing had no bleed holes and was not illustrated in the figure. The global coordinate system (x, y) was used to show how planforms were located in free stream and the local coordinate system (x', y') was designated to explain bleed hole orientations. The location of the bleed holes on pressure side of planform was kept same for all three configurations. The holes were rounded rectangle in shape, parallel to leading edge on axis y' . The distance to leading edge, d , the length of the holes, l , the distance between holes, s , and the width of the holes, r . The planforms with different bleeding configurations were named as Back (B), Edge (E) and Back & Edge (BE) referring to direction of the bleed air. To better visualize the direction of bleed holes, angles Φ and θ were defined with respect to local coordinate system and tabulated. Φ represents the angle between bleed air direction and x' , and θ represents the angle between bleed air direction and y' axis. θ and Φ angle values (θ, Φ) for B, E and BE planforms were (18,90), (90,45), (18,45) respectively. The value of the angle θ was determined such that it was higher than the maximum angle of attack value in this study which is 16 deg. The aim of this angle was to increase possible effectiveness of hole as the angle of attack increases. The value of the angle Φ is defined such that the air leaves leading edge tangentially, hence same with bevel

angle. Pressure tabs were located at chordwise distance of $x/C = 0.5$. The number of pressure holes was different on each planform due to the geometric constraints associated with the bleeding holes. The Base, B, E and BE wings had 20, 16, 14 and 14 pressure tabs, respectively. The maximum blockage ratio occurred at the highest attack angle of $\alpha = 16$ deg and was 1%.

3.3.3 Flexion Ratio Experiments

In this study, it is aimed to control the flow structure and particularly to delay stall on a non-slender delta wing by passive control, i.e. material modification inspired by nature. A recent investigation [98] shows that the natural fliers and swimmers obey the same bending rules, same flexion ratio, being independent from the scale of the organism or the fluid medium. As previously presented in Chapter 2, Figure 2-17 demonstrates the flexion ratio and flexion angle concept, as well as their value for a broad range of swimmers and fliers. Flexion ratios and flexion angles are independent from the scale of organism, the fluid medium and the taxonomic group [98]. Previous studies show that flexibility enhances the flow structures over delta wing planforms via whole body oscillations. Since it is impractical to design a flexible planform with whole body oscillations, an alternative approach for using flexibility; using the bending rules in nature is implemented.

Effect of flexion ratio application on nonslender delta wings were studied quantitatively via Particle Image Velocimetry (PIV) experiments at attack angles $\alpha = 6, 8, 10, 12, 14, 18, 24$ and $\alpha = 30$ deg at Reynolds numbers $Re = 1 \times 10^4, 2 \times 10^4, 3.5 \times 10^4$ and $Re = 10^5$ which were based on the wing chord C . The free stream velocities were 1.1 m/s, 2.3 m/s, 3.9 and 11.3 m/s for the corresponding Reynolds numbers, respectively. Figure 3-21 and 3-22 present the geometric details of the planforms along with the examples of manufactured wings from stainless steel, and the experimental matrix, respectively.

Five delta wing models of 45 deg sweep, made of stainless steel, were manufactured. The base wing was manufactured from 2 mm stainless steel with no bevel on the leading edges by water jet cutting. The chord C of the all four wings were equal and 135 mm with thickness to chord ratio $t/C = 0.015$ at rigid part. The flexion ratio is defined as a/S where, a , represents the rigid length of the planform at designated measurement plane and S represents the half-span length for the same measurement plane. Although nature optimized the flexion ratio, a/S , to 0.7, in order to better understand the flow physics, wings with flexion ratio $a/S = 0.7, 0.5$ and 0.3 was manufactured. The wings were manufactured such that 45 deg sweep wing planforms of $50 \mu m$ and $100 \mu m$ of stainless steel were produced and mounted on 2 mm rigid wings with sweep angles to 12 ,17 ,25 with a metal-to-metal tape. However, initial PIV experiments demonstrated that wing planforms with flexible parts made of $100 \mu m$ didn't respond to free stream flow and hence discarded from experiments. Figure 3-23 presents the plan view of the wing model and measurement plane. The maximum blockage ratio occurred at the highest attack angle of $\alpha = 30$ deg and was 1.2%.

3.4 Uncertainty Estimates

Experimental uncertainties are inevitable companions of experimental data and must be considered from beginning to end of the experimental work. The uncertainty may be due to the physical phenomenon to be measured and due to the experimental system.

The uncertainties related to pressure coefficient measurements which were based on pressure measurements were calculated via method error propagation of Kline and McClinton [106].

$$\omega_R = \left[\left(\omega_{x_1} \frac{\partial R}{\partial x_1} \right)^2 + \left(\omega_{x_2} \frac{\partial R}{\partial x_2} \right)^2 + \dots + \left(\omega_{x_n} \frac{\partial R}{\partial x_n} \right)^2 \right]^{1/2} \quad (3.7)$$

Equation 3.7 calculates the resultant uncertainty depending on the uncertainties of each independent variables, ω_{x_i} . Since all the pressure measurements were done with same pressure scanner, all ω_{x_i} values are same and called ω_p . The physical value of the pressure scanner measurement accuracy was 0.05 % FS. Relative uncertainty of each result can be calculated via Equation 3.8.

$$\frac{\omega_R}{R} = u_R \quad (3.8)$$

Recall that the pressure coefficient was calculated via 3.4.

$$C_p = \frac{p - p_\infty}{\frac{1}{2} \rho U_\infty^2} = \frac{p - p_\infty}{p_{dyn}} = \frac{\Delta P}{p_{dyn}}$$

Applying the afore mentioned method would lead to

$$\omega_{C_p} = \left[\left(\omega_p \frac{\partial C_p}{\partial \Delta P} \right)^2 + \left(\omega_p \frac{\partial C_p}{\partial p_{dyn}} \right)^2 \right]^{1/2} \quad (3.9)$$

The differentiation results in :

$$\omega_{C_p} = \left[\left(\frac{\omega_p}{p_{dyn}} \right)^2 + \left(\frac{\omega_p \Delta P}{p_{dyn}^2} \right)^2 \right]^{1/2} \quad (3.9)$$

The calculated results are tabulated in Table 1. The relative uncertainty values for the pressure coefficient $-C_p$ at the peak values were estimated as 0.3 and 3% at two different Reynolds number.

Table 1 Uncertainty values for the pressure measurements for passive bleed experiments for all planforms at the maximum and the minimum Reynolds numbers for attack angles $\alpha = 6, 10$ and 16 deg.

Uncertainty (%)		Base	B	E	BE
$\alpha=6$ deg	Re=35000	2.4	2.54	2.95	2.7
	Re=100000	0.26	0.28	0.35	0.28
$\alpha=10$ deg	Re=35000	2.2	2.2	2.5	2.4
	Re=100000	0.25	0.26	0.3	0.26
$\alpha=16$ deg	Re=35000	2.5	2.3	2.8	2.5
	Re=100000	0.29	0.26	0.34	0.3

The uncertainty values for PIV measurements are calculated via commercial software TSI Insight4G and tabulated for the conducted experiments. The uncertainty results for the passive bleed experiments and flexion ratio experiments are tabulated in Table 2 and Table 3. For the whole span of experiments the maximum uncertainty values in measured velocity values are 10%.

Table 2 Uncertainty values for the PIV measurements for passive bleed experiments for all planforms at the maximum and minimum Reynolds numbers for attack angles $\alpha = 6$ and 16 deg.

Uncertainty (%)		Base	B	E	BE
$\alpha=6$ deg	Re=10000 (1.13m/s)	11.5	7.1	7.1	9.7
	Re=100000 (11.3 m/s)	8.8	8.8	19.7	8.8
$\alpha=16$ deg	Re=10000 (1.13 m/s)	8.8	7.9	6.6	8.8
	Re=100000 (11.3 m/s)	9.3	7.9	6.2	8.4

Table 3 Uncertainty values for the PIV measurements for flexion ratio concept experiments for base planform and planform $a/S = 0.7$ at the maximum and minimum Reynolds numbers for attack angles $\alpha = 12$ and 30 deg.

Uncertainty (%)		Base	$a/S = 0.7$
$\alpha=12$ deg	Re=10000 (1.13m/s)	8.8	6.2
$\alpha=30$ deg	Re=10000 (1.13 m/s)	8.8	7.9
	Re=100000 (11.3 m/s)	6.2	6.2

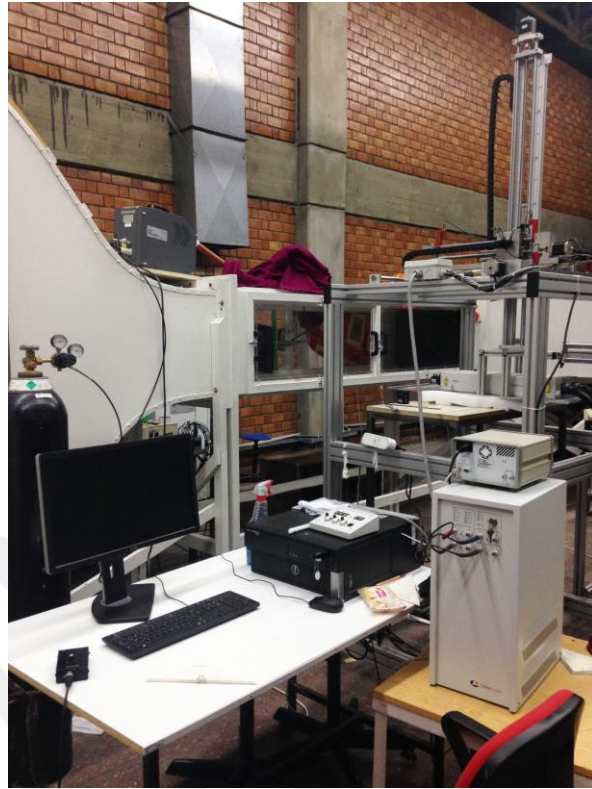


Figure 3-1 View from wind tunnel facility (top) and test section (bottom).

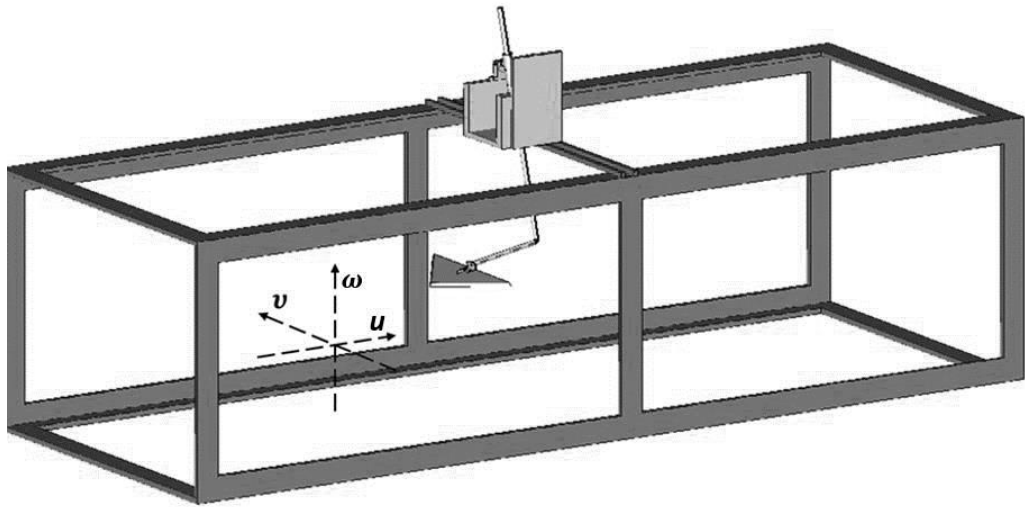


Figure 3-2 Wing model, mount and test section assembly.

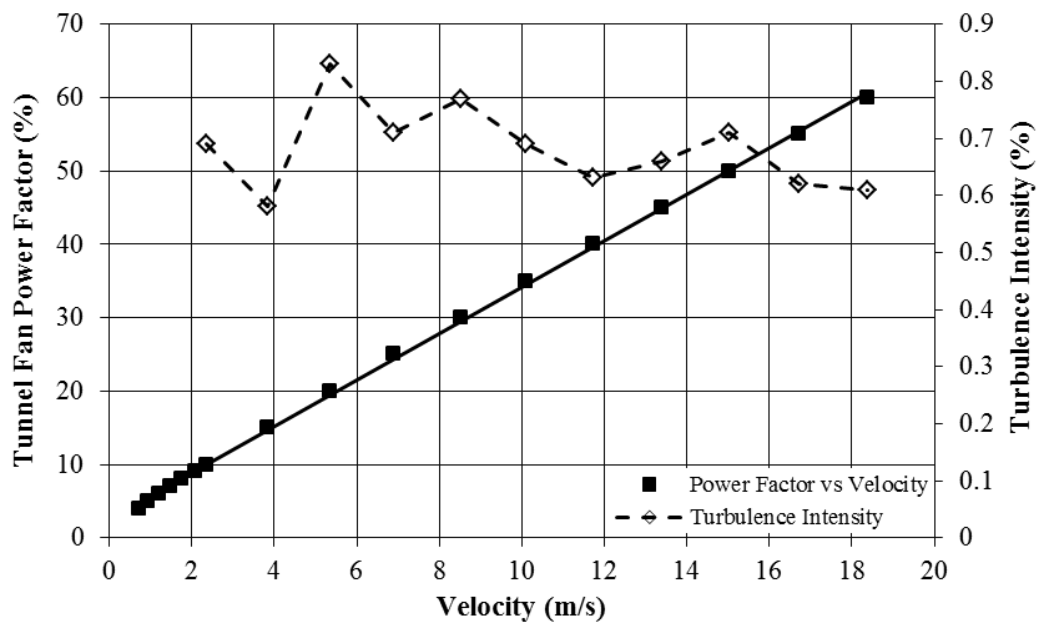


Figure 3-3 Wind tunnel calibration graph.

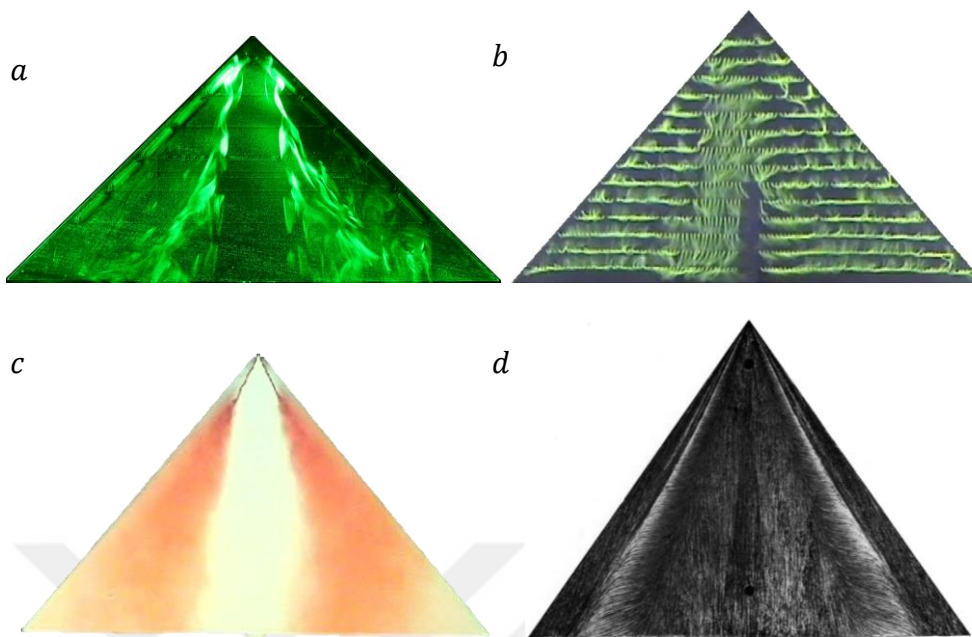


Figure 3-4 Examples of flow visualization results a) laser illuminated smoke visualization, b) tuft visualization[6], c)dye visualization [6], d) surface oil visualization[107].

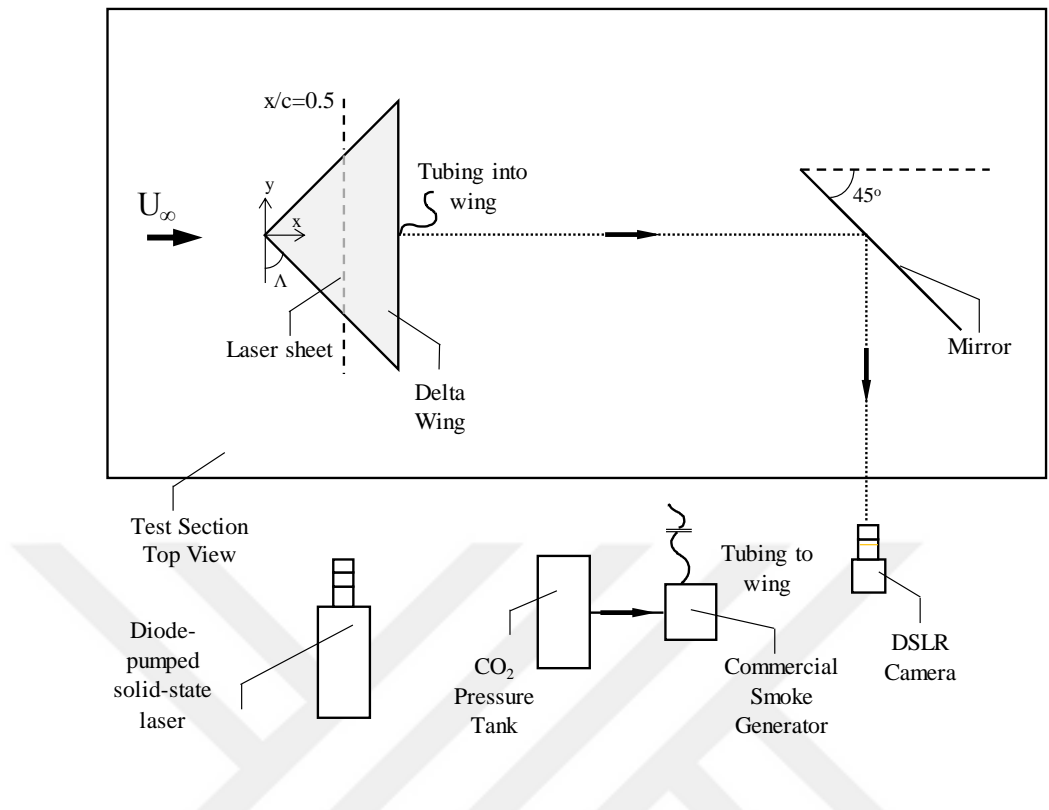


Figure 3-5 Schematics of cross flow laser-illuminated smoke visualization experiment set-up.

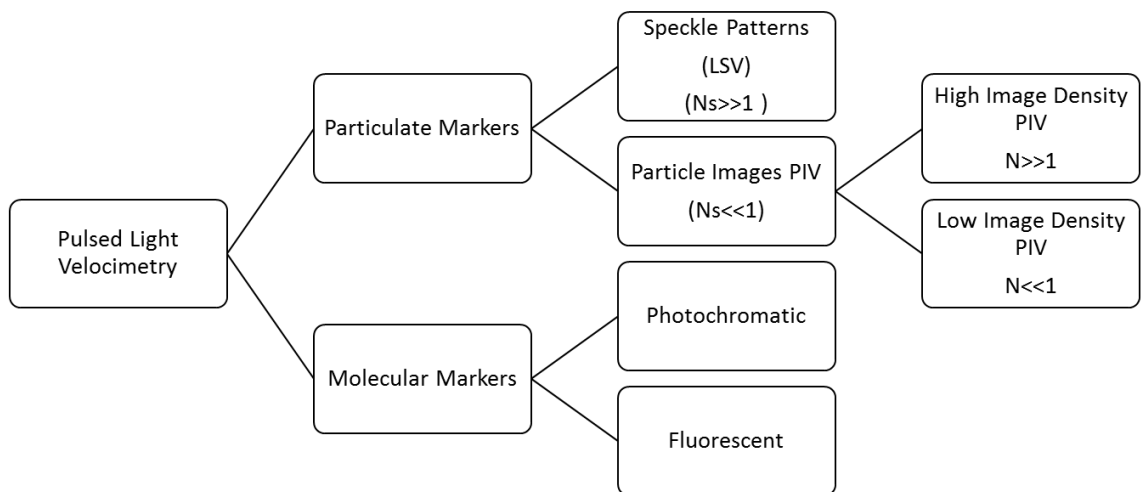


Figure 3-6 Classes of pulsed-light velocimetry.

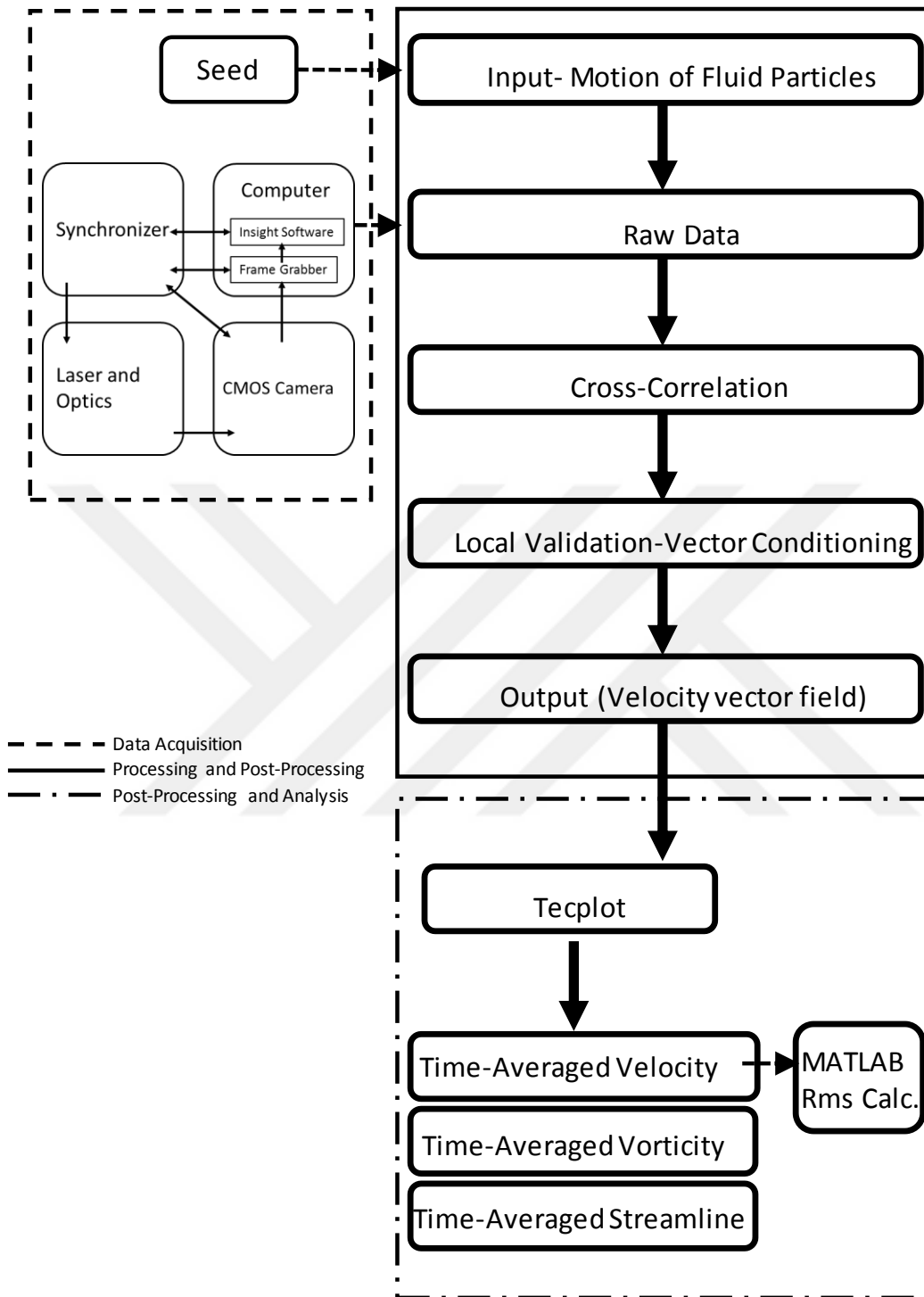


Figure 3-7 Flow chart of PIV experiment : acquisition, processing, post-processing and analysis.

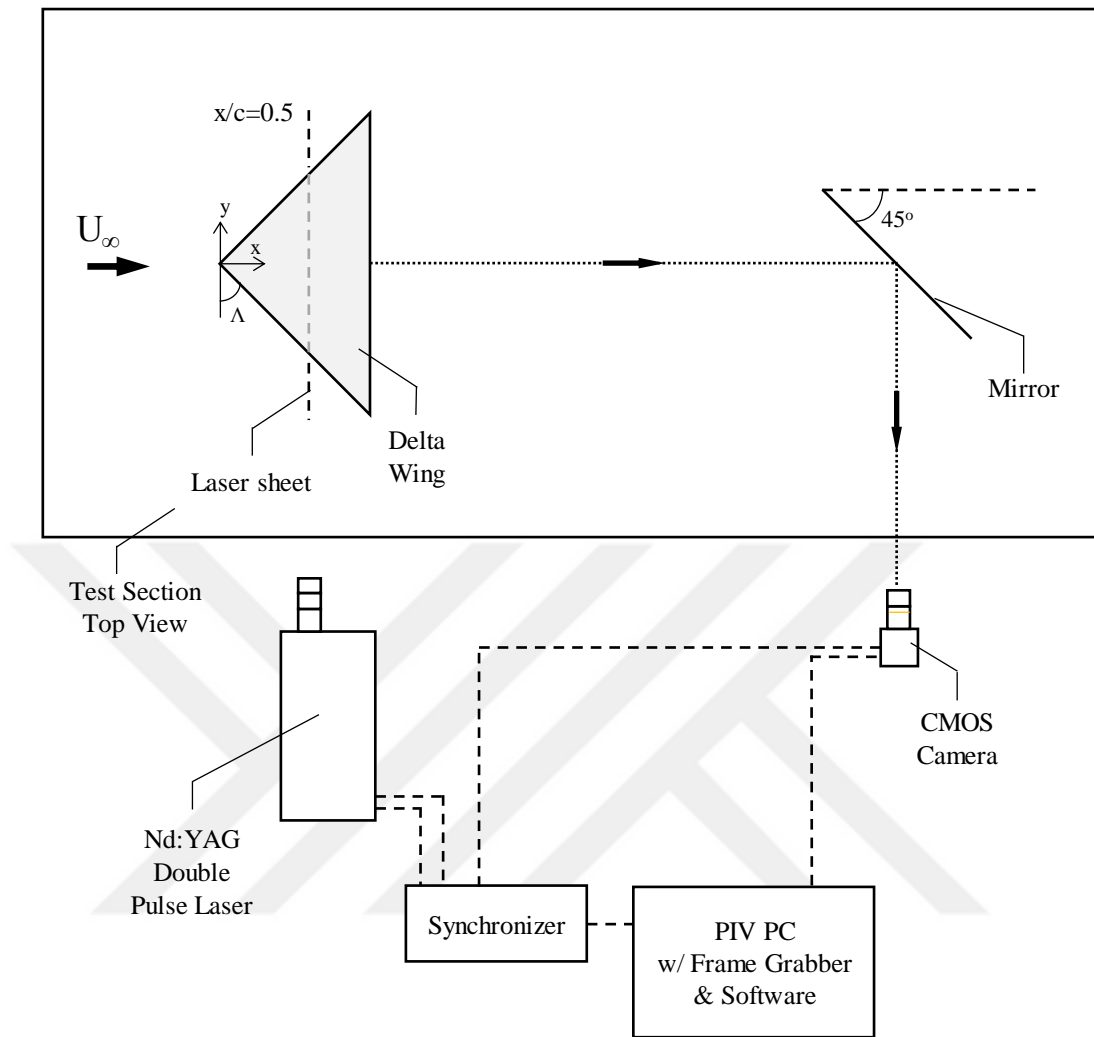


Figure 3-8 Schematic representation of the cross flow PIV experiment set-up.

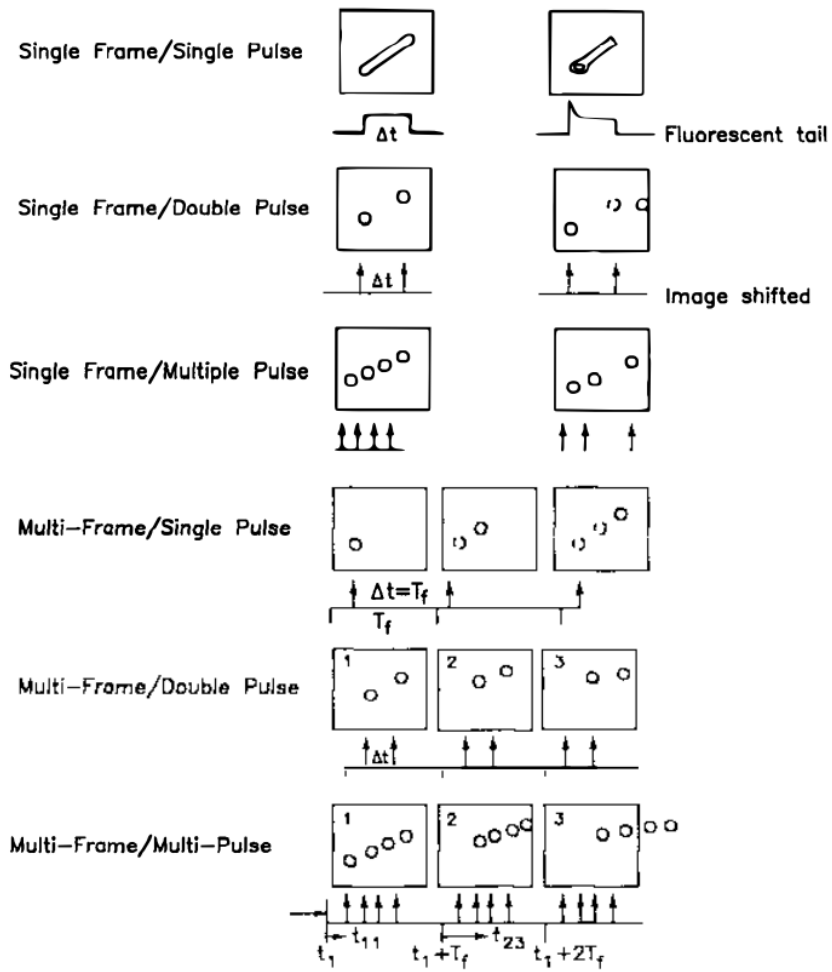


Figure 3-9 Possible methods for pulse-coding and framing methods in Particle Image Velocimetry [103].

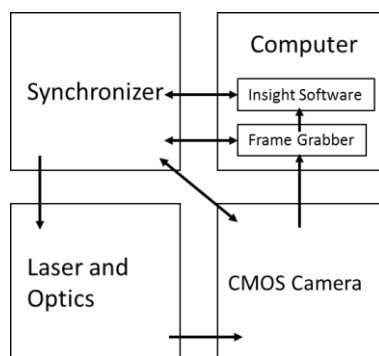


Figure 3-10 Data transfer routes of a 2D PIV system.

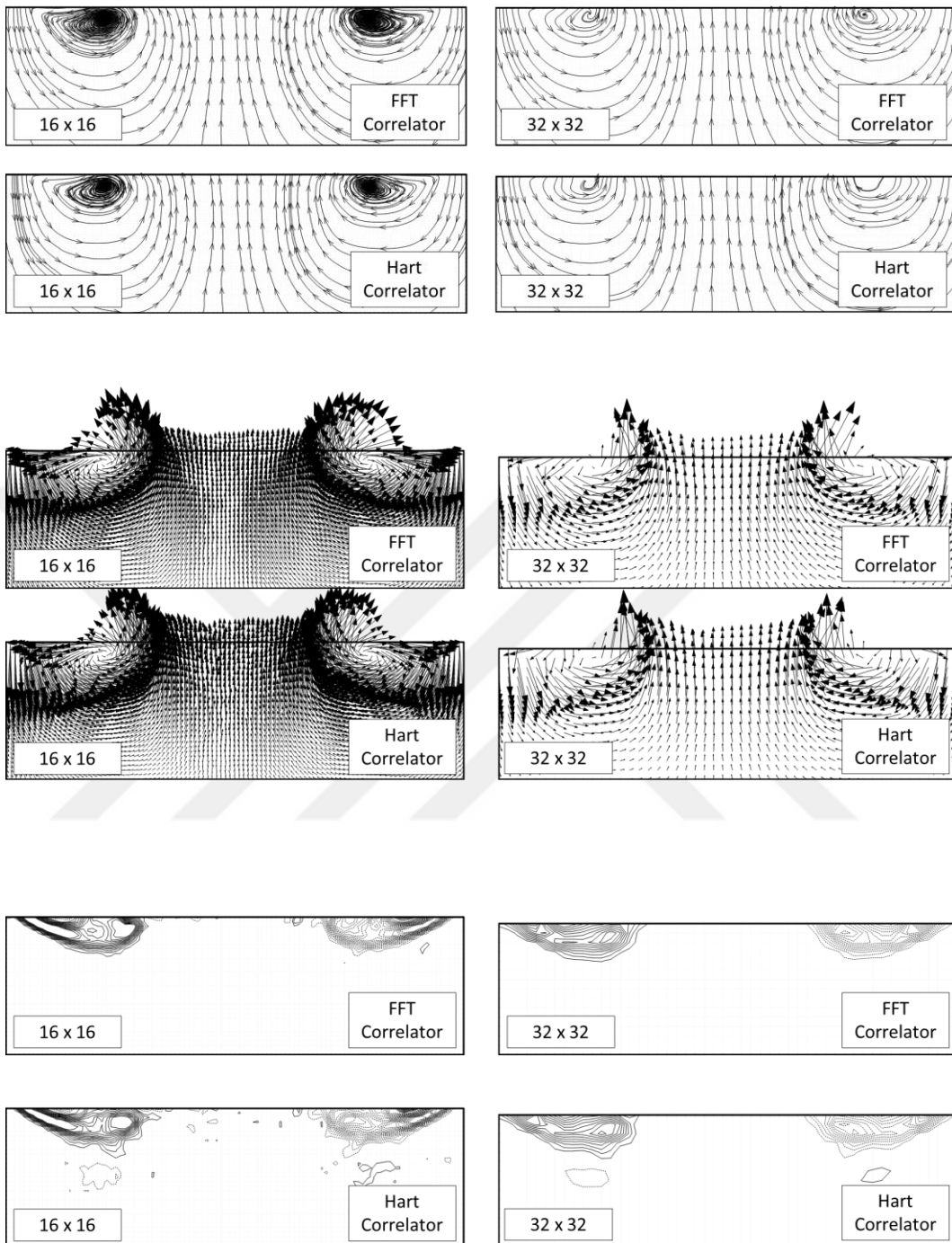


Figure 3-11 Comparison of FFT correlator with Hart correlator on results at 16x16 and 32x32 interrogation windows via streamlines, velocity vectors and non-dimensional axial vorticity contours from top to bottom respectively.

Vector data from tecplot

$$v_{rms}(x, y) = \sqrt{\left\{ \frac{1}{N} \sum_{n=1}^N [v_n(x, y) - \langle v(x, y) \rangle]^2 \right\}}$$

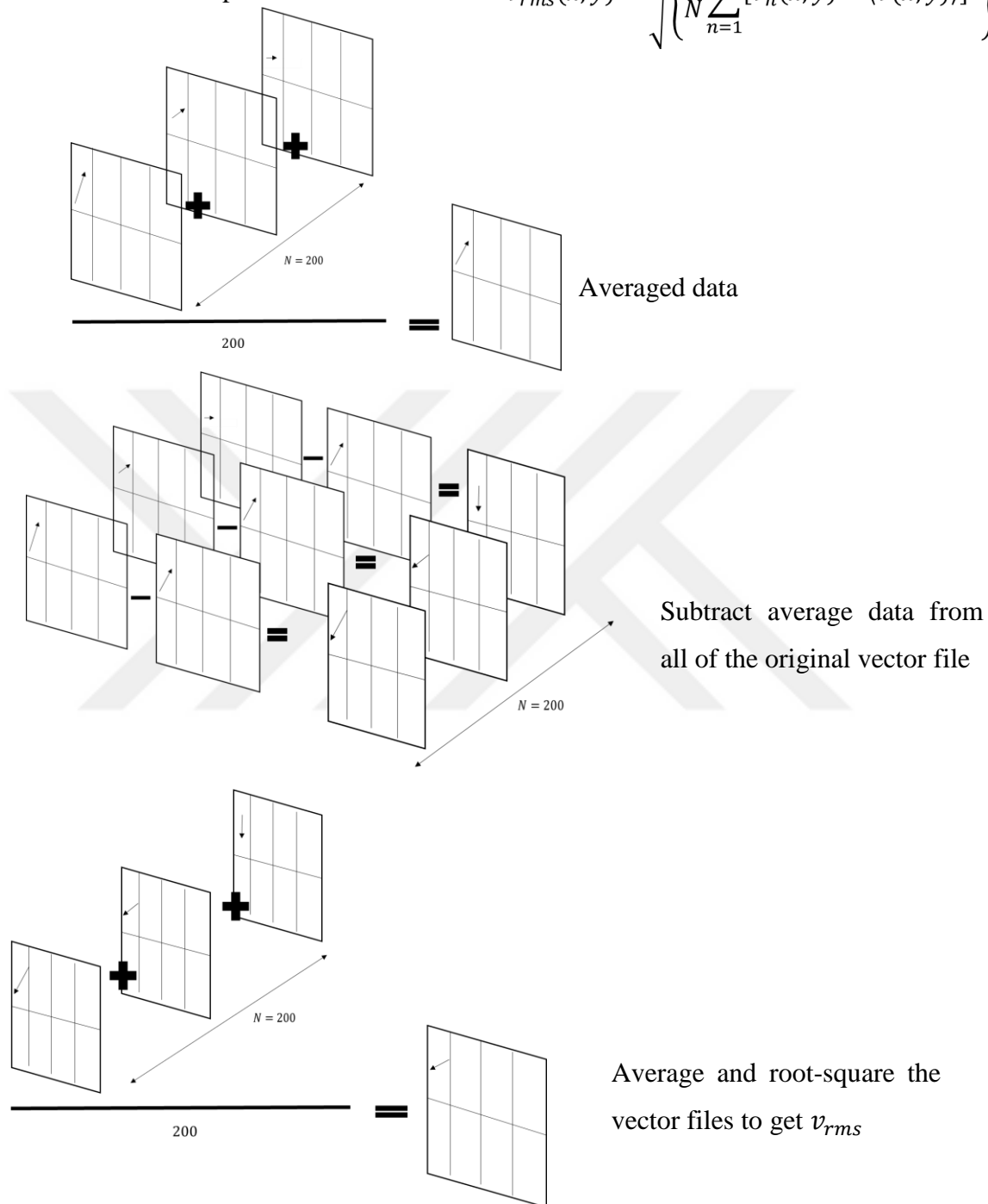
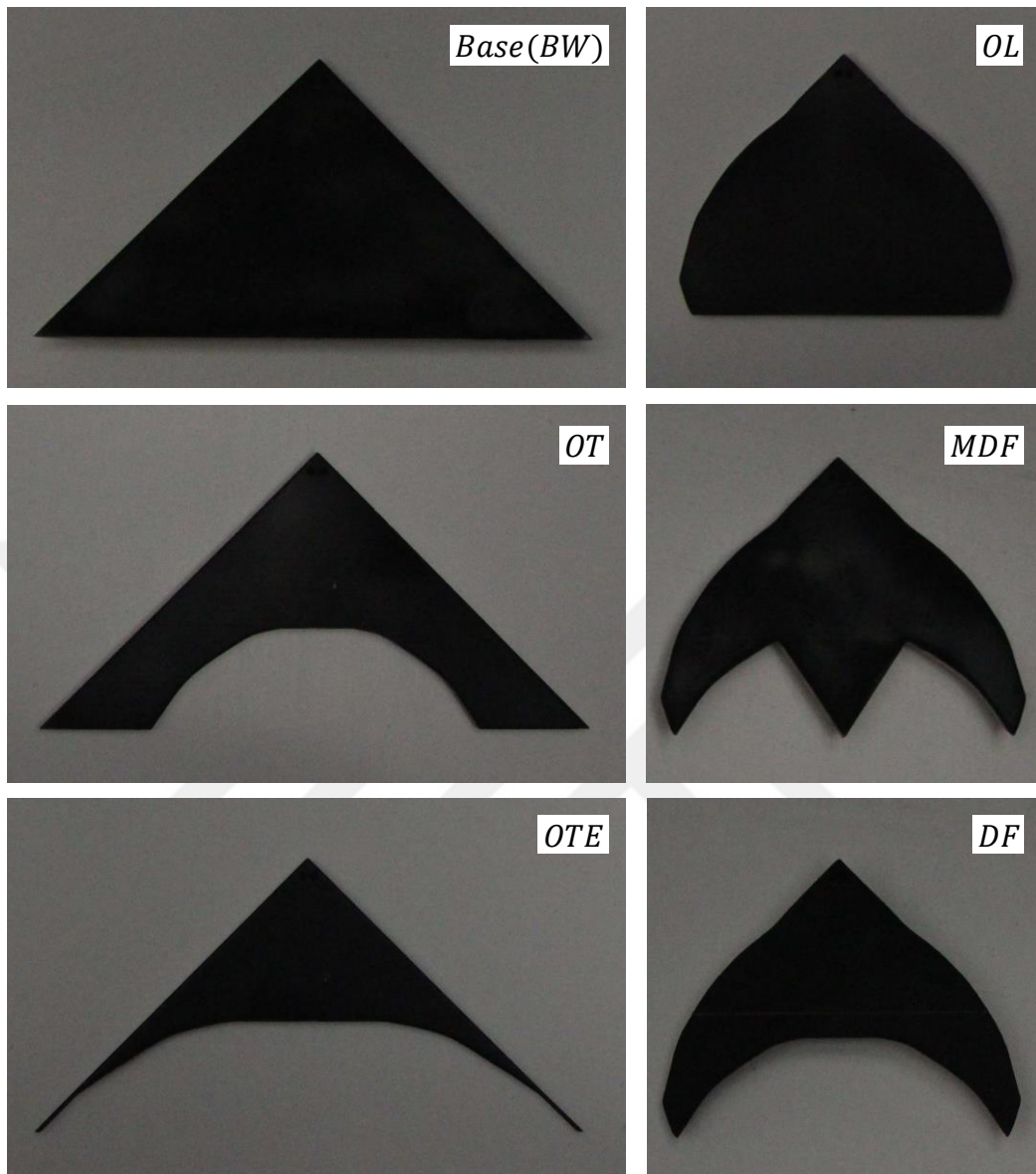


Figure 3-12 Schematics of how to calculate v_{rms} data from original tecplot vector file.



- BW : Base Wing
- OL : Only Leading Edge Modification
- OT : Only Trailing Edge Modification
- DF : Dolphin Fluke
- MDF : Modified Dolphin Fluke
- OTE : Only Trailing Edge Extended Modification

Figure 3-13 Manufactured wings for bio-inspired edge-modification experiments.

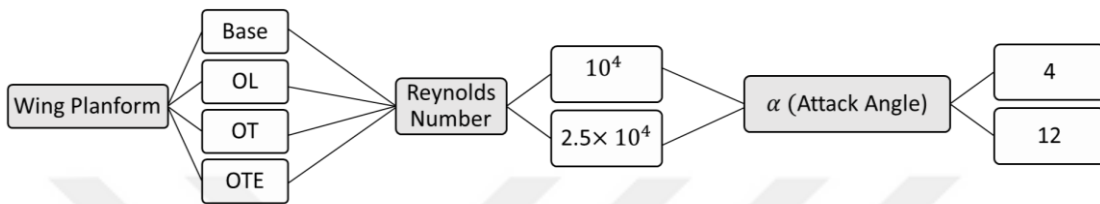
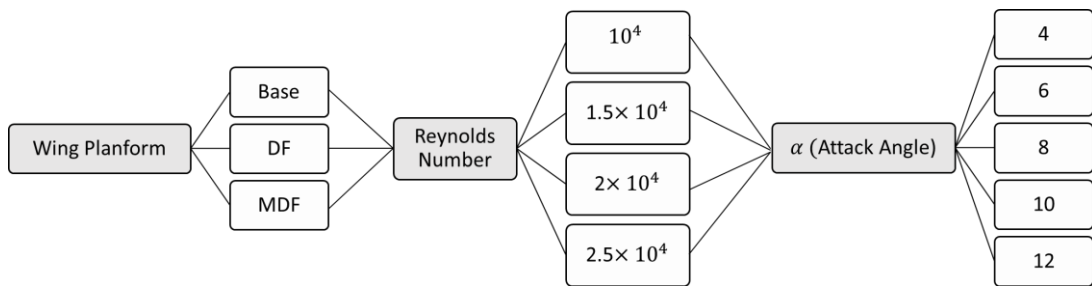


Figure 3-14 Experiment matrices for edge modification experiments Part-I (up) and Part II (bottom).

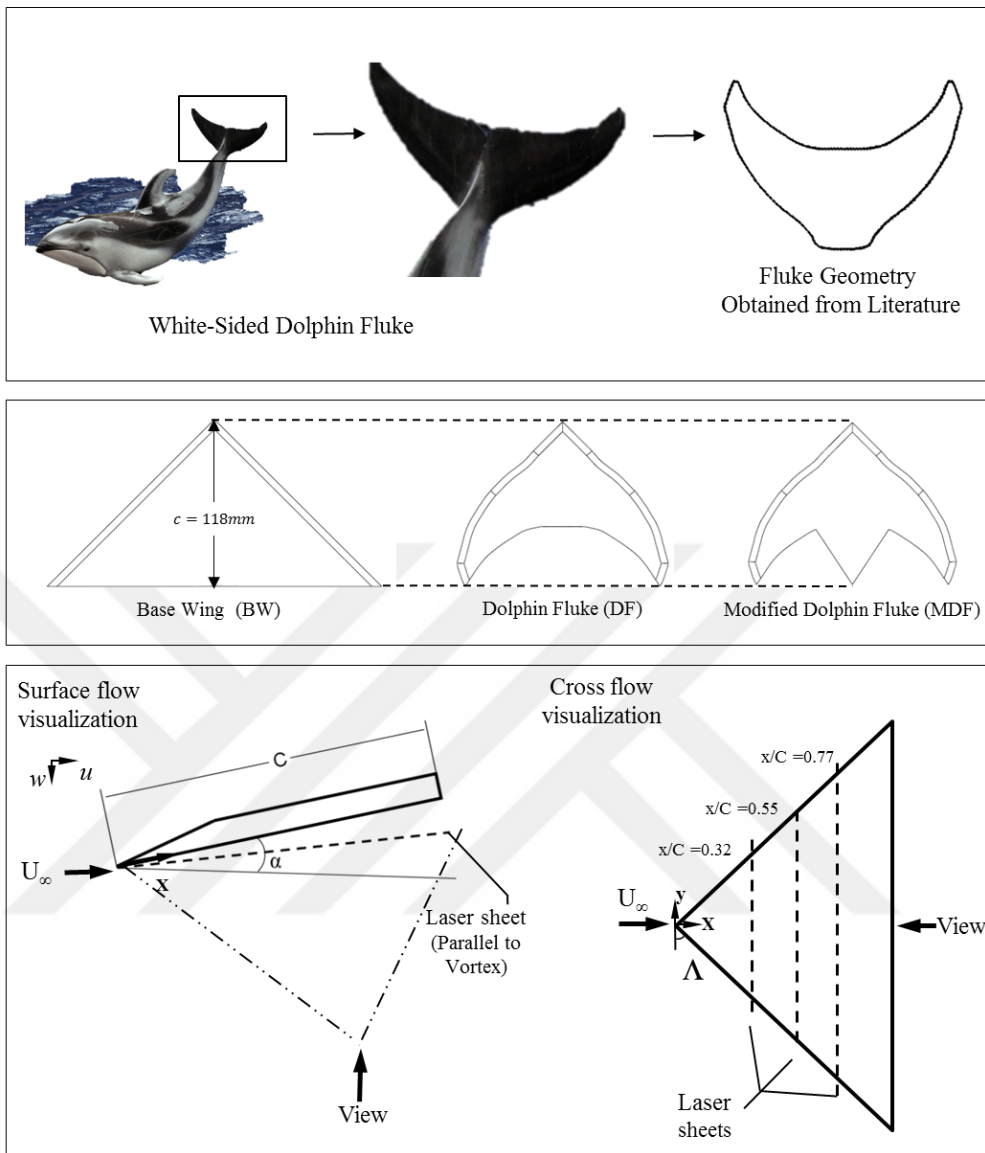


Figure 3-15 Overview of the wing models and measurement planes for bio-inspired edge modification experiments for Part I.

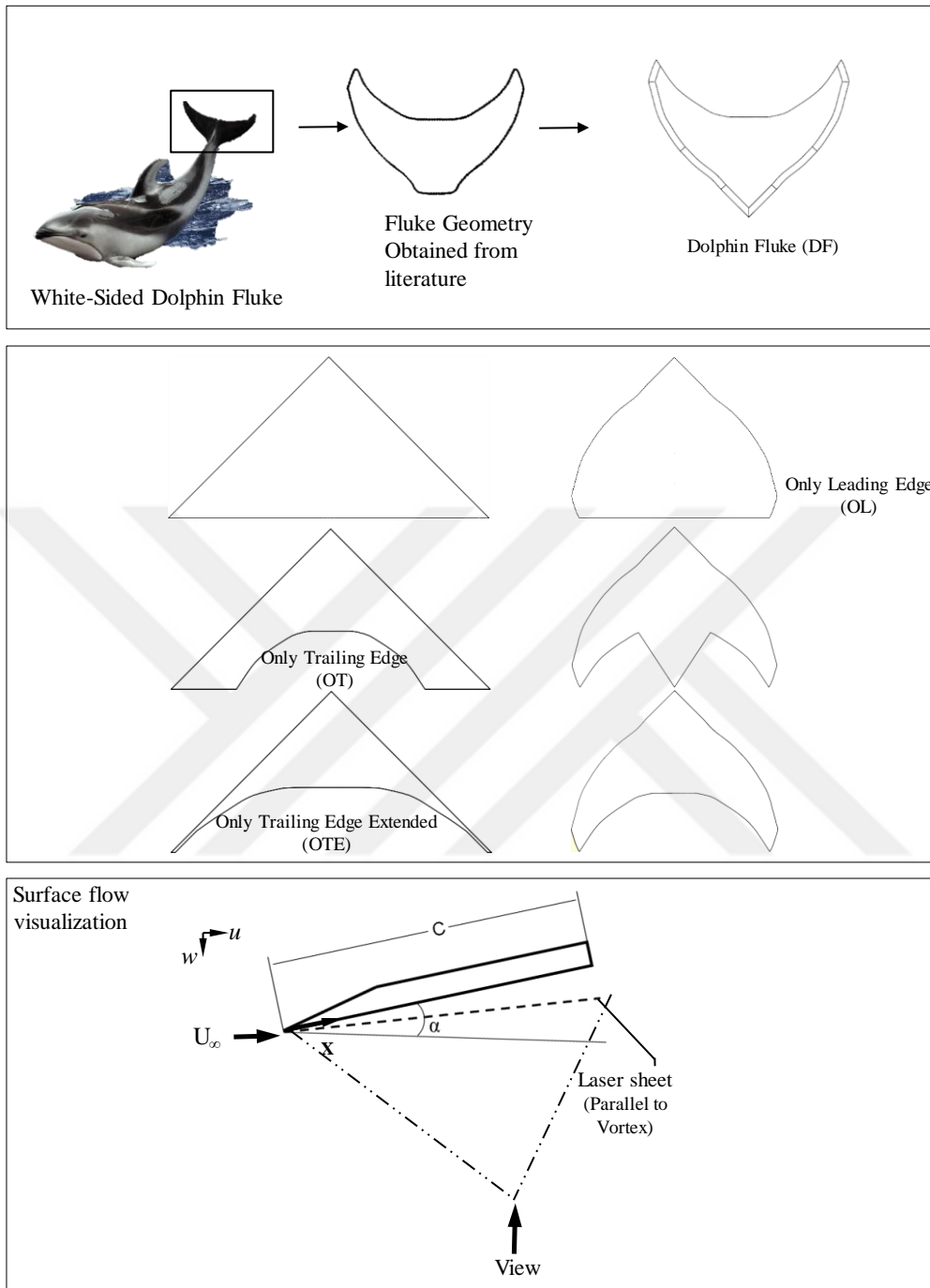


Figure 3-16 Overview of the wing models and measurement planes for additional bio-inspired edge modification experiments for Part II.

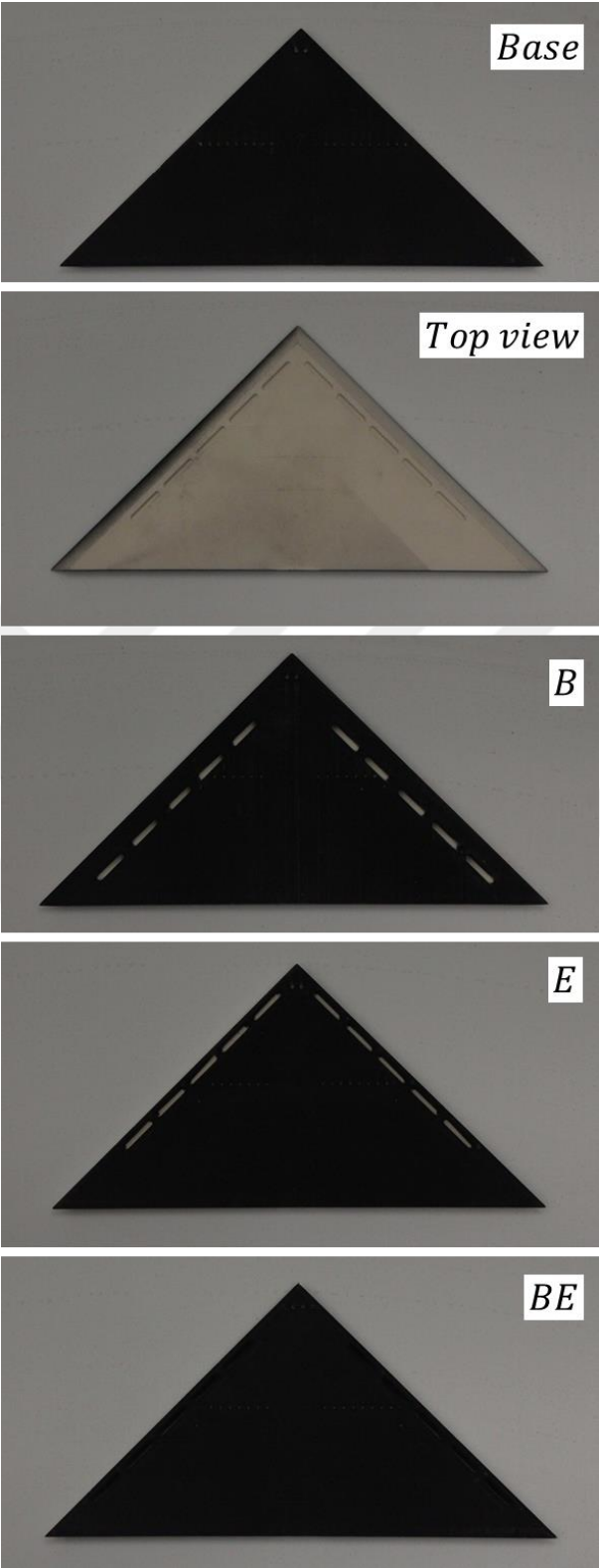


Figure 3-17 Manufactured wings for passive bleed experiments.

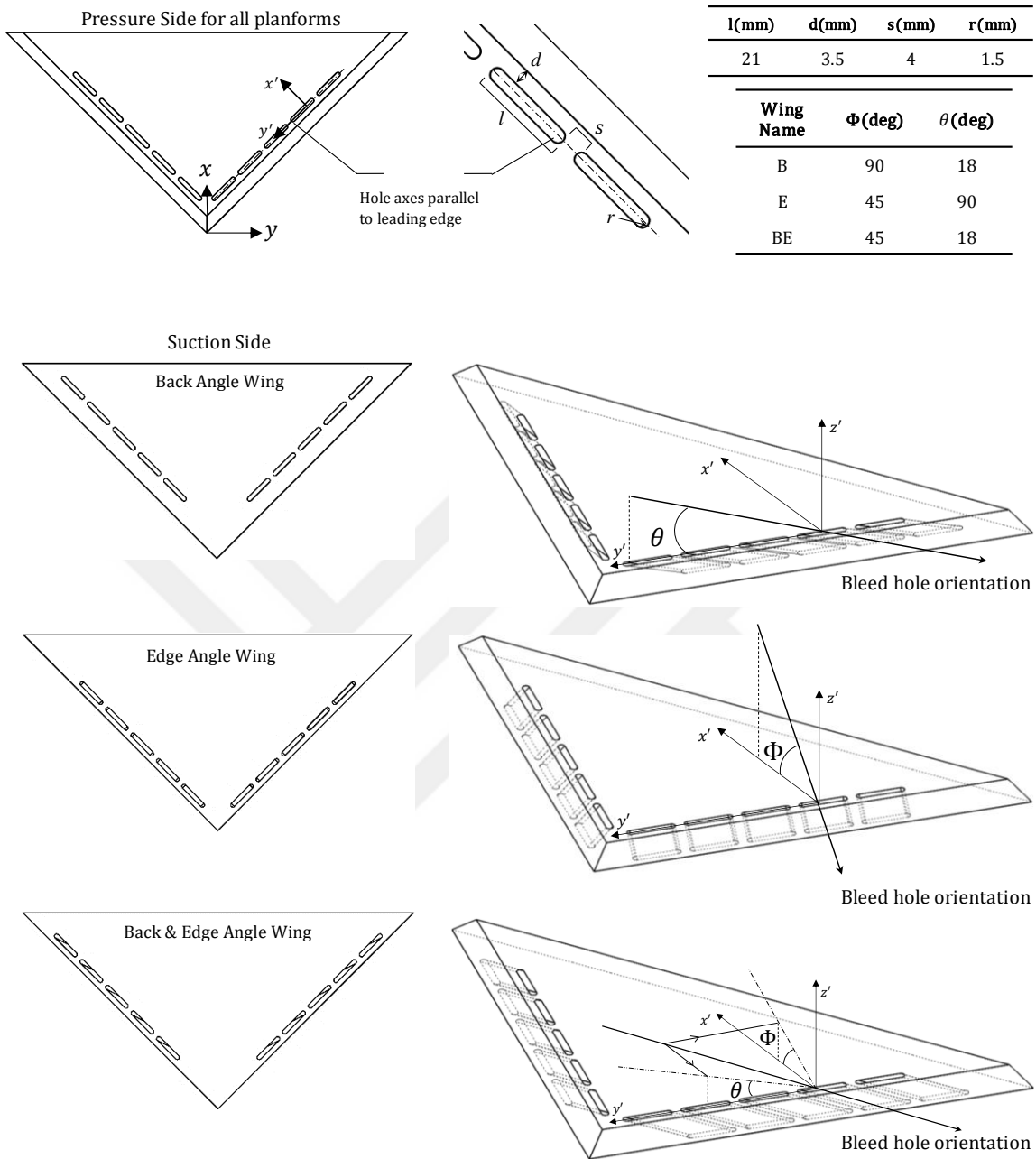


Figure 3-18 Details of bleeding configurations of B, E and BE planforms.

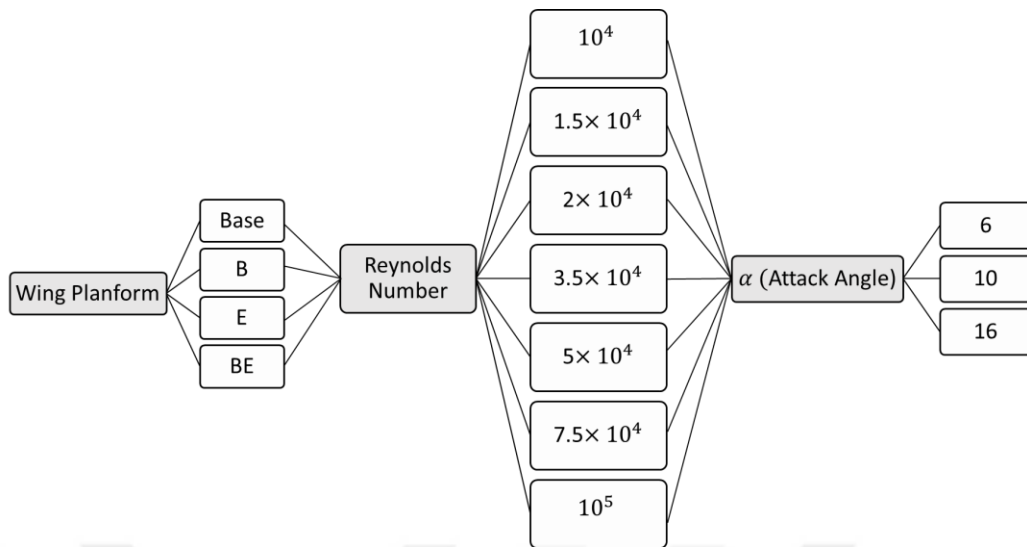


Figure 3-19 Experiment matrix for passive bleed experiments.

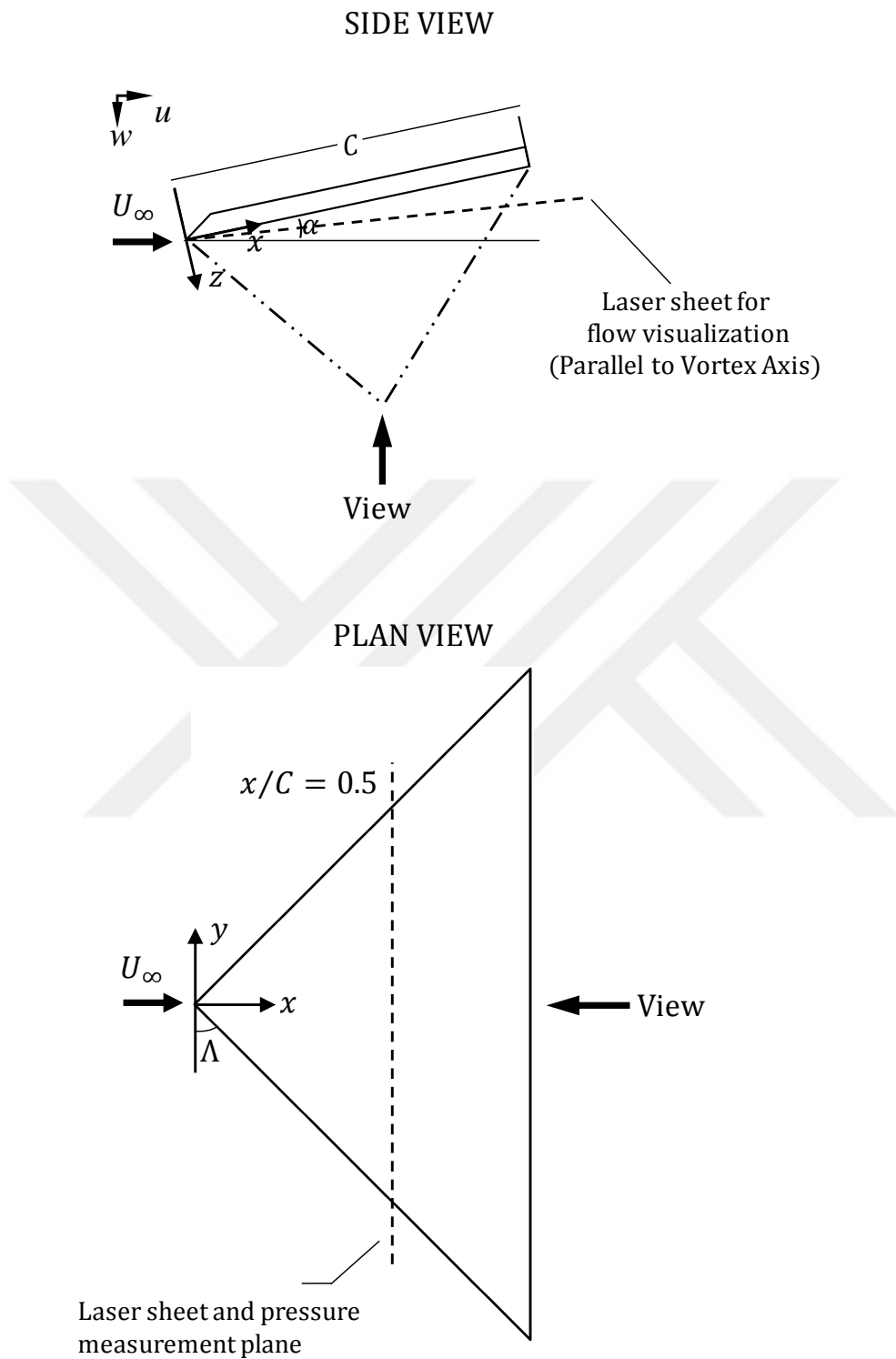


Figure 3-20 Overview of the experimental set-up and with delta wing and laser sheet locations for passive bleed experiments.

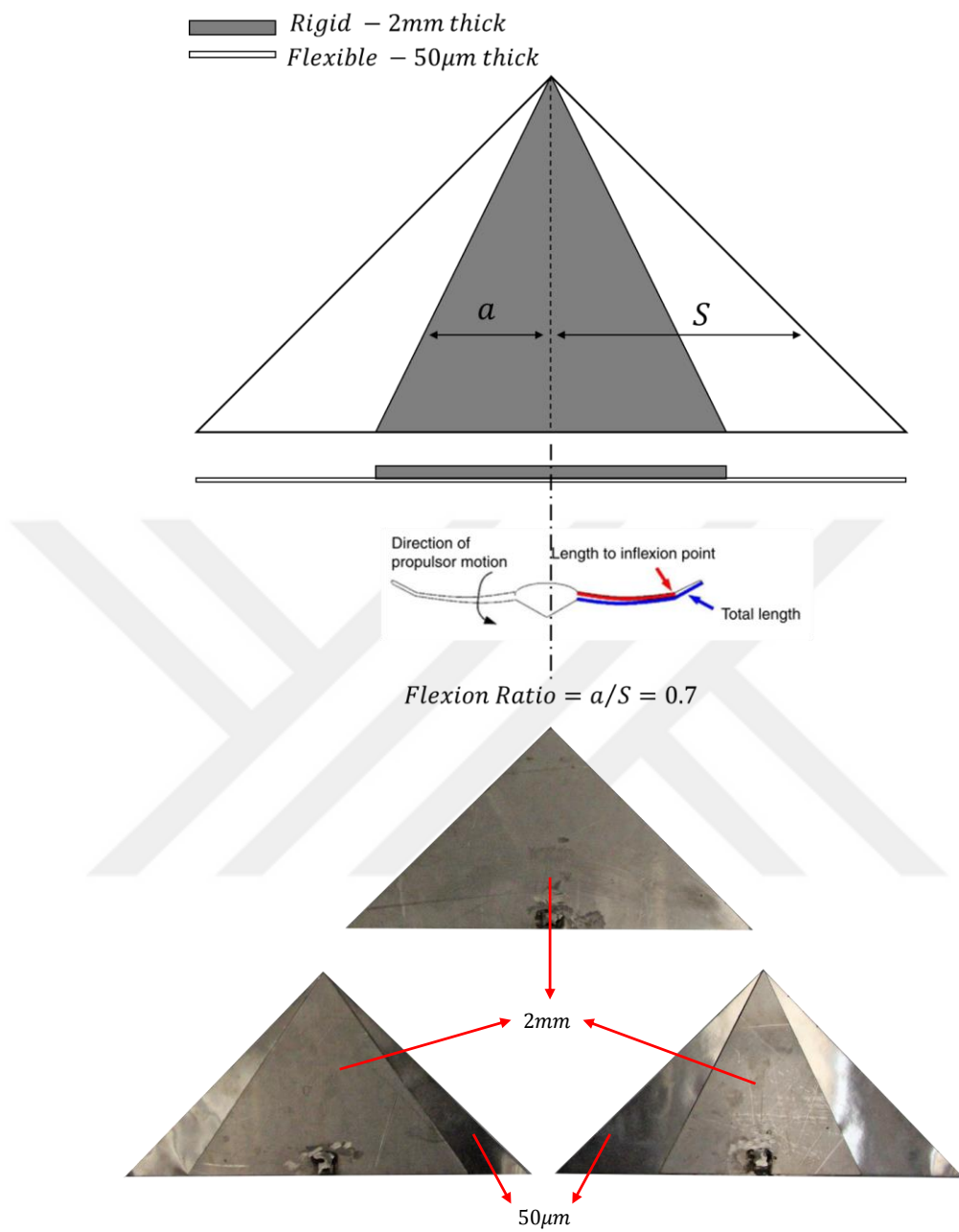


Figure 3-21 Geometric details of flexion experiment wings with examples of manufactured

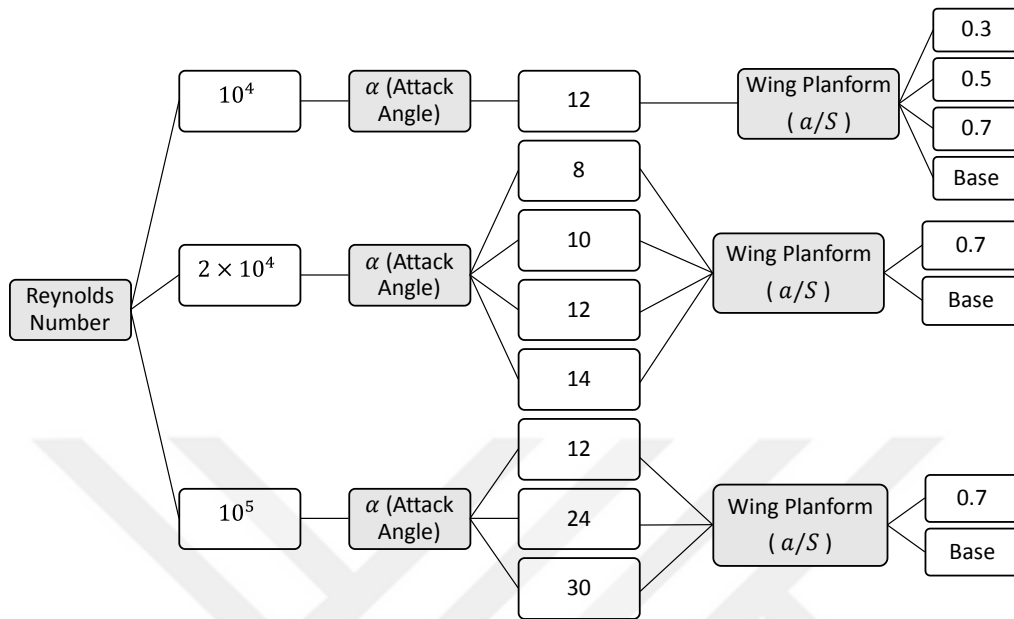


Figure 3-22 Experimental matrix for flexion ratio concept experiments.

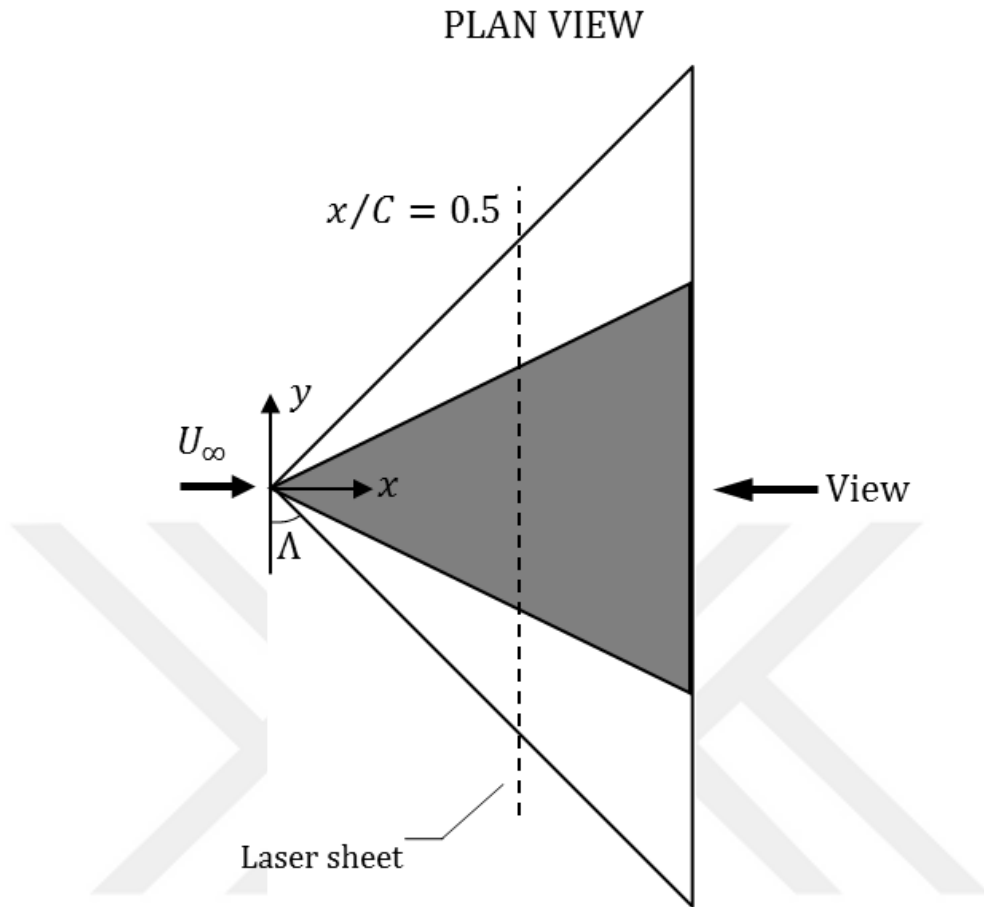


Figure 3-23 Overview of the planform with laser sheet orientations for cross flow PIV experiments.



CHAPTER 4

EFFECT OF EDGE MODIFICATIONS ON FLOW STRUCTURE OF A NONSLENDER DELTA WING -PART I

The present chapter investigates the sole effect of bio-inspired geometry modification on flow structure and stall characteristic of a 45° swept delta wing using laser illuminated smoke visualization technique. The bio-inspired geometry was derived from fluke geometries due to apparent physical similarity. The fluke geometry was obtained from the literature, which was a white-sided female dolphin of sweep angle 47.7 [107]. The fore body of the fluke was adapted to have 45° of sweep. The adaptation point was chosen such that the shoulder on the geometry was kept without any change. The chord C based on Reynolds number was varied within the range of $10^4 < Re < 2.5 \times 10^4$ and the attack angles were $\alpha = 4^\circ, 6^\circ, 8^\circ, 10^\circ$ and 12° to cover a broad range of operation with different flow characteristics including leading edge vortices, vortex breakdown, and three-dimensional separation from the wing surface. The effect of leading edge and trailing edge modification is also studied separately and presented in next chapter.

4.1 Results and Discussions

Surface flow visualizations for three wing planforms, base wing (BW), dolphin fluke (DF), and modified dolphin fluke (MDF), at attack angle $\alpha = 4^\circ$ and Reynolds numbers $Re = 10^4, 1.5 \times 10^4, 2 \times 10^4, 2.5 \times 10^4$ are demonstrated in Figure 4-1. The first, the second, and the third column represent the results of base wing (BW), modified dolphin fluke (MDF), and dolphin fluke (DF), respectively. Each row represents the corresponding Reynolds numbers in ascending order, top to bottom, from Reynolds number $Re = 10^4$ to $Re = 2.5 \times 10^4$. Considering the

surface flow visualization for the base wing (BW) at $Re = 10^4$, it is apparent that symmetrical single leading edge vortex structure without any indication of breakdown is dominating the flow over the planform. In addition, a very weak in nature, small filaments are also apparent on the outboard sides of these single vortices, which might be an early indication of second primary vortex. For the modified dolphin fluke (MDF) and dolphin fluke (DF) planforms shown in the second and the third column of the first row images in Figure 4-1, these filaments are more apparent and believed to be indicating a stronger second primary vortex. Increasing Reynolds number to $Re = 1.5 \times 10^4$, as shown in the second row images in Figure 4-1, leading edge vortices on all three planforms move slightly outboard. For the base wing planform, a dual vortex structure is observed without clear indication of breakdown on the planform. However, considering the surface smoke visualizations of DF and MDF planforms at the corresponding Reynolds number, distinctive flow patterns are seen. Although dual vortex structures are still dominant near apex region for both planforms, outboard vortex transforms into a very stable, small-scale whorl pattern as it moves towards the mid-chord region. This structure is similar to whorl patterns observed on 45 degree sweep delta wings in [1]. The inboard vortex remains stable until it reaches to the trailing edge where it suffers from breakdown. Slight difference between the flow patterns of DF planform and MDF planform is also witnessed. The whorl pattern on MDF planform is not as apparent as DF planform. At Reynolds number $Re = 2 \times 10^4$ for the base wing (BW) unsteady oscillations on the outboard vortex is observed and dual vortex structure seems to be intertwining along with the movement of vortex breakdown location upstream toward the apex of the wing. The aforementioned whorl pattern observed for fluke planforms at Reynolds number $Re = 1.5 \times 10^4$, seems to be vanishing on MDF planform. The smoke pattern on DF planform is not as coherent as $Re = 1.5 \times 10^4$ and this might be an indication of relatively weaker whorl pattern formation. In addition, it is observed that increasing Reynolds number from $Re = 1.5 \times 10^4$ to $Re = 2 \times 10^4$ does not have any remarkable effect on the location of vortex breakdown for DF and MDF

planforms. Increasing Reynolds number to $Re = 2.5 \times 10^4$ deteriorates the dual vortex structure on BW planform and significantly moves the vortex breakdown location upstream toward the apex of the wing. Considering the flow structures on dolphin fluke planforms at Reynolds number $Re = 2.5 \times 10^4$, dual vortex structure on MDF seems to be similar to the patterns on BW planform. On DF planform the outboard vortex experiences a very early breakdown. In addition, primary vortex experiences early breakdown compared to BW and MDF planforms.

In order to better identify the difference in flow structures between BW planform and DF planform and better understand aforementioned distinctive whorl pattern obtained in dolphin fluke planforms, Figure 4-2 is constructed for attack angle $\alpha = 4^\circ$ and Reynolds number $Re = 1.5 \times 10^4$. Surface flow smoke visualization and cross flows smoke visualizations at three different chordwise distances $x/C = 0.32$, $x/C = 0.55$ and $x/C = 0.77$ are presented at the top and the bottom part of Figure 4-2 for BW and DF planforms, respectively. Dimensionless length scales indicating the spanwise position at various cross flow planes are also added on these figures to clearly identify corresponding location of flow structures on the wing surface. Considering the cross flow patterns along with the surface flow patterns for both planforms, apparent coherence in flow patterns at different measurement planes are witnessed. For BW planform, strong dual vortex structure entirely remains on the planform without any dispersion of smoke whereas for DF planform, this structure is only evident at $x/C = 0.32$ and not apparent further downstream at other two chordwise distances. At cross flow plane of $x/C = 0.55$, a single vortex core along with a dispersed smoke distribution outboard of this vortex structure is observed. At cross flow plane of $x/C = 0.77$, vortex structure seems to be suffering from breakdown which is clearly supported by the surface flow smoke visualization. Smoke distribution indicates an expanded vortex core without complete dispersion to the flow field.

The rest of the figures are constructed as Figure 4-1 where surface flow visualizations for three wing planforms, base wing (BW), dolphin fluke (DF), and modified dolphin fluke (MDF), are demonstrated for different Reynolds numbers at attack angles $\alpha = 6^\circ, 8^\circ, 10^\circ, 12^\circ$, respectively. The first, the second, and the third column represent the results of base wing (BW), modified dolphin fluke (MDF), and dolphin fluke (DF), respectively. Each row represents the corresponding Reynolds numbers in ascending order, top to bottom, from Reynolds number $Re = 10^4$ to $Re = 2.5 \times 10^4$. Figure 4-3 demonstrates the results for angle of attack $\alpha = 6^\circ$. At $Re = 10^4$ BW planform has a dual vortex structure where inboard vortex remains on the planform without any indication of breakdown. The outboard vortex is rather unstable with a location of breakdown close to the trailing edge of the wing. As Reynolds number increases, breakdown location moves upstream. At Reynolds numbers $Re = 2 \times 10^4$ and $Re = 2.5 \times 10^4$, dual vortex structure turns into a single vortex structure with an indication of breakdown at upstream of the mid-chord. For DF planform, there is a footprint of dual vortex structure at low Reynolds number $Re = 10^4$ which turns out to be an apparent dual vortex structure at $Re = 1.5 \times 10^4$ where the outer vortex breaks down at near mid-chord. Further increase in Reynolds number moves the breakdown location upstream toward the apex of the planform. Considering both the MDF and DF planforms in general, it can be stated that the overall flow structures are quite similar at all Reynolds numbers. The only major difference is detected at $Re = 1.5 \times 10^4$, where the whorl pattern in the outboard vortex seems to have relatively larger spatial extent for MDF planform compared to DF planform.

The whorl patterns observed particularly for dolphin fluke planforms which are shown in Figures 4-1, 4-2 and 4-3, deserve more attention. For the cases where dual vortex structure appears in all planforms, the outboard vortex filament indicates undulations in patterns regardless of the attack angle. This undulation continues and reaches to the trailing edge of the wing on BW planform. However,

on both DF and MDF planforms vortex structure leans toward outboard of the wing and forms a stable whorl pattern. This might be due to the fact that the flow faces with variable sweep as it moves from the apex toward the trailing edge of the wing. Considering the change in nominal sweep angle that fluid experiences (first constant, then decreasing, and after certain point behind our measurement plane of $x/C = 0.77$, starts to increase), it can be argued that the feeding mechanism of the outboard vortex from the separated shear layer deteriorates. In BW planform, this deterioration is not strong enough to create clear whorl structure, however a weak footprint of whorl pattern is also witnessed at $Re = 1.5 \times 10^4$ for attack angle of $\alpha = 6^\circ$ as shown in Figure 4-3.

Figure 4-4 presents the surface smoke visualizations for attack angle $\alpha = 8^\circ$. At $Re = 10^4$ BW planform has a strong leading edge vortex with a breakdown location downstream of the mid chord region. A second vortex is apparent at outboard side of the primary vortex which breakdowns at near apex region. Increase in Reynolds number moves the breakdown location of first primary vortex upstream toward the apex region. Further increase in Reynolds number reaching to $Re = 2.5 \times 10^4$ causes disappearance of coherent vortex structure such that the smoke patterns disperse and cover the whole wing surface. Considering the DF planform, second primary vortex appears at $Re = 1.5 \times 10^4$ with an early breakdown. Increasing Reynolds number to $Re = 2 \times 10^4$ vortex breakdown location shifts upstream and the outboard vortex only appears as filaments with a very small coherent vortex at the apex. At Reynolds number $Re = 2.5 \times 10^4$, the vortex breakdown location of the primary vortex appears closer to the apex region where the outboard vortex preserves its presence. For MDF planform at $Re = 1 \times 10^4$ a single leading edge vortex with a clear indication of breakdown close to mid-chord distance is observed. Increasing Reynolds number to $Re = 1.5 \times 10^4$, single vortex structure turns into dual vortex formation with an early breakdown for outboard vortex. Further increase in Reynolds number to $Re = 2 \times 10^4$ and

$Re = 2.5 \times 10^4$ moves the breakdown locations upstream toward the apex of the planform for both vortical structures.

Figure 4-5 demonstrates the results for different Reynolds numbers at angle of attack $\alpha = 10^\circ$. At Reynolds number $Re = 10^4$ BW planform is dominated by single large-scale vortex with breakdown location near mid chord distance. At Reynolds numbers $Re = 1.5 \times 10^4$ and $Re = 2 \times 10^4$ vortex core expands and location of breakdown moves slightly upstream. At $Re = 2.5 \times 10^4$ the breakdown location is near the apex region and dispersed flow covers the whole wing surface. On DF planform however, the overall flow structure demonstrates complete different behavior compared to BW planform. At Reynolds number $Re = 10^4$, a large-scale swirl, which is an indication of three-dimensional separation from the surface, dominates the flow structure over the wing surface. At $Re = 1.5 \times 10^4$, the spatial extent of this swirl pattern gets smaller and the core of it moves toward the apex of the planform. At Reynolds numbers $Re = 2 \times 10^4$ and $Re = 2.5 \times 10^4$, the disappearance of swirl pattern and recovery of LEV's with breakdown are evident. For MDF planform at $Re = 10^4$, large-scale swirl pattern is observed in a relatively smaller scale compared to DF planform. At Reynolds number $Re = 1.5 \times 10^4$, LEVs are apparent with an unsteady oscillation back and forth to swirl structures when considering series of pictures taken for the corresponding case (not shown here). Further increase in Reynolds numbers to $Re = 2 \times 10^4$ and $Re = 2.5 \times 10^4$ cause recovery of strong LEV's with clear indication of breakdown on planform.

In order to better identify the difference in flow structures between BW planform and DF planform and better understand aforementioned swirl pattern obtained in dolphin fluke planforms, Figure 4-6 is constructed for attack angle $\alpha = 10^\circ$ and Reynolds number $Re = 10^4$. Surface flow smoke visualization and cross flows smoke visualizations at three different chordwise distances $x/C = 0.32$, $x/C = 0.55$ and $x/C = 0.77$ are presented at the top and the bottom part of Figure 4-6

for BW and DF planforms, respectively. Considering the cross flow patterns along with the surface flow patterns for both planforms, apparent coherence in flow patterns at different measurement planes are witnessed. For BW planform, the top portion of the corresponding figure, LEVs are evident with apparent breakdown locations. Vortex core of the LEV is apparent as condensed smoke distribution at both cross-flow planes of $x/C = 0.32$ and $x/C = 0.55$ where the spatial extent of it is relatively larger at $x/C = 0.55$. However, at $x/C = 0.77$, the flow is dispersed and there is no evident of the vortex core, which is indicating the existence of breakdown upstream of the corresponding cross flow plane. On DF planform, there is a large-scale swirl pattern which is directly associated with three-dimensional separation from the surface of the planform. Cross flow visualizations at all three stations demonstrate coherence with the surface smoke visualization with dispersed smoke distributions covering large spatial extent at cross flow planes.

Surface smoke visualization results of three wing configurations for attack angle $\alpha = 12^\circ$ are illustrated in Figure 4-7. BW planform has three-dimensional surface separation at $Re = 10^4$. Increasing Reynolds number favors the formation of LEVs with breakdown, which are clearly evident at $Re = 1.5 \times 10^4$. Further increase in Reynolds number moves the breakdown location upstream toward the apex of the wing where it reaches to the apex region at Reynolds number $Re = 2.5 \times 10^4$ and smoke disperses and covers the whole wing planform. For DF planform, large-scale swirl pattern, indicating three-dimensional surface separation, is observed at $Re = 10^4$. Increase in Reynolds number moves the focus of swirl structure toward the apex of the wing with a significant reduction in the spatial extent of the pattern. At $Re = 1 \times 10^4$ the swirl pattern on DF planform has similar spatial extent as MDF planform, whereas on BW planform it has relatively smaller spatial extent. There is no significant variation between the flow structures of MDF and DF planforms except at relatively higher Reynolds number $Re = 2 \times 10^4$ where DF planform continues to indicate the swirl pattern.

Figure 4-8 presents the charts constructed for vortex breakdown locations of three planforms with respect to attack angles at different Reynolds numbers. The vortex breakdown location is normalized with chord length of the planforms and examples of these dimensions are shown on the right bottom part of the corresponding figure. It should be noted that the vortex breakdown locations on the charts represent calculated average values since average of 5 % chord length variations are evident particularly due to wandering behavior of the vortex structure in streamwise direction. There are also extreme cases where these values reach to 10 % of the chord distance.

The left chart in the upper row of Figure 4-8 indicates the vortex breakdown locations for the angle of attack $\alpha = 4^\circ$. As presented in this chart, the vortex breakdown locations are beyond the planform surface for all three planforms at $Re = 10^4$. This is also valid at $Re = 1.5 \times 10^4$ for BW planform whereas for DF and MDF planforms the breakdown appears at distances close to the mid-chord. As expected, increase in Reynolds number moves the breakdown locations upstream toward the apex region at all wing planforms. This location merges to 40% chord length for all wing planforms at $Re = 2.5 \times 10^4$.

The right chart in the top row of Figure 4-8 corresponds to the breakdown locations at attack angle of $\alpha = 6^\circ$. Considering the Reynolds number $Re = 10^4$, the breakdown location of the BW planform stays beyond the surface, whereas the locations appear in DF and MDF planforms are significantly different compared to the base wing planform and are evident at the vicinity of the mid-chord distance. At $Re = 1.5 \times 10^4$, the vortex breakdown location appears on the surface for BW planform. Further increase in Reynolds number to $Re = 2 \times 10^4$ leads a significant change in the location of breakdown at BW planform. All planforms have the similar breakdown locations close to 40% of the chord distance at the corresponding Reynolds number. When considering $Re = 2.5 \times 10^4$ and compared to $Re = 2 \times 10^4$, it is evident that BW and DF planforms show little reaction to

Reynolds number increase, whereas, the location appears to be at 27% chord distance for MDF planform, which can be considered as a significant shift.

The chart in the bottom row of Figure 4-8 indicates the vortex breakdown locations for the angle of attack $\alpha = 8^\circ$. Considering the breakdown locations at three wing planforms and the trend in breakdown location variations with respect to Reynolds number, aforementioned discussions for attack angles $\alpha = 4^\circ$ and $\alpha = 6^\circ$, demonstrated in the upper charts of Figure 9, are also valid for the angle of attack $\alpha = 8$. Increase in Reynolds number moves the breakdown locations upstream toward the apex region at all wing planforms. This location merges to 20% chord distance for all wing planforms at $Re = 2.5 \times 10^4$. According to the all charts indicated in Figure 9, it is evident that the base wing planform demonstrates significantly better performance compared to the MDF and DF planforms in considering the breakdown locations within the Reynolds number range used in the present study.

4.2 Conclusion

The present investigation aims to examine novel passive control techniques on non-slender delta wings based on bio inspiration to possibly eliminate stall or to delay vortex breakdown. The effect of leading edge and trailing edge modification is studied qualitatively via laser illuminated smoke visualization by comparing with a 45° swept base wing (BW) model at attack angles $4 < \alpha < 12$ deg and Reynolds numbers $10^4 < \alpha < 2.5 \times 10^4$. The edges of BW planform are modified and the planform is converted to a white-sided dolphin fluke geometry.

The results indicate that leading edge modification is quite effective on altering the overall flow pattern. On the contrary of the expectations, the stall performance of the modified planform deteriorates compared to the base wing planform. Particularly for $\alpha = 10^\circ$ and $\alpha = 12^\circ$, DF planform experiences stall earlier than

BW model. In addition, for the modified planforms, outboard vortex of the dual vortex structure forms a very stable whorl structure at relatively low angle of attacks $\alpha = 4^\circ$ and $\alpha = 6^\circ$. Trailing edge modification from DF to MDF planform does not indicate any substantial effect on stall performance of the wing. However as presented in next chapter, the effect of trailing edge seems to be more compared to leading edge effect at low Reynolds numbers.



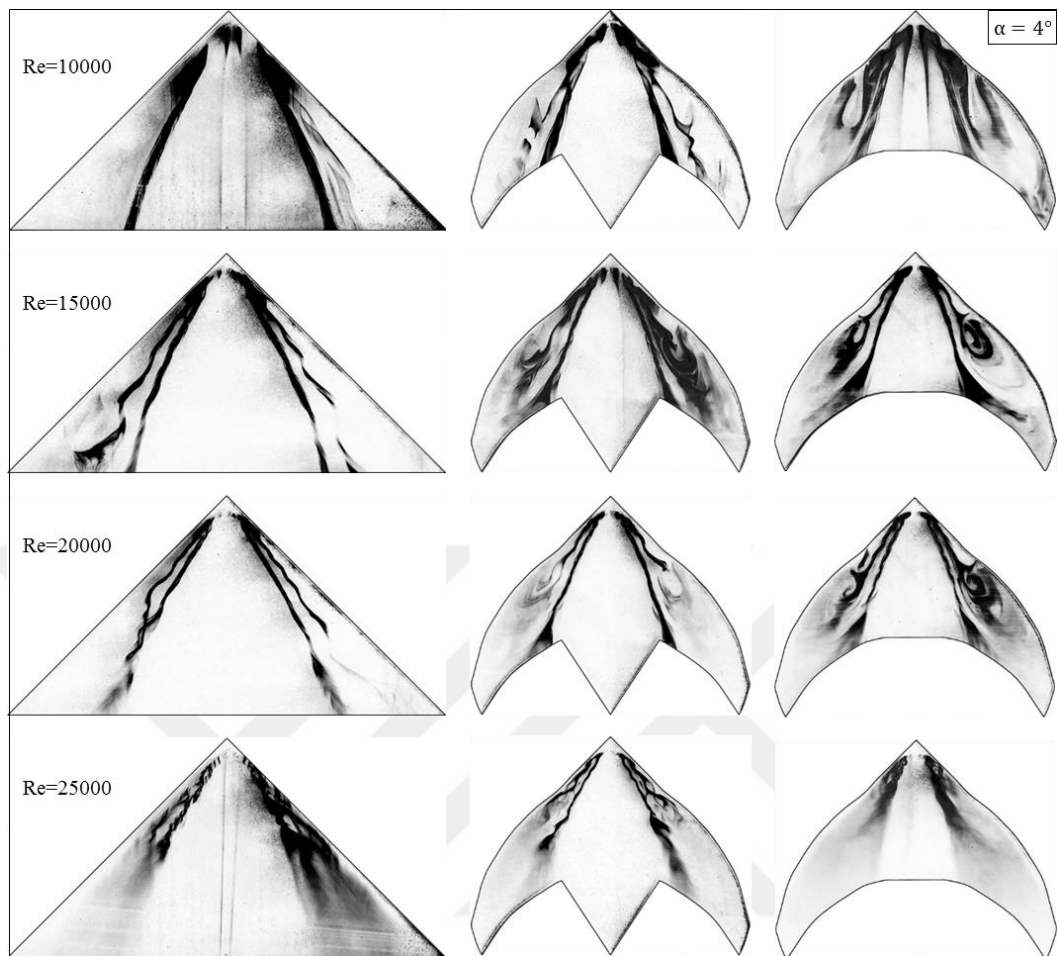


Figure 4-1 Surface flow smoke visualizations for base wing (BW), modified dolphin fluke (MDF), and dolphin fluke (DF) planforms for Reynolds numbers $Re = 10^4$, $Re = 1.5 \times 10^4$, $Re = 2 \times 10^4$ and $Re = 2.5 \times 10^4$ at attack angle of $\alpha = 4^\circ$

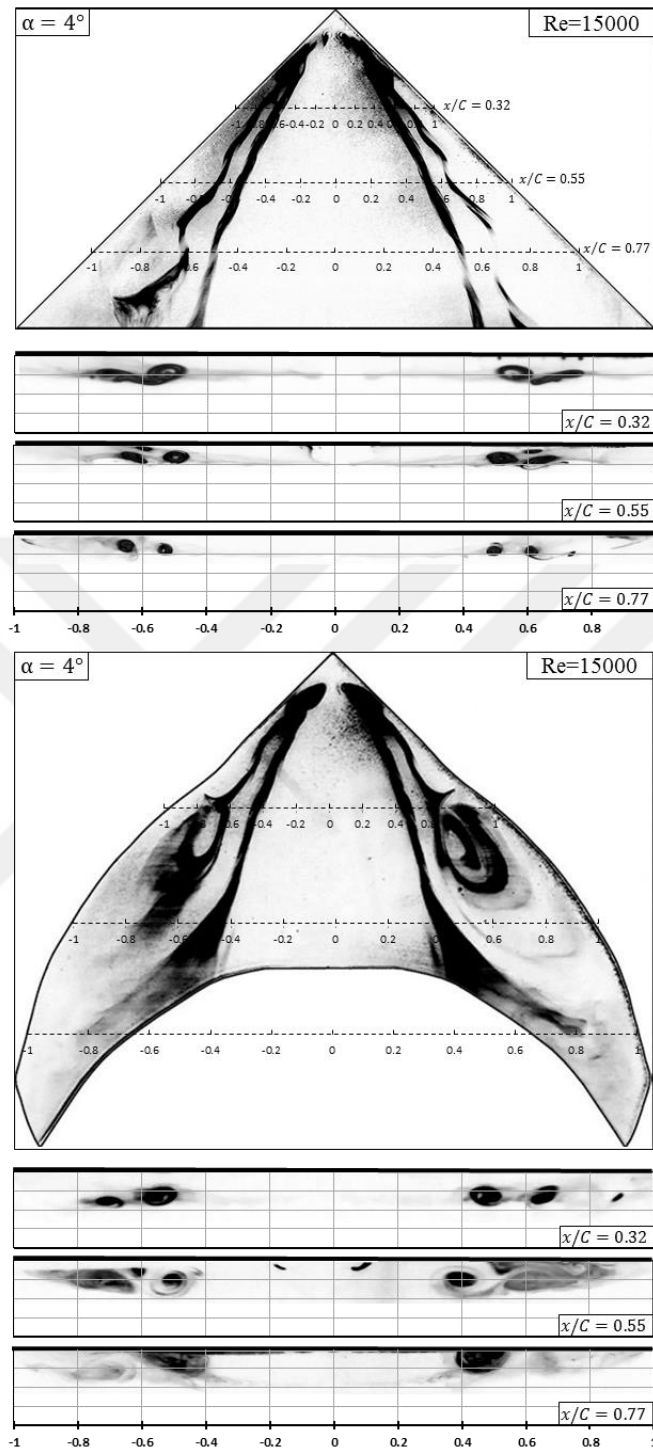


Figure 4-2 Comparison of surface and cross flow smoke visualizations for base wing (BW) and dolphin fluke (DF) planforms for $Re = 1.5 \times 10^4$ at attack angle of $\alpha = 4^\circ$.

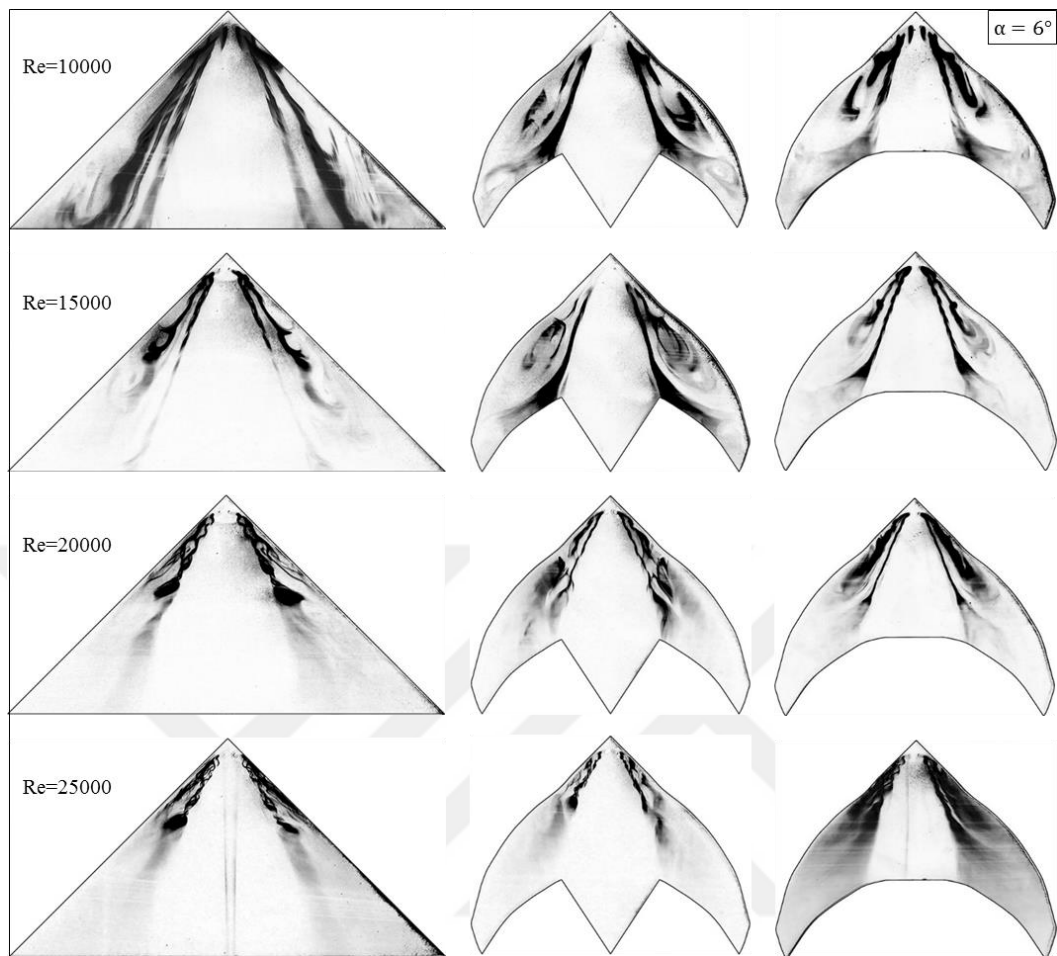


Figure 4-3 Surface flow smoke visualizations for base wing (BW), modified dolphin fluke (MDF), and dolphin fluke (DF) planforms for Reynolds numbers $Re = 10^4$, $Re = 1.5 \times 10^4$, $Re = 2 \times 10^4$ and $Re = 2.5 \times 10^4$ at attack angle of $\alpha = 6^\circ$.

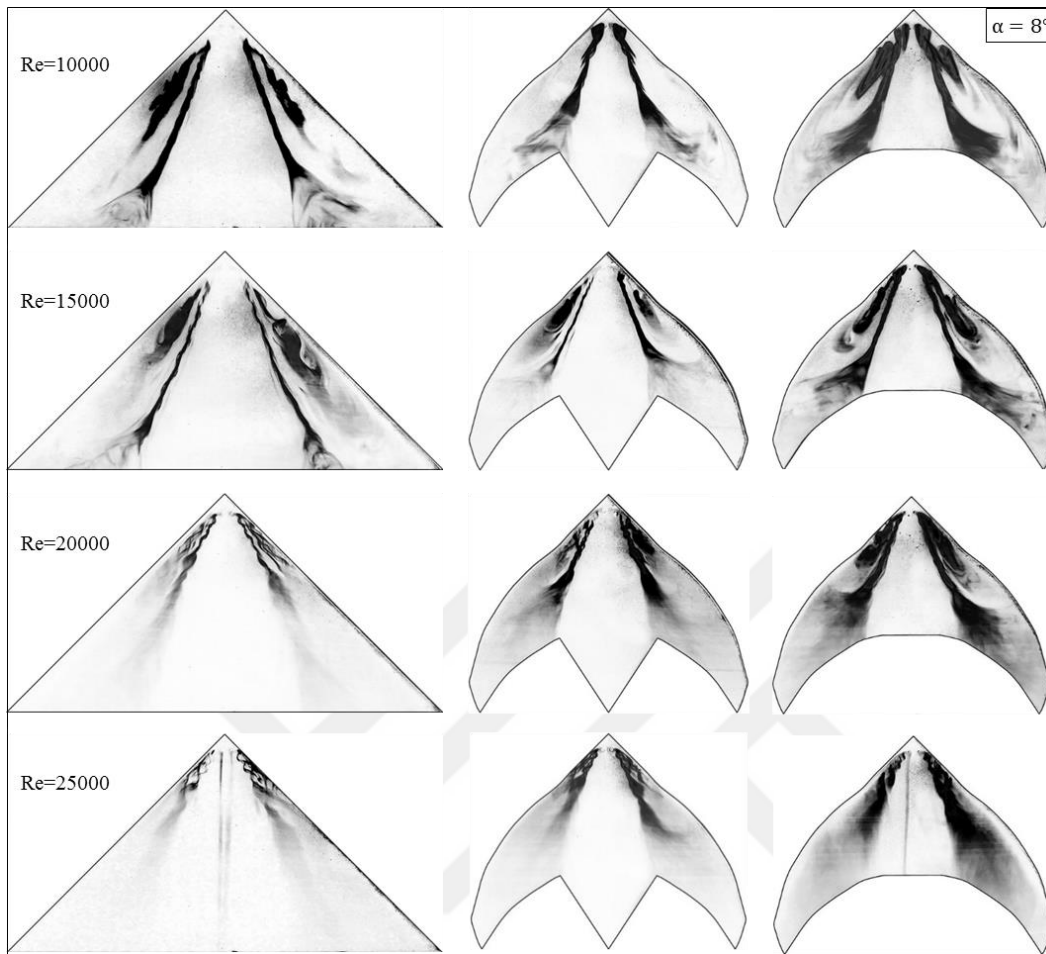


Figure 4-4 Surface flow smoke visualizations for base wing (BW), modified dolphin fluke (MDF), and dolphin fluke (DF) planforms for Reynolds numbers $Re = 10^4$, $Re = 1.5 \times 10^4$, $Re = 2 \times 10^4$ and $Re = 2.5 \times 10^4$ at attack angle of $\alpha = 8^\circ$.

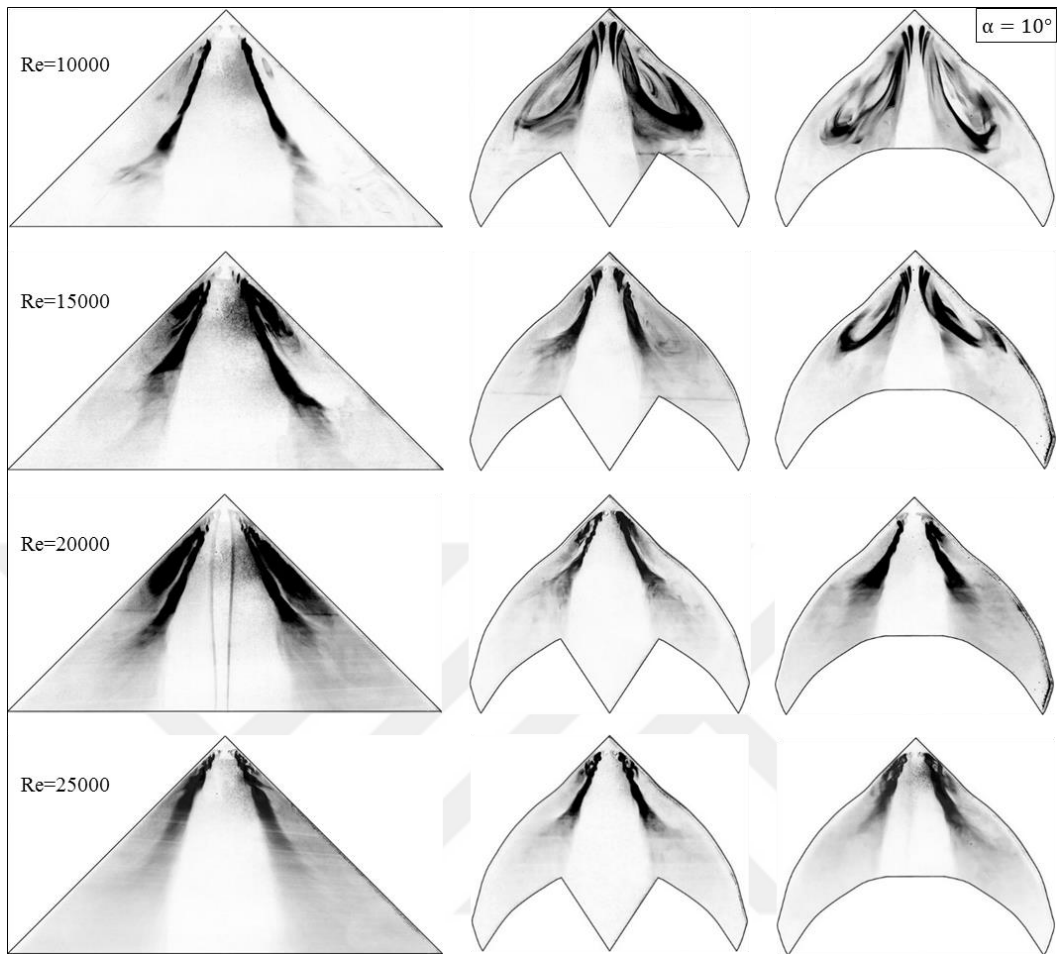


Figure 4-5 Surface flow smoke visualizations for base wing (BW), modified dolphin fluke (MDF), and dolphin fluke (DF) planforms for Reynolds numbers $Re = 10^4$, $Re = 1.5 \times 10^4$, $Re = 2 \times 10^4$ and $Re = 2.5 \times 10^4$ at attack angle of $\alpha = 10^\circ$.

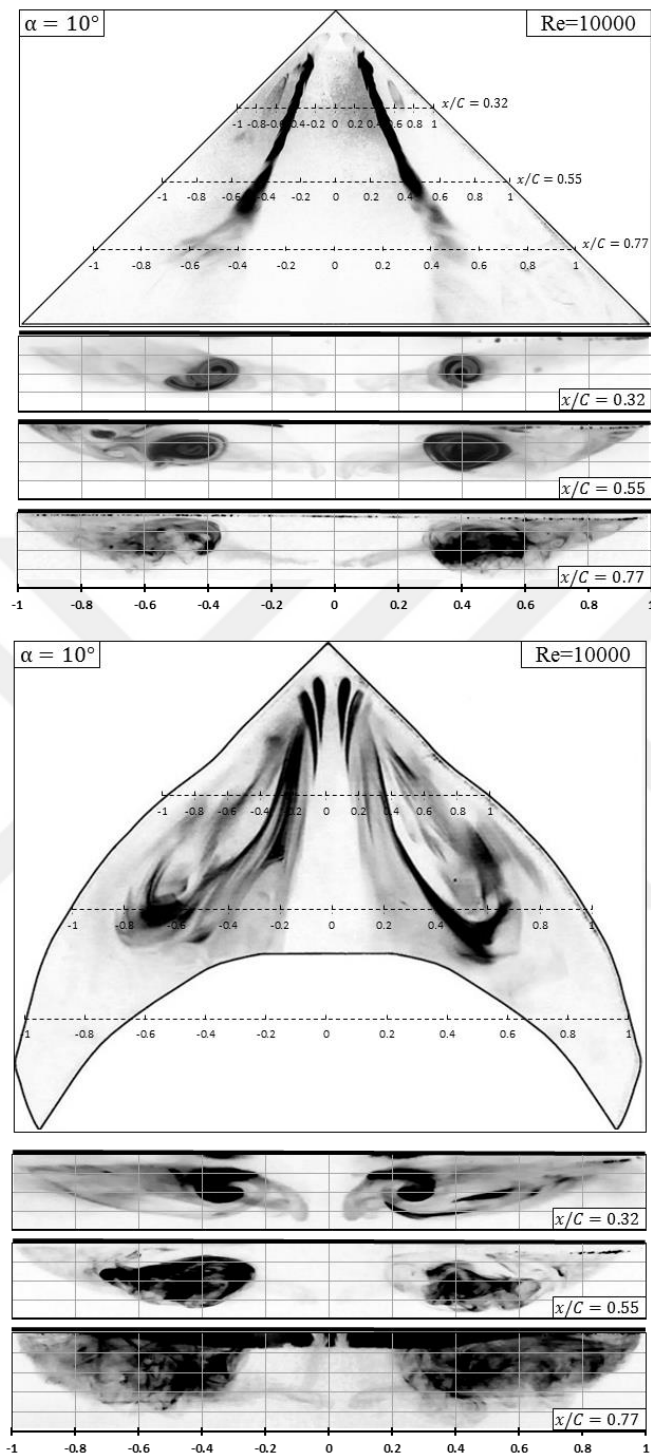


Figure 4-6 Comparison of surface and cross flow smoke visualizations for base wing (BW) and dolphin fluke (DF) planforms for $Re = 10^4$ at attack angle of $\alpha = 10^\circ$.

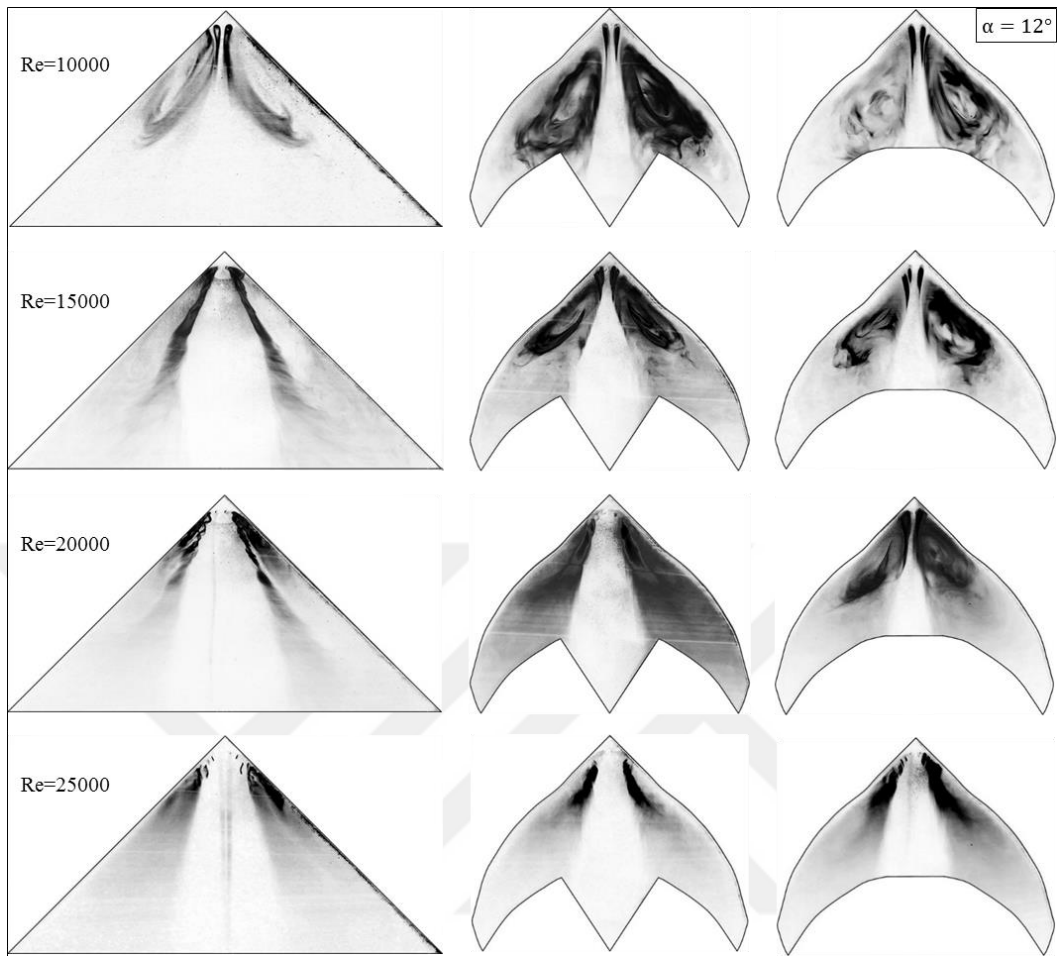


Figure 4-7 Surface flow smoke visualizations for base wing (BW), modified dolphin fluke (MDF), and dolphin fluke (DF) planforms for Reynolds numbers $Re = 10^4$, $Re = 1.5 \times 10^4$, $Re = 2 \times 10^4$ and $Re = 2.5 \times 10^4$ at attack angle of $\alpha = 12^\circ$.

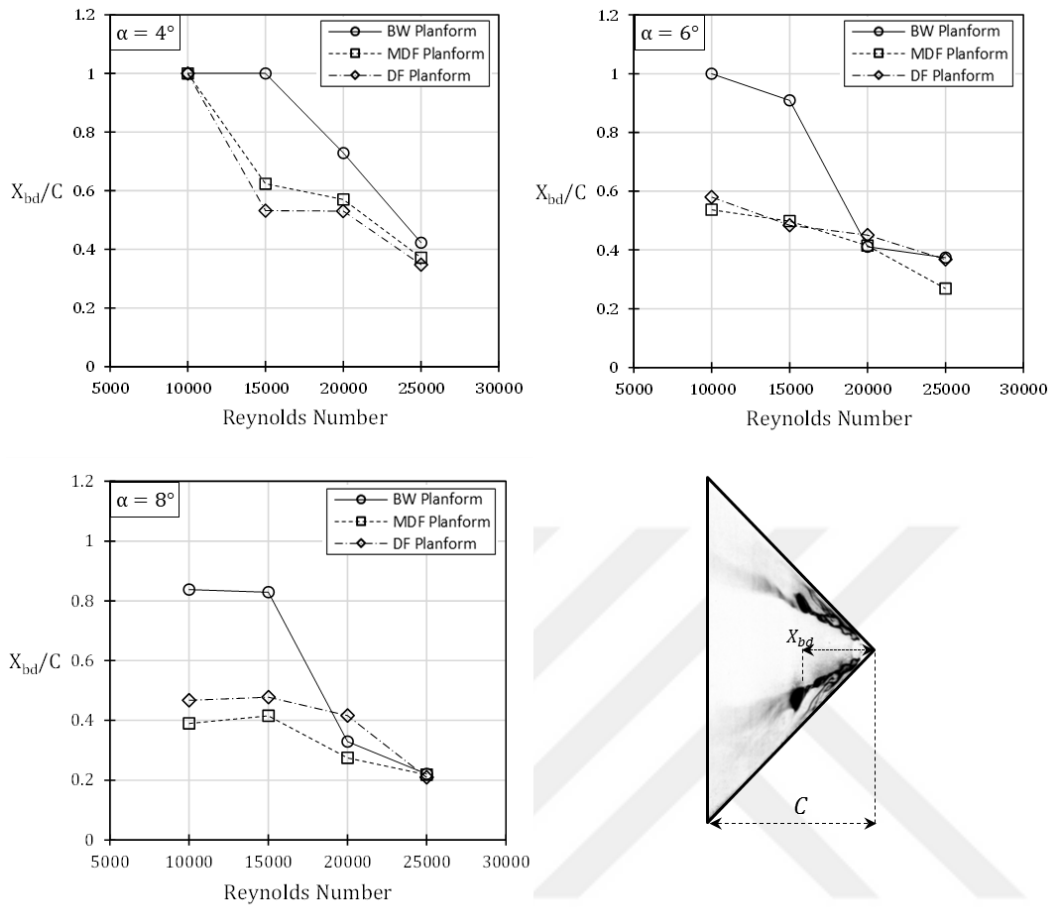


Figure 4-8 Vortex breakdown locations for attack angle of $\alpha = 4^\circ, 6^\circ$ and 8° at $Re = 10^4, Re = 1.5 \times 10^4, Re = 2 \times 10^4$ and $Re = 2.5 \times 10^4$.

CHAPTER 5

EFFECT OF EDGE MODIFICATIONS ON FLOW STRUCTURE OF A NONSLENDER DELTA WING -PART II

The present chapter is a continuum of the previous chapter, Part I, in which the results revealed that the edge modifications lead quite complex effects on the flow structures over the planform. Since the individual effects of leading edge modifications and trailing edge modifications could not be understood clearly with the wing models used in Part I, it was planned to apply each modification on Base planform separately. In this chapter, the effects of leading edge modification and trailing edge modification on flow structure and stall characteristic of a 45° swept delta wing were studied separately using laser illuminated smoke visualization technique. Moreover, a third planform, where the trailing edge modification was scaled up until the leading edge was also studied to obtain more information on the effect trailing edge modification. The chord C based on Reynolds numbers were $Re = 10^4$ and $Re = 2.5 \times 10^4$, and the attack angles were $\alpha = 4^\circ$, and 12° to observe the effect of individual modifications on extreme limits of the previous study on leading edge vortices, vortex breakdown, and three-dimensional separation from the wing surface.

5.1 Results and Discussions

Surface flow visualizations for all the wing planforms produced, Base wing (BW), only leading edge modified wing (OL), only trailing edge modification (OT), extended trailing edge modification (OTE), dolphin fluke (DF), and modified dolphin fluke (MDF) at attack angle $\alpha = 4^\circ$ and Reynolds number $Re = 10^4$ are demonstrated in Figure 5-1. The first column represents the BW, OT and OTE

and, the second column represents OL, MDF and DF from top to bottom, respectively.

As discussed in previous chapter, considering the surface flow visualization for the base wing (BW) at $Re = 10^4$, it is apparent that symmetrical single leading edge vortex structure without any indication of breakdown is dominating the flow over the planform. In addition, a very weak in nature, small filaments are also apparent on the outboard sides of these single vortices, which might be an early indication of second primary vortex. The second row of first column, demonstrates OT planform for the corresponding case. An apparent dual vortex structure is observed on OT planform, which is not observed on either BW or DF planform. On the third row, OTE planform has similar dual vortex structure with OT planform with an earlier vortex breakdown location which indicates that extending trailing edge modification deteriorates the flow structures and promotes vortex breakdown. It is interesting to note that although the spanwise location of trailing edges are different on OT and OTE planform, on both planforms the breakdown takes place just after the trailing edge. Moreover, both DF and MDF planforms also show a similar trend. Although in the first part of the study, it was concluded that the change in leading edge may be the major parameter affecting the breakdown location and deterioration of flow, this new set of experiments demonstrate that trailing edge may be the major parameter affecting the breakdown location. OL planform in the top image of second column shows flow features of both BW and DF. The vortical structure over the planform is very similar to BW planform in terms of the spanwise location and breakdown location which is not shown here. However, the outer filaments, which are tending to form a swirl structure is similar to DF planform, yet not as apparent as DF planform shown in the bottom image of the second column. However, the inner vortical structures last longer. For the dolphin fluke (DF) planform, these filaments are more apparent and believed to be indicating a second primary vortex. Figure 5-2 demonstrates the surface flow visualization results at $Re = 2.5 \times 10^4$ at attack

angle $\alpha = 4^\circ$. As indicated in previous chapter, DF planform experiences breakdown slightly earlier compared to BW planform. For OL planform, the flow structures are similar to DF planform. However, for OT and OTE, the breakdown location is very similar to that of Base planform. The smoke traces on OT and OTE planforms seem to be bended toward the symmetry plane.

Figure 5-3 presents the surface flow visualization results at attack angle $\alpha = 12^\circ$ at $Re = 10^4$. BW planform has three-dimensional surface separation at $Re = 10^4$ which is evident from the swirling structure over the planform. Although the three dimensional surface separation, i.e. swirl pattern, is observed on all planforms, the spatial extent, the distance between symmetric swirl patterns and the location of the core of the swirling patterns change among planforms. Considering the OL planform, the swirl patterns is smaller in extent and the core of the swirl is located at a similar chordwise distance from apex compared to BW planform. Moreover, the distance between swirl patterns are larger on OL planform. The results of OT, OTE, DF and MDF indicate that any kind of trailing edge modification increases the size of spatial extent and with closer swirling patterns compared to BW. Considering the results of OL and other planforms together, it can be argued that trailing edge region dominated the flow structures. At $Re = 2.5 \times 10^4$ in Figure 5-4, the results indicate that for all planforms the vortex breakdown location moves very close to wing apex and it is not possible to clearly identify the flow patterns of smoke tracers and not possible to draw a solid conclusion.

Figure 5-4 is constructed to clearly visualize all the planforms and the transition of flow structures from BW planform to DF planform via OT, OTE, OL and MDF planforms. Results of attack angle $\alpha = 4^\circ$ at $Re = 10^4$, $Re = 2.5 \times 10^4$ and $\alpha = 12^\circ$ at $Re = 10^4$, $Re = 2.5 \times 10^4$ are demonstrated from top to bottom respectively.

5.2 Conclusion

The present investigation aims to clarify the individual effect of trailing edge modifications and leading edge modification applied to a 45 deg swept base wing at attack angles $\alpha = 4$ and 12 deg, and Reynolds numbers $Re = 10^4$ and $Re = 2.5 \times 10^4$ qualitatively via laser-illuminated smoke visualization. The necessary edge modifications to modify the base planform into DF planform were applied one-by-one to understand their effect separately.

Although in previous chapter, it was implied that the DF planform may deteriorate flow due to the modification on leading edge, i.e., change in the nominal sweep angle that the flow encounters through the leading edge, the results presented in this chapter indicates that the main parameter leads to deterioration in flow structures is the trailing edge modifications. Comparing the vortex breakdown locations for all planforms with trailing edge modifications, i.e., DF, MDF, OT and OTE, the breakdown occurs just behind the trailing edge at $Re = 10^4$ at $\alpha = 4^\circ$, independent from where the trailing edge is located.

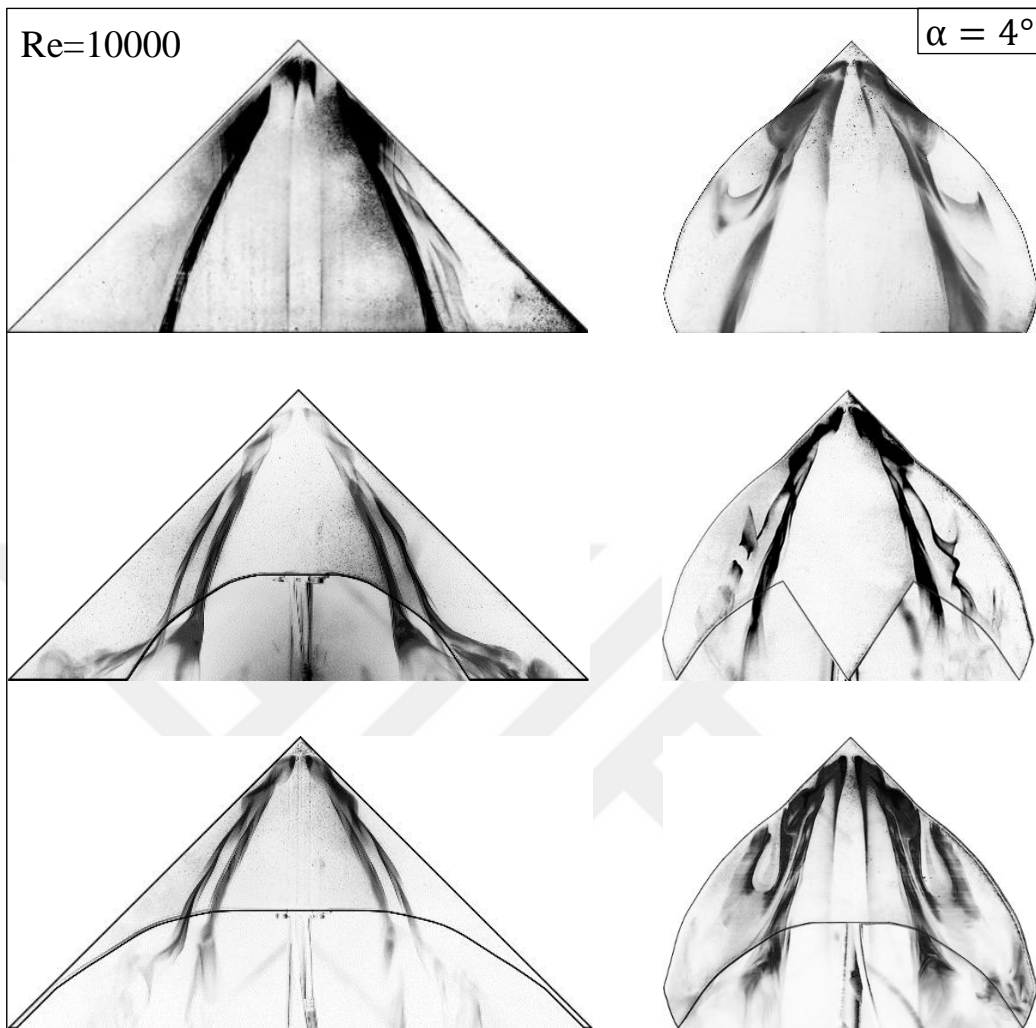


Figure 5-1 Surface flow smoke visualizations for BW, DF, OL, OT and OTE planforms for Reynolds numbers $Re = 10^4$ at attack angle of $\alpha = 4^\circ$.

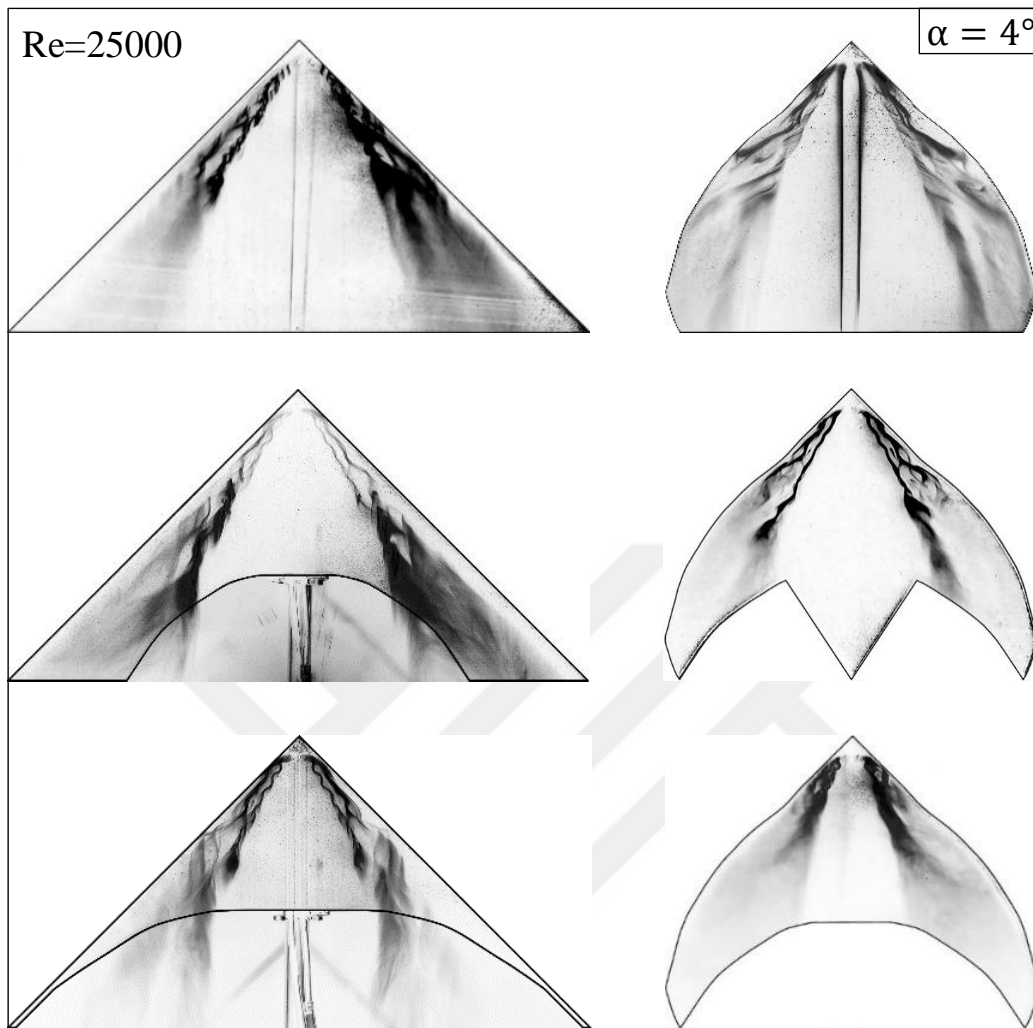


Figure 5-2 Surface flow smoke visualizations for BW, DF, OL, OT and OTE planforms for Reynolds numbers $Re = 2.5 \times 10^4$ at attack angle of $\alpha = 4^\circ$.

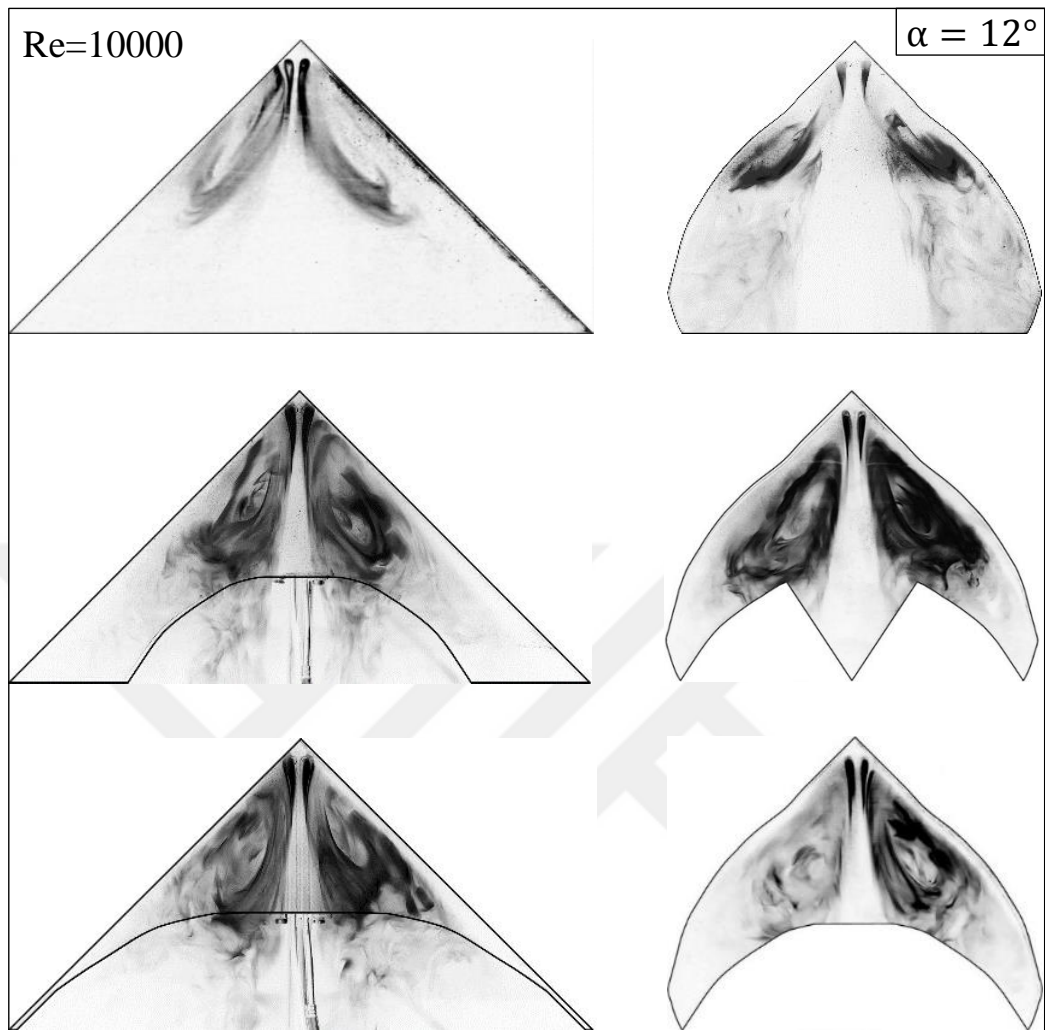


Figure 5-3 Surface flow smoke visualizations for BW, DF, OL, OT and OTE planforms for Reynolds numbers $Re = 10^4$ at attack angle of $\alpha = 12^\circ$.

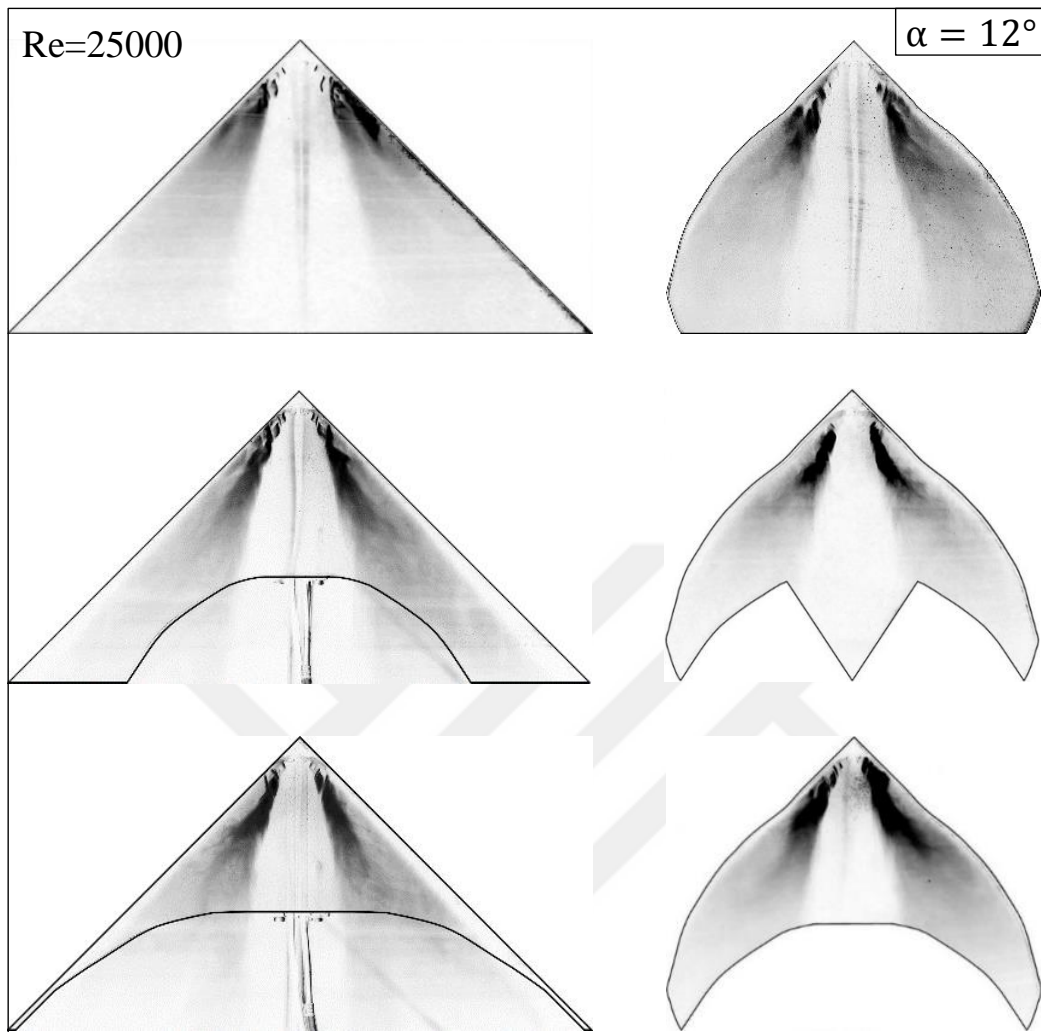


Figure 5-4 Surface flow smoke visualizations for BW, DF, OL, OT and OTE planforms for Reynolds numbers $Re = 2.5 \times 10^4$ at attack angle of $\alpha = 12^\circ$

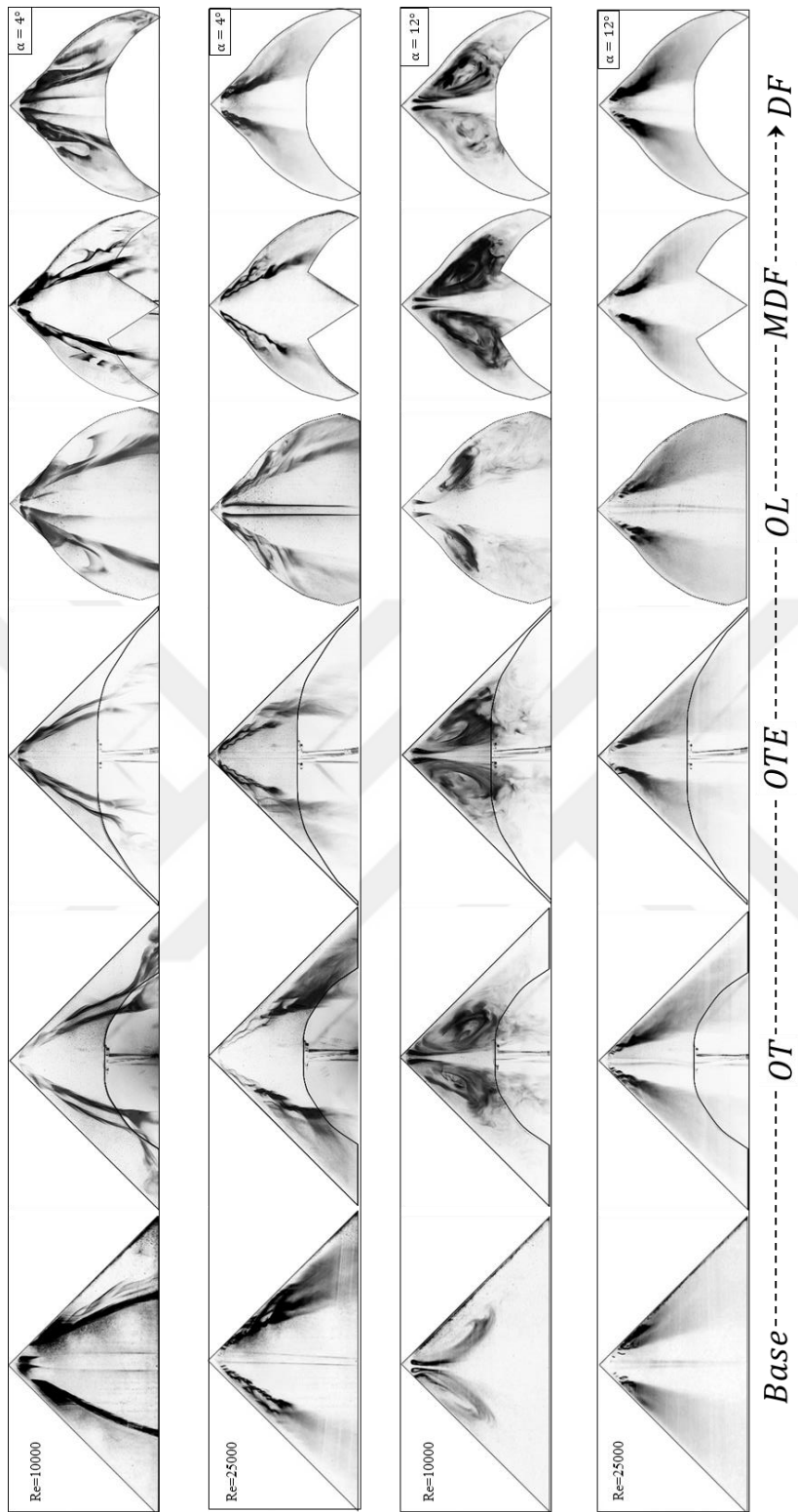


Figure 5-5 Comparison of whole planforms, at $Re = 1 \times 10^4$ and $Re = 2.5 \times 10^4$ at attack angles $\alpha = 4^\circ$ and $\alpha = 12^\circ$.



CHAPTER 6

EFFECT OF PASSIVE BLEED ON FLOW STRUCTURE OVER A NONSLENDER DELTA WING

This chapter explains the effect of passive bleeding on flow structure of a 45deg swept nonslender delta wing using techniques of laser-illuminated flow visualization, surface pressure measurements and PIV. Three different bleeding configurations were tested to identify the effectiveness of the control technique compared to a Base planform for a broad range of attack angles $6 < \alpha < 16$ deg at Reynolds numbers $Re = 10^4, 3.5 \times 10^4$ and 10^5 . Since this study is the first passive bleeding study on nonslender delta wings to the authors' best knowledge, locations of the bleed holes were chosen by considering the capability to mimic tangential blowing and trailing edge blowing studies as well as considering a recent passive bleed study [69] which was applied on low aspect ratio wings in literature. After initial trials on different wings, three wing models were chosen for further studies. The planforms with different bleeding configurations were named as Back (B), Edge (E) and Back & Edge (BE) referring to direction of the bleed air. Two major angles, θ and Φ , were defined where the details were given in Chapter 3. θ and Φ angle values (θ, Φ) for B, E and BE planforms were (18,90), (90,45), (18,45) respectively. The θ angle of the holes were chosen such that at highest angle of attack, where three-dimensional flow separation is most likely to occur over planform, mass transport from pressure side to suction side was maximum. The value of the angle Φ is defined such that the air leaves leading edge tangentially, hence same with bevel angle.

6.1 The Effect of Bleeding on Flow Structure at $Re = 10^4$

The effects of three different bleeding configurations, B, E, and BE planforms, on flow structures of 45 deg sweep delta wing are characterized at $Re = 10^4$. Figures 6-1, 6-2 and 6-3 demonstrate the cross-flow PIV results of bleeding experiments at chordwise distance of $x/C = 0.5$ for angle of attacks $\alpha = 6, 10$, and 16 deg, respectively. The figures are constructed using the same approach, where each row represents the time-averaged velocity vectors $\langle V \rangle$, the time-averaged streamline patterns $\langle \Psi \rangle$, and the contours of constant axial non-dimensional vorticity patterns $\langle \omega C/U \rangle$ for the half Base, B, E, and BE planforms from top to bottom, respectively. The length of the vector on the top left corner corresponds to the magnitude of the freestream velocity, $U = 1.13 \text{ m/s}$, which can be used for the comparison purposes of the velocity vectors shown in the first column. The contours of constant axial non-dimensional vorticity $\langle \omega C/U \rangle$ are illustrated such that solid (dark) and dashed (light) lines indicate, respectively, positive and negative contours, in which the positive orientation corresponds to axial vorticity in the direction of the outward normal. The constant contours of non-dimensional axial vorticity values are set same for all Re numbers and attack angles with minimum and incremental values of 7 and 2 respectively ($[|\langle \omega C/U \rangle|]_{min} = 7$ and $[|\Delta \langle \omega C/U \rangle|] = 2$).

Figure 6-1 represents the results at attack angle $\alpha = 6$ deg for $Re = 10^4$. The patterns of time-averaged streamline, velocity vectors, and vorticity contours clearly indicate that bleeding, apparent in all configurations, causes quite complex flow structures over the planform and moves the reattachment inboard toward the wing center. There is an indication of an additional swirl structure, which is the most prominent in the planform E as shown in the third row of Figure 6-1. Considering the patterns of constant contours of axial non-dimensional vorticity $\langle \omega C/U \rangle$ for the Base planform, there is a footprint of dual vortex structure with very high vorticity concentrations in the inboard vortex close to the symmetry

plane. The secondary vortex as shown with positive vorticity contours extends towards the normal direction and splits the primary vortex, which is clearly supported by the streamline patterns and the velocity vectors. Bleeding causes substantial variations in vorticity contours and transforms the patterns into unique structures not commonly observed at this low attack angle. Considering the planform B, there is an elongated vorticity pattern from the leading edge, which feeds the primary vortex and leads to relatively higher vorticity concentrations. Approximately 20 % increase in the maximum levels of the contours of constant vorticity is achieved with bleeding configuration of planform B compared to the Base planform. Vorticity patterns of planform E indicate that this bleeding configuration adversely affects the vorticity formation. Separated vorticity concentrations with a maximum value of 50 % less than the vorticity levels in Base planform are obtained in this bleeding configuration. This observation is well in line with the study of Hu et al [69] where it is stated that bleeding closer to leading edge tends to deteriorate the shear layer feeding mechanism. Planform BE, which corresponds to the last row of Figure 6-1, has vorticity patterns similar to the patterns obtained by bleeding configurations of B and E planforms. For this configuration, the deterioration in the vorticity patterns is not as dramatic as the one generated by the planform E and the improvement in the strength of vorticity concentrations is not as strong as the one achieved by the planform B.

The corresponding patterns for the attack angle $\alpha = 10$ deg are demonstrated in Figure 6-2. In line with the aforementioned observations for the attack angle $\alpha = 6$ deg as indicated in Figure 6-1, bleeding moves the reattachment inboard toward the symmetry plane. The contours of non-dimensional axial vorticity $\langle \omega C/U \rangle$ indicate that the condensed vorticity region on Base planform disperses on all planforms with bleeding. None of the bleeding configurations causes any improvement in the strength of the vorticity concentrations, which is different than the observation at the attack angle $\alpha = 6$ deg. Considering the patterns of bleeding configuration for the planform E, a complete deterioration of the

vorticity patterns is witnessed, which also causes the disappearance of the reattachment. The bleeding configuration of planform B seems to have the least deterioration of vorticity patterns and closest to the patterns of Base planform among all bleeding configurations.

Figure 6-3 demonstrates the cross-flow patterns for the attack angle $\alpha = 16$ deg. Considering the flow patterns of Base planform, separated flow, without any indication of strong reattachment, is evident, which also causes the disappearance of vorticity concentrations with the defined minimum levels. The cross-flow patterns indicate that bleeding, apparent in all configurations, causes improvement in the flow field with significant increases in the strength of the reattachment as indicated by high magnitude velocity vectors close to the wing center. In addition, elongated vorticity patterns due to the feeding mechanism of shear layer are apparent in all bleeding configurations. The most prominent improvement is obtained by the bleeding configuration of planform B, where the reattachment is relatively stronger and the vorticity concentrations are apparent, which might be considered as the footprint of the recovery of vortical structure on the planform.

In order to complement the PIV cross-flow measurements, laser illuminated smoke visualizations are presented for a selected case. Figure 6-4 shows the results of surface and cross-flow smoke visualizations for all bleeding planforms along with the Base wing for $Re = 10^4$ at angle of attack $\alpha = 6$ deg. The dimensionless length scales indicating the spanwise position at cross-flow plane $x/C = 0.5$ are added to both surface and cross-flow images to identify the spatial extent and the corresponding locations of smoke distributions representing the streaklines emanating from the wing apex. From top to bottom, Base, B, E and BE planform images are presented, respectively. The results indicate that all cross-flow images are well in-line with the surface flow images. A clear indication of dual vortex structure with the breakdown locations just over the trailing edge is evident for the Base planform. As discussed in the PIV results of Figure 6-1, when the bleeding is considered, additional swirl patterns, emanating from the bleed

slots, are clearly apparent on the crossflow smoke visualizations. For the bleeding configuration of planform B, there is a shift of primary vortex inboard toward the wing center along with a slight movement of breakdown downstream. This might be associated with the increase in the levels of vorticity contours for this bleeding configuration as indicated in Figure 6-1. To draw more concrete conclusions regarding the improvement in the breakdown location with this bleeding configuration, broad ranges of attack angles and Reynolds numbers need to be investigated. Considering the bleeding configurations of planforms E and BE, very complex flow structures are obtained which completely support the aforementioned observations as indicated by the discussions of the results of Figure 6-1.

6.2 The Effect of Bleeding on Flow Structure at $Re = 10^5$

Figures 6-5, 6-6 and 6-7 demonstrate the cross-flow PIV results of Base planform and bleeding configurations including B, E, and BE planforms at $Re = 10^5$ for the attack angles $\alpha = 6, 10,$ and 16 deg, respectively. As described in the previous section for the results of $Re = 10^4$, shown in Figures 6-1, 6-2, and 6-3, the figures are constructed using the same approach, where each row represents the time-averaged velocity vectors $\langle V \rangle$, the time-averaged streamline patterns $\langle \Psi \rangle$ and the contours of constant axial non-dimensional vorticity patterns $\langle \omega C/U \rangle$ for the half Base, B, E, and BE planforms from top to bottom, respectively. The length of the vector on the top left corner corresponds to the magnitude of the freestream velocity, $U = 11.3 \text{ m/s}$, which can be used for the comparison purposes of the velocity vectors shown in the first column. The contours of constant axial non-dimensional vorticity $\langle \omega C/U \rangle$ are illustrated such that solid (dark) and dashed (light) lines indicate, respectively, positive and negative contours, in which the positive orientation corresponds to axial vorticity in the direction of the outward normal. The constant contours of non-dimensional axial vorticity values are set same for all Re numbers and attack angles with

minimum and incremental values of 7 and 2 respectively ($[\omega C/U]_{min} = 7$ and $[\Delta(\omega C/U)] = 2$).

Figure 6-5 represents the results at attack angle $\alpha = 6$ deg for $Re = 10^5$. The patterns of time-averaged streamlines, velocity vectors, and vorticity contours indicate that the flow structure over the Base planform significantly changes with all bleeding configurations. Considering the planform B, the core of vortical structure and the overall concentration of the elongated vorticity pattern move slightly inboard toward the symmetry plane. In addition, in this bleeding configuration, there is significant increase in the maximum levels of the vorticity, approximately 40 %, compared to the Base planform. The bleeding configuration of planform E, as shown in the third row of the Figure 6-5, transforms flow structure into unique patterns, including two discrete vorticity concentrations, which is also evident in the streamline topology with two focal points. Considering the vorticity concentrations, the highest peak values are detected close to the leading edge of the planform. There is also an indication of weak vorticity concentration due to the reattachment region, which can be considered as the third vortical pattern. For this configuration, the reattachment point appears much closer to the symmetry plane compared to the Base planform. The similar improvement in the strength of the vorticity concentrations obtained with the bleeding configuration B is also evident in the bleeding configuration BE. Although the inboard vorticity concentration decreases 30%, the peak value of the outboard concentration is 55% higher than the concentration region on Base planform. However, considering the overall pattern, the footprints of both bleeding configurations E and B are evident in the results of planform BE.

The cross-flow PIV results for the attack angle $\alpha = 10$ deg are presented in Figure 6-6 . It is evident that the aforementioned discussions of the results for the attack angle $\alpha = 6$ deg shown in Figure 6-5 are completely valid for the case $\alpha = 10$ deg. In summary, the effect of bleeding on flow structure includes the

movement of reattachment region inboard toward the symmetry plane and improvement in the strength of vorticity concentrations. The highest improvement in the strength of the vorticity concentrations is obtained with the bleeding configuration of planform B whereas the innermost movement of the reattachment point is achieved with the bleeding configuration of planform E. For all planforms two vorticity concentrations are evident. For B and BE planforms, 40% and 30% increases are achieved in the maximum levels of inboard and outboard vorticity concentrations, respectively.

The corresponding cross-flow patterns for attack angle $\alpha = 16$ deg are demonstrated in Figure 6-7. Considering the flow patterns of Base planform, there is an indication of separated flow, which has very low vorticity magnitudes and weak reattachment very close to the center of the wing. Similarly, the Planform E, shown in the third row of the Figure 6-7, has the reattachment in the proximity of symmetry plane and do not provide any noticeable improvement on the flow structure compared to the Base planform. The highest improvement in the flow field is obtained with the bleeding configuration of planform B where a significant increase in the strength of the vorticity concentrations is evident. Approximately 90% increase in maximum level of constant contours of non-dimensional vorticity is achieved. In addition, the overall flow pattern indicates the recovery of the vortical structure and thus the eradication of separated flow when considering the general shape and the spatial extent of the vorticity contours, which can be considered as the utmost influence of bleeding on flow structure. Considering the bleeding configuration of planform BE, there is an increase in the strength of the vorticity concentrations, approximately 45% in the maximum levels in the region of interest, which seems to be insufficient for the elimination of separated flow.

6.3 The Effect of Bleeding on Surface Pressure Measurements: *Reynolds Number Dependence*

The surface pressure measurements are conducted at Reynolds numbers $Re = 3.5 \times 10^4$, and $Re = 10^5$ at chordwise distance $x/C = 0.5$ for all planforms including Base, B, E and BE. Figure 6-8 demonstrates the results of pressure measurements in terms of $-C_p$ values for all four planforms at $Re = 3.5 \times 10^4$ on the left column and $Re = 10^5$ at the right column for the attack angles of $\alpha = 6, 10$ and 16 deg from top to bottom, respectively. The horizontal axis represents the non-dimensional spanwise distance, y/S , measured from the symmetry plane of planform. The highest $-C_p$ values indicate the highest suction areas, whereas the lowest $-C_p$ values represent the locations at which the flow reattaches to the wing surface.

Considering the $-C_p$ distributions for the attack angles $\alpha = 6$ deg and $\alpha = 10$ deg at $Re = 3.5 \times 10^4$ shown in the top and the middle charts of the left column in Fig. 9, respectively, the peak $-C_p$ values decrease, which indicate drop in suction, and the corresponding locations appear closer to the center of the planform in all bleeding configurations. The similar behavior is also evident in the locations of the lowest $-C_p$ values, which are the indication of the reattachment region. The highest deviation in the $-C_p$ distribution compared to Base planform is obtained with the bleeding configuration of planform E, which has the maximum drop of 28 % in the values of suction peaks in average of both attack angles. The $-C_p$ distributions of the bleeding configurations of planforms B and BE are quite similar. In addition, as the attack angle increases from $\alpha = 6$ deg to $\alpha = 10$ deg, it is also evident that the suction peak and the reattachment location shift toward the center of the planform indicated by $-C_p$ distributions as expected. Considering the results at $\alpha = 16$ deg, Base, E and BE planforms have flat-like $-C_p$ distributions which are the indication of separated flow over the planforms. However, $-C_p$ distribution of planform B demonstrates the footprints of vortical structures and flow reattachment to the wing surface. Thus, it can be concluded that the elimination of the separated flow is succeeded with the bleeding

configuration of planform B. Considering the $-C_p$ charts for $Re = 10^5$ shown at the right column of Figure 6-8, the general trends of $-C_p$ distributions are quite similar with that of $Re = 3.5 \times 10^4$ for all angle of attacks. In addition, as the Reynolds number increases the overall flow structure including the location of the suction peak and the reattachment region shift outboard toward the leading edge. Increase in Reynolds number causes increase in the highest $-C_p$ and decrease in the lowest $-C_p$, which indicate stronger suction and reattachment on the wing surface. The elimination of three-dimensional separation may also be an indication of elimination of stall and increase in lift force. All these observations are well in line with the aforementioned discussions where the cross-flow PIV results are presented.

A detailed comparison of the Base wing and the bleeding configuration of planform B is presented in Figure 6-9 using the results of constant contours of non-dimensional vorticity and pressure measurements at $Re = 3.5 \times 10^4$ and $Re = 10^5$ for attack angle $\alpha = 16$ deg along with the surface and cross-flow visualizations at $Re = 3.5 \times 10^4$. The figure is constructed such that the left side represents the results for the Base wing and the right part represents the results for planform B. The dimensionless length scales indicating the spanwise position at cross-flow plane $x/C = 0.5$ is added to both surface and cross-flow images to identify the spatial extent and the corresponding locations of smoke distributions. Both surface and cross-flow visualization results show that on Base wing, the flow is completely dispersed on the wing planform, and flow reattachment is on the symmetry line, which might be interpreted as pre-three-dimensional surface separation. Considering the bleeding configuration of planform B, the flow indicates a vortical like flow structure with flow reattachment location appearing at the vicinity of $y/S = 0.25$. The corresponding vorticity contours and $-C_p$ distributions at $Re = 3.5 \times 10^4$ are in line with the surface and cross-flow visualization results. The dispersed vorticity concentration on Base planform turns into a typical representation of vortical structure emanating from the separated

shear layer on B planform. $-C_p$ distributions, which are presented at the bottom part of the Figure 6-9, support these observations. $-C_p$ results of Base wing show a flat-like distribution, which might be interpreted as the pre-three-dimensional surface separation, whereas, on B planform the apparent hump-like pattern indicates the footprint of the vortical structure on the planform. The increase in Reynolds number to $Re = 10^5$ lowers the vorticity concentration on Base planform, however there is no significant variation in the overall distribution of vorticity concentration on the bleeding configuration of planform B. The peak value of the inboard vorticity concentration remains same, whereas the outboard vorticity concentration, corresponding to shear layer emanating from the leading edge, has an approximately 25% increase in the peak value. Considering the surface pressure distributions, increase in Reynolds number increases the $-C_p$ values significantly, which indicates stronger suction over the planform B, whereas there is no significant change in $-C_p$ distributions indicated for the Base planform.

6.4 The Effect of Bleeding on Pressure and Velocity Fluctuations

Surface pressure fluctuations and surface normal velocity fluctuations are directly related to buffeting, i.e. unsteady loading on planforms as addressed in Ozgoren et al [31]. The contours of constant non-dimensional axial vorticity $\langle \omega C/U \rangle$ and contours of constant non-dimensional root-mean square of vertical velocity fluctuation w_{rms}/U for Base (on the left) and B (on the right) planforms for attack angle $\alpha = 16$ at $Re = 3.5 \times 10^4$ and $Re = 10^5$ are presented at the top and bottom part of Figure 6-10, respectively. In general, the results indicate that the patterns of $\langle \omega C/U \rangle$ and w_{rms}/U are closely related in terms of the spatial extent of the contours and the location of the peak values as mentioned by Yaniktepe and Rockwell [108]. Considering the $Re = 3.5 \times 10^4$ case, shown on the top portion of the figure, the broad patterns of w_{rms}/U on Base planform,

which is covering the whole semi-span and attached to wing surface, becomes smaller in terms of spatial extent on planform B. Moreover, the concentrated region of w_{rms}/U near the reattachment region moves away from the surface on planform B without any increase in magnitude compared to Base planform. Considering the $Re = 10^5$ case, demonstrated on the bottom part of the figure, the overall trend is similar to $Re = 3.5 \times 10^4$. The peak values of w_{rms}/U on B planform are 30% higher compared to the values on Base wing. In addition, with bleeding, the spatial extent of w_{rms}/U gets smaller and the concentration at the vicinity of reattachment region moves away from the surface as observed at $Re = 3.5 \times 10^4$.

Figure 6-11 is constructed to demonstrate the effect of passive bleeding on buffeting characteristics for each planform at $Re = 3.5 \times 10^4$. Contours of constant non-dimensional root-mean square of vertical velocity fluctuation w_{rms}/U and root-mean square of pressure fluctuations $C_{p,rms}$ are plotted on the left and the right columns for the attack angles $\alpha = 6$ deg and $\alpha = 16$ deg, respectively. The vertical axis of the figures represents $C_{p,rms}$ values. Considering the results at angle of attack $\alpha = 6$ deg, constant contours of w_{rms}/U do not show any significant variation between the Base and B planforms, in terms of the spatial extent and magnitude of the contours. However, on planform E, velocity fluctuations slightly attenuate and spatially extend over the entire surface of the planform. Considering the BE planform, reduction in spatial extent of w_{rms}/U contours is evident. The peak value locations of $C_{p,rms}$ plot on Base planform are well in line with the highest concentration region of w_{rms}/U . Zharfa et al [109] reported that maximum $C_{p,rms}$ values exist between the vortical core and reattachment line for a nonslender delta wing. This observation is valid for the cases within this study. Considering the time-averaged streamline and vorticity patterns, which is not shown here, the peak $C_{p,rms}$ value occurs between the focus of swirl pattern and reattachment location, and the trend of $C_{p,rms}$ values as well as w_{rms}/U is well-in line with vorticity patterns. Similar observations are valid

for B, E and BE planforms, where there is a peak $C_{p,rms}$ value over the highest concentrated w_{rms}/U contour region. Considering the results at attack angle $\alpha = 16$ deg, the patterns of w_{rms}/U are dramatically broadened, covering the whole semi-span planform surface. The fluctuation contour patterns have a clear relation with leading edge, as in vorticity contours which are not here. The smallest w_{rms}/U values are observed on E planform. The spatial extent of constant contours of w_{rms}/U are smallest on B planform. The $C_{p,rms}$ values increased compared to $\alpha = 6$ deg for all planforms. On B planform, where the vortical structures are recovered, $C_{p,rms}$ value shows a significant peak in line with high concentration region of w_{rms}/U . Base, E and BE planforms however do not have a significant peak compared to B planform. The peak value locations of vorticity and velocity fluctuations quite overlap, which are not shown here.

6.5 Conclusion

The focus of the present study is to have the basic understanding on the effect of passive bleeding on flow structure of a nonslender delta wing, since it is the first bleeding study applied to nonslender delta wing to the best of authors' knowledge. For this purpose, the experiments were conducted in a low speed wind tunnel for a broad range of Reynolds numbers $10^4 \leq Re \leq 10^5$ and attack angles $6 \leq \alpha \leq 16$ deg using four different 45 deg swept delta wing including three different bleed configurations and a base planform. The techniques of laser-illuminated smoke visualization, surface-pressure measurements, and Particle Image Velocimetry were employed. The following main conclusions are drawn from the results of the present study:

- 1) Passive bleeding seems to be quite effective in terms of altering the entire flow field over the planform.

- 2) At relatively low angle of attacks, i.e. $\alpha=6$ and 10 deg, the bleeding causes reduction in the magnitudes of suction pressure coefficient $-C_p$ in general, which indicates loss in suction performance of the planform.
- 3) For low incidences, i.e. $\alpha = 6$ deg at $Re = 10^4$, surface and cross-flow smoke visualizations indicate that the bleeding configuration of planform B delays the appearance of vortex breakdown and moves the corresponding location downstream.
- 4) At angle of attack $\alpha=16$ deg, where pronounced surface separation appears on the Base planform, the recovery of the vortical structures with significant increases in the magnitude of suction pressure coefficient $-C_p$ is achieved with the bleeding configuration of planform B. This suggests that the proper bleeding configuration induces significant improvement on the overall flow pattern with eliminating the three-dimensional separation on the wing surface.
- 5) E planform, interfering the flow very close to leading edge, possibly distorts the shear layer feeding mechanism on planform and leads to substantial deterioration of flow structures for all cases. This observation is well in line with the study of Hu et al [69].

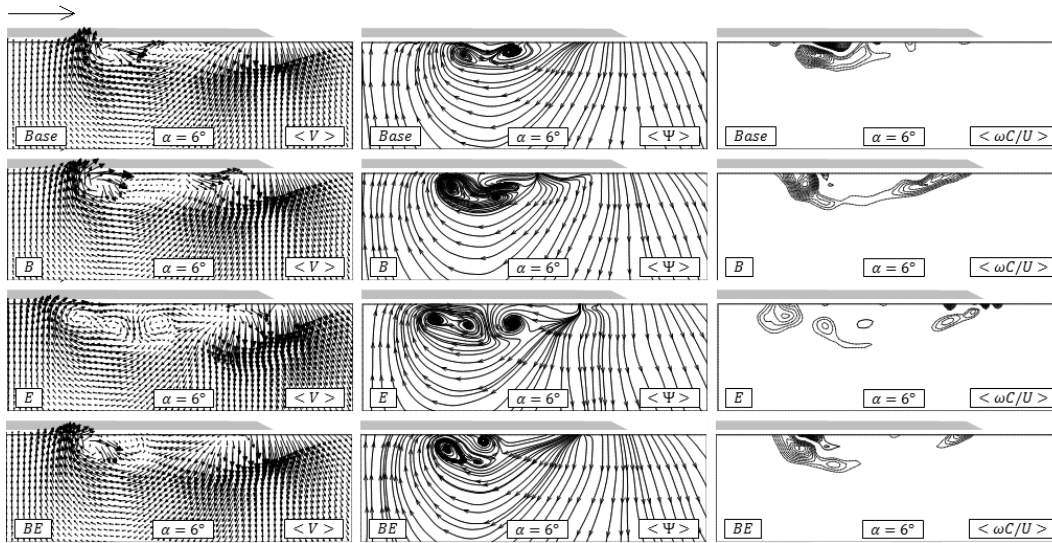


Figure 6-1 Patterns of time-averaged velocity vectors $\langle V \rangle$, streamlines $\langle \Psi \rangle$ and constant contours of non-dimensional axial vorticity $\langle \omega C/U \rangle$ at angle of attack $\alpha = 6$ deg for $Re = 10^4$: $[|\langle \omega C/U \rangle|]_{min} = 7$, $\Delta[|\langle \omega C/U \rangle|] = 2$

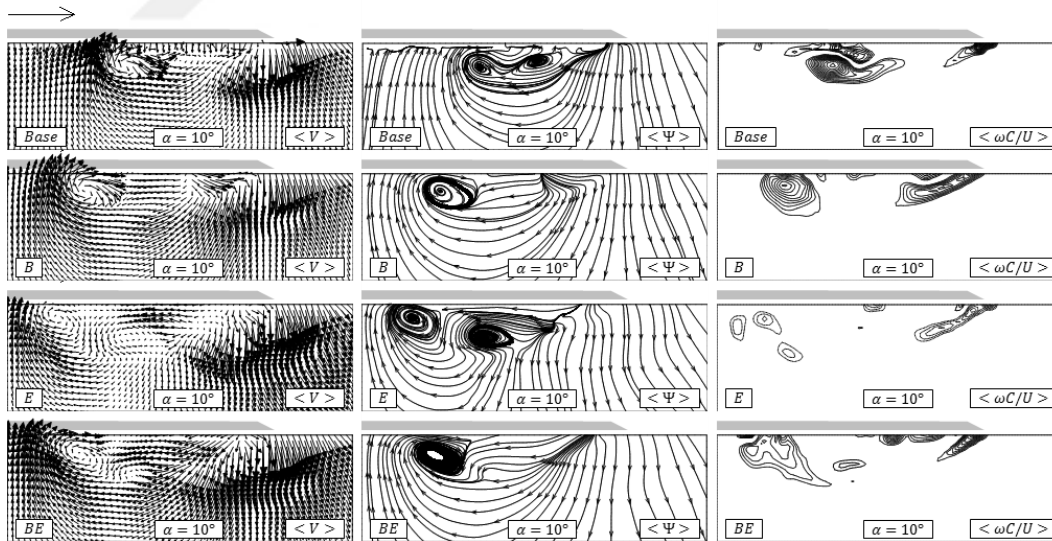


Figure 6-2 Patterns of time-averaged velocity vectors $\langle V \rangle$, streamlines $\langle \Psi \rangle$ and constant contours of non-dimensional axial vorticity $\langle \omega C/U \rangle$ at angle of attack $\alpha = 10$ deg for $Re = 10^4$: $[|\langle \omega C/U \rangle|]_{min} = 7$, $\Delta[|\langle \omega C/U \rangle|] = 2$

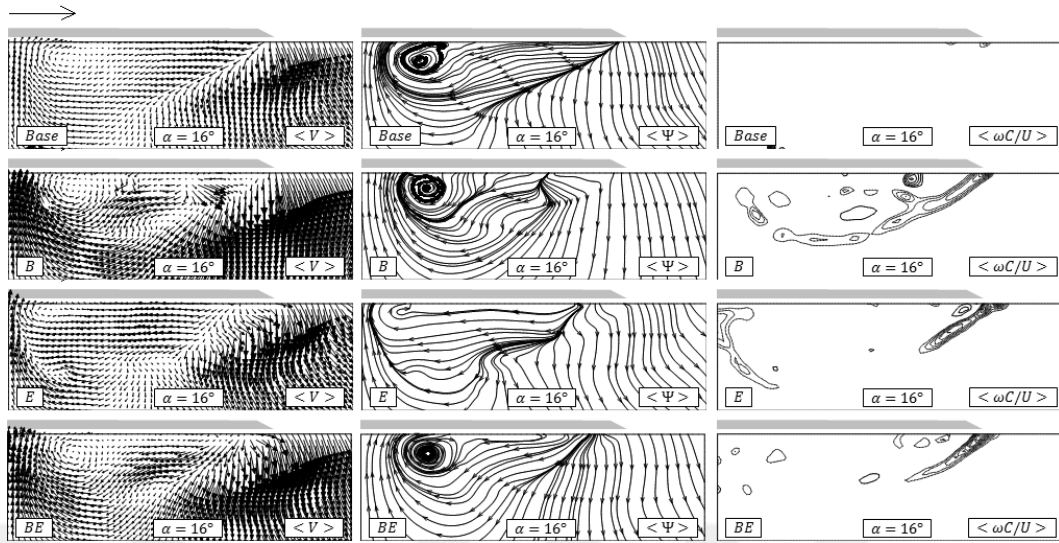


Figure 6-3 Patterns of time-averaged velocity vectors $\langle V \rangle$, streamlines $\langle \Psi \rangle$ and constant contours of non-dimensional axial vorticity $\langle \omega C/U \rangle$ at angle of attack $\alpha = 16$ deg for $Re = 10^4$: $[\langle \omega C/U \rangle]_{min} = 7$, $\Delta[\langle \omega C/U \rangle] = 2$

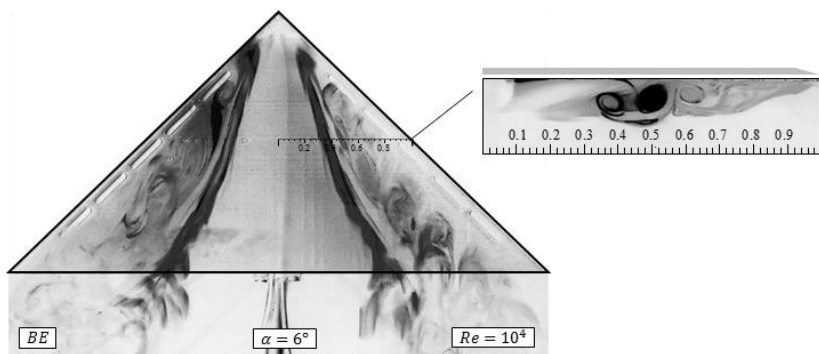
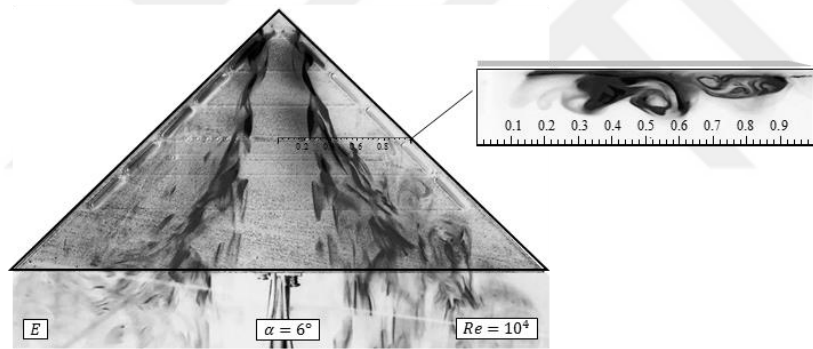
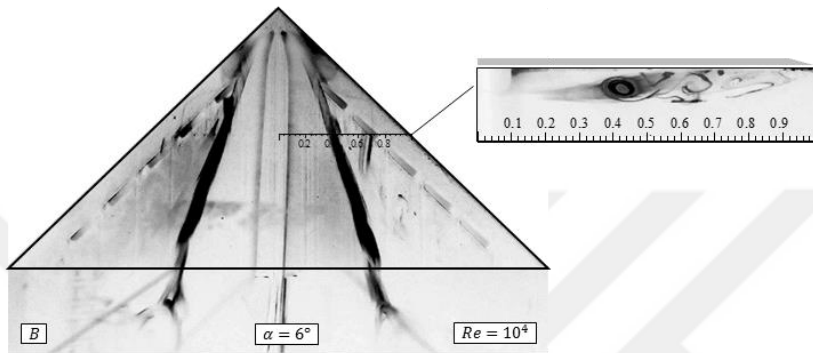
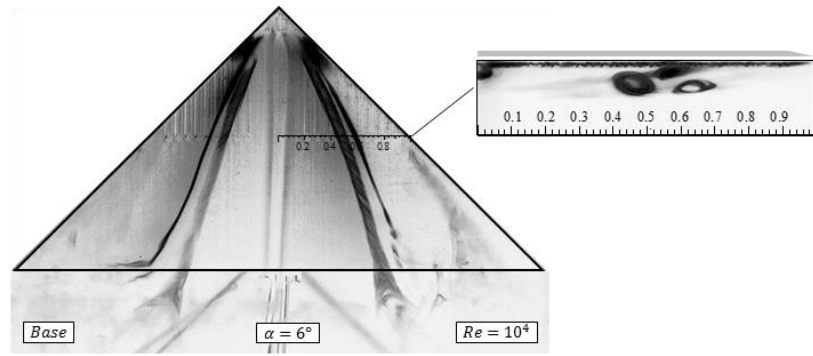


Figure 6-4 Surface -flow and half span cross -flow smoke visualizations for Base, B, E and BE planforms for $Re = 10^4$ at angle of attack $\alpha = 6^\circ$.

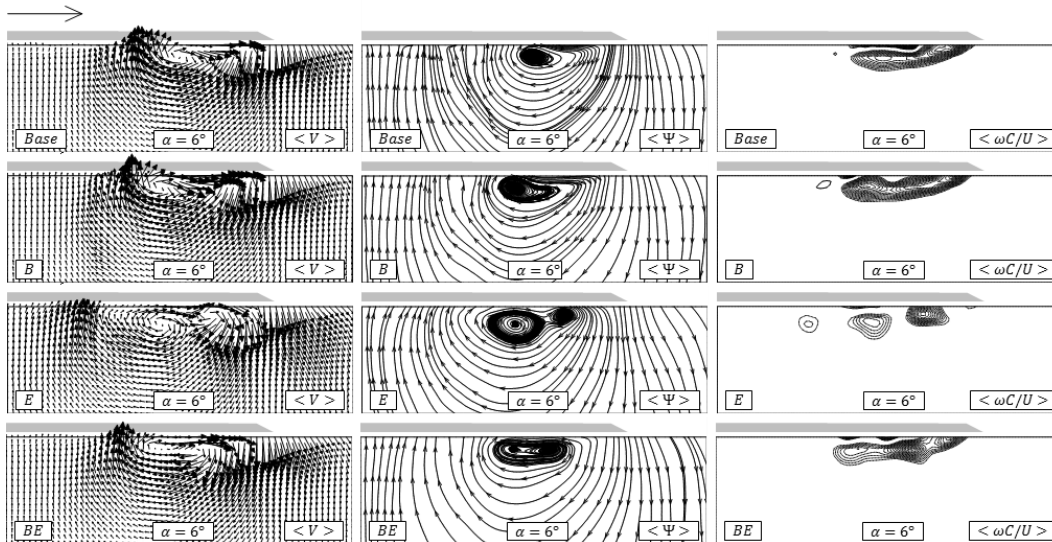


Figure 6-5 Patterns of time-averaged velocity vectors $\langle V \rangle$, streamlines $\langle \Psi \rangle$ and constant contours of non-dimensional axial vorticity $\langle \omega C/U \rangle$ at angle of attack $\alpha = 6$ deg for $Re = 10^5$: $[|\langle \omega C/U \rangle|]_{min} = 7$, $\Delta[|\langle \omega C/U \rangle|] = 2$

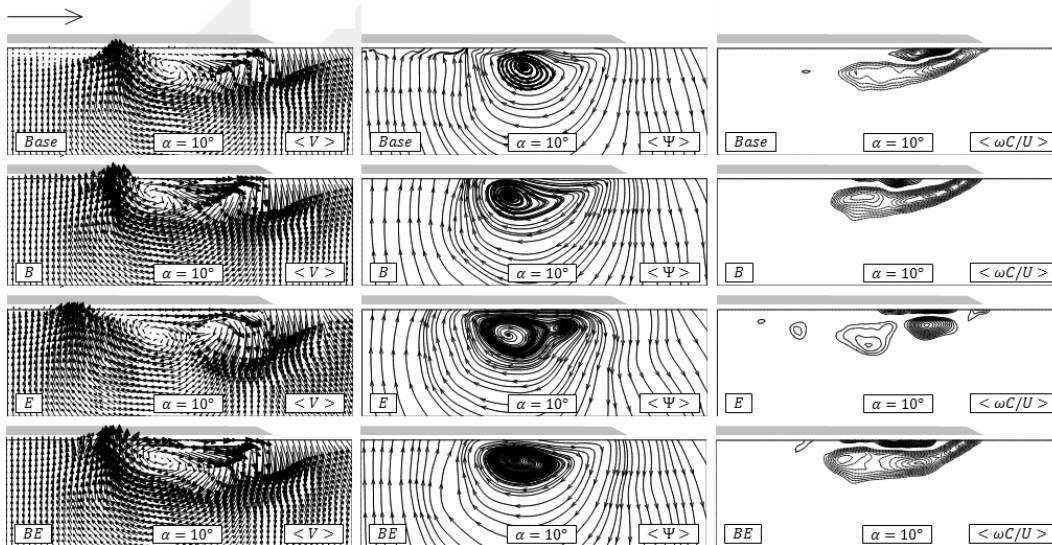


Figure 6-6 Patterns of time-averaged velocity vectors $\langle V \rangle$, streamlines $\langle \Psi \rangle$ and constant contours of non-dimensional axial vorticity $\langle \omega C/U \rangle$ at angle of attack $\alpha = 10$ deg for $Re = 10^5$: $[|\langle \omega C/U \rangle|]_{min} = 7$, $\Delta[|\langle \omega C/U \rangle|] = 2$

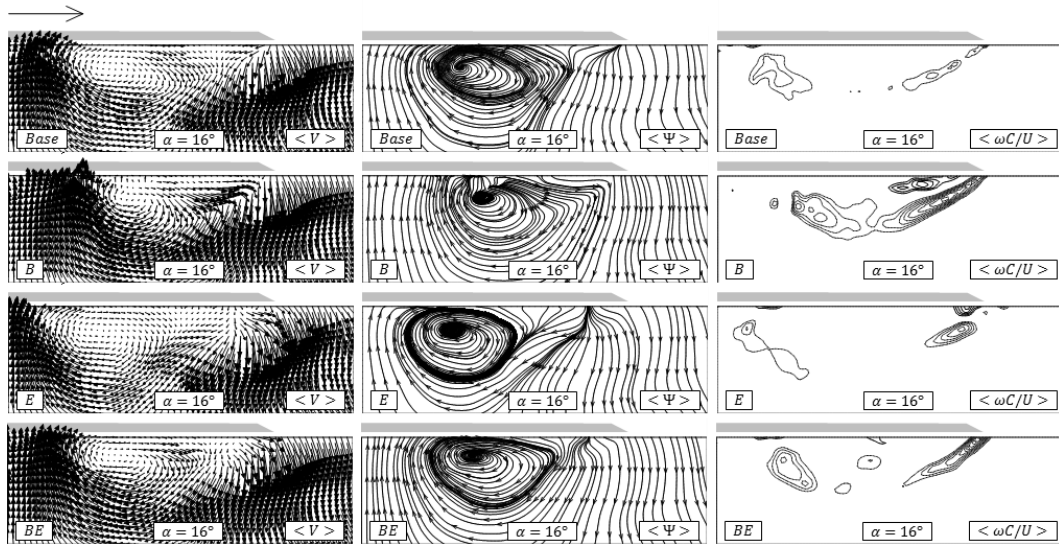


Figure 6-7 Patterns of time-averaged velocity vectors $\langle V \rangle$, streamlines $\langle \Psi \rangle$ and constant contours of non-dimensional axial vorticity $\langle \omega C/U \rangle$ at angle of attack $\alpha = 16$ deg for $Re = 10^5$: $[\langle \omega C/U \rangle]_{min} = 7$, $\Delta[\langle \omega C/U \rangle] = 2$

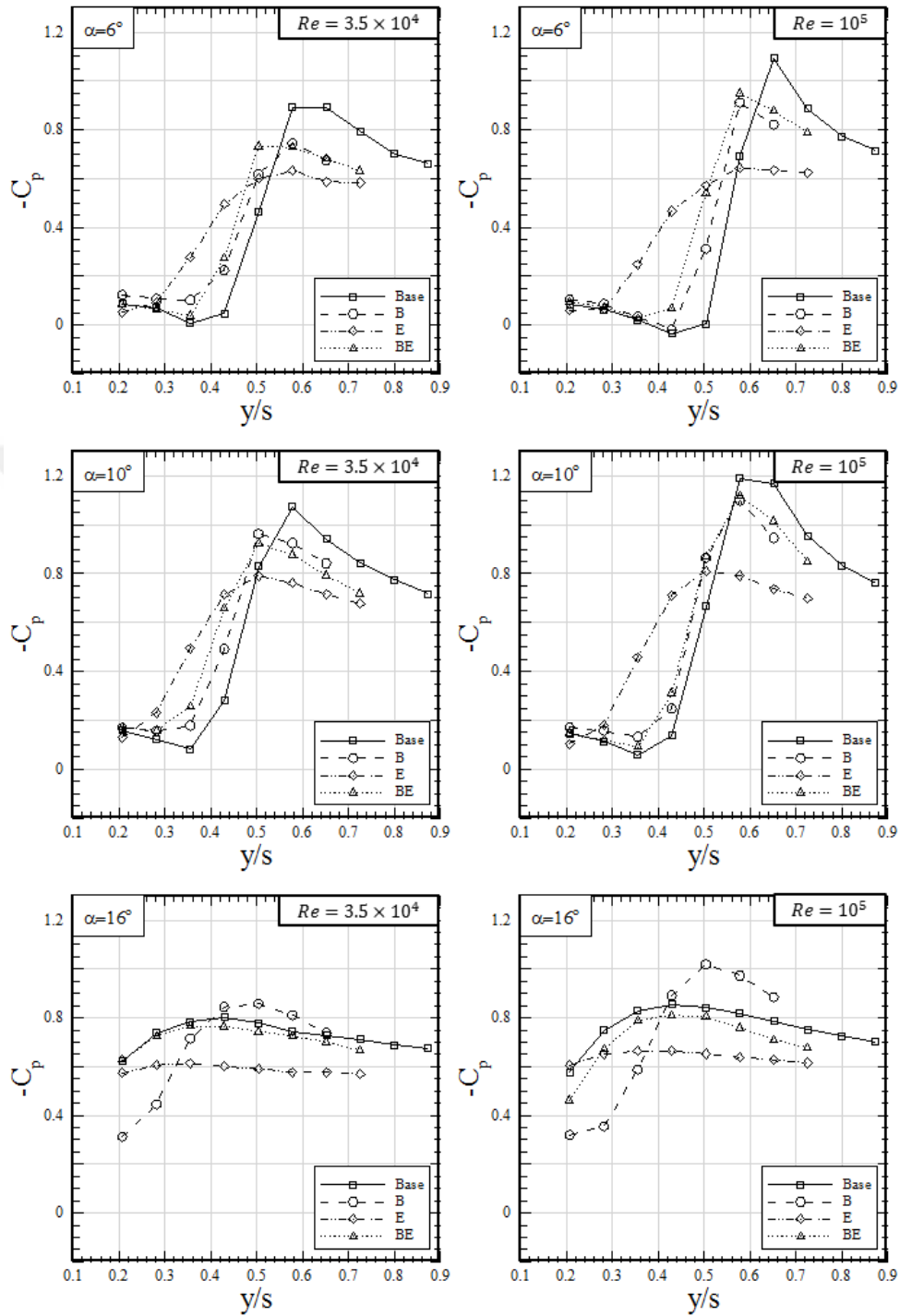


Figure 6-8 $-C_p$ distributions of half span Base, B, E and BE planforms at angle of attacks $\alpha = 6, 10$ and 16 deg at $Re = 3.5 \times 10^4$ (left) and $Re = 10^5$ (right).

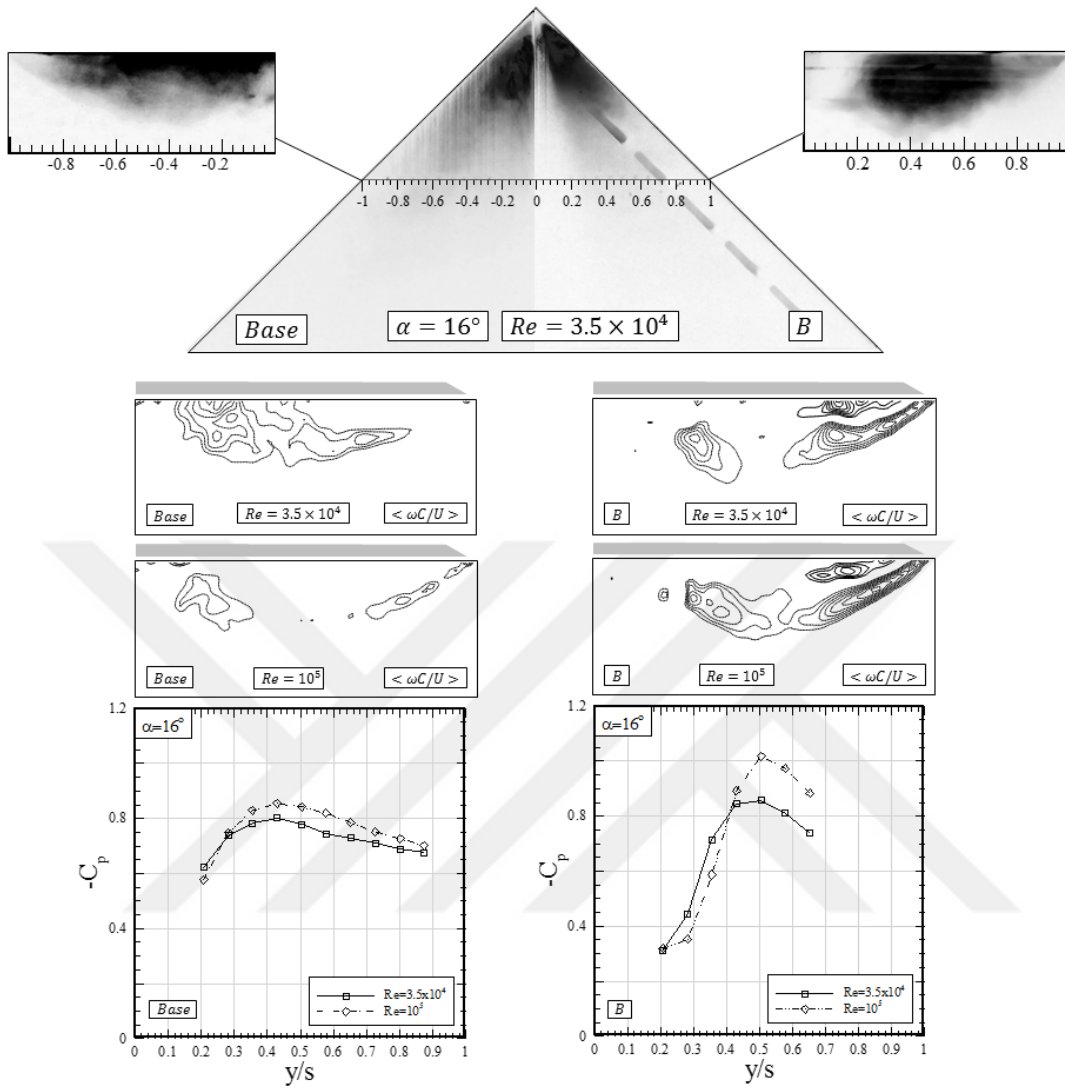


Figure 6-9 Comparison of surface and cross flow smoke visualizations at $Re = 3.5 \times 10^4$ with constant contours of non-dimensional axial vorticity patterns $\langle \omega C/U \rangle$ and $-C_p$ distribution at $Re = 3.5 \times 10^4$ and $Re = 10^5$ for Base (left) and B (right) planforms. $[\langle \omega C/U \rangle]_{min} = 7$, $\Delta[\langle \omega C/U \rangle] = 2$

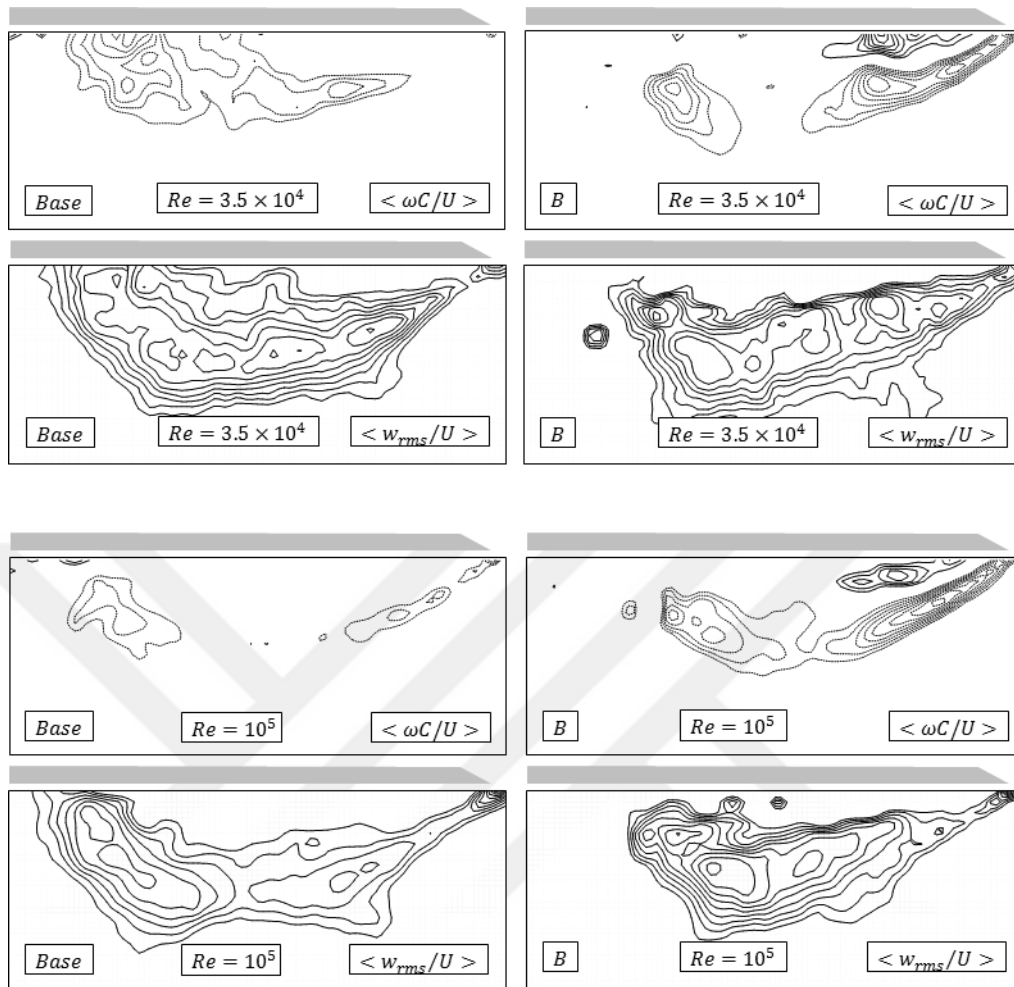


Figure 6-10 Patterns of constant contours of non-dimensional axial vorticity $\langle \omega C/U \rangle$ ($[|\langle \omega C/U \rangle|]_{min} = 7$, $\Delta[|\langle \omega C/U \rangle|] = 2$) and constant contours of non-dimensional root mean square of vertical velocity w_{rms}/U ($[w_{rms}/U]_{min} = 0.08$, $\Delta[w_{rms}/U] = 0.015$) at $Re = 3.5 \times 10^4$ and $Re = 10^5$ for Base and B planforms for attack angle $\alpha = 16$ deg.

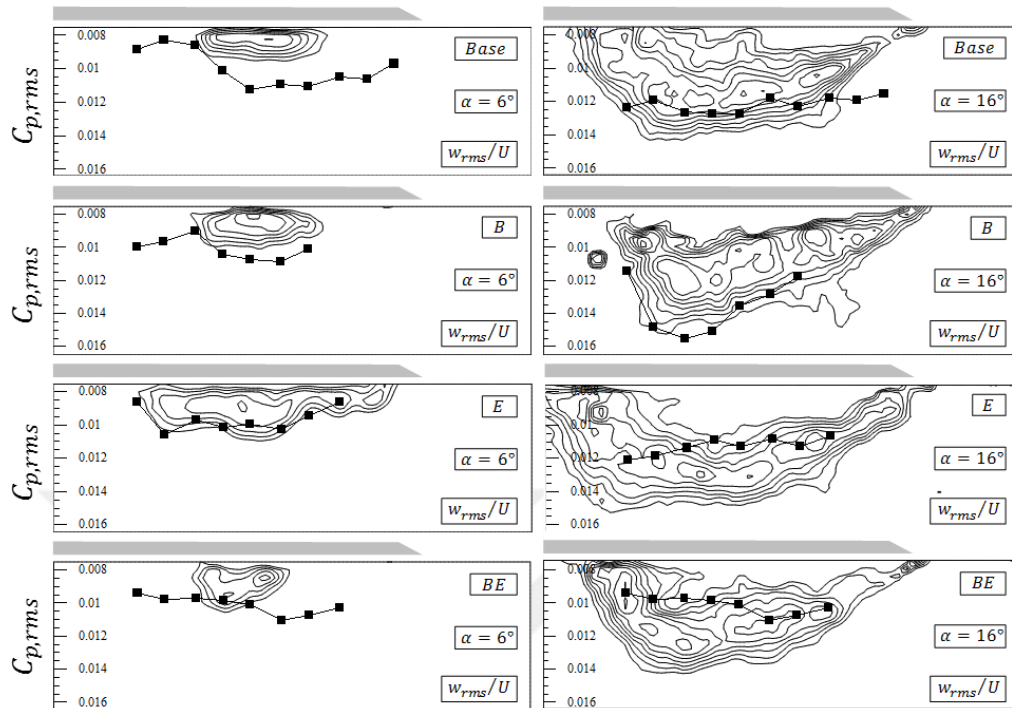


Figure 6-11 Patterns of constant contours of non-dimensional root mean square of vertical velocity w_{rms}/U ($[w_{rms}/U]_{min} = 0.08$, $\Delta[w_{rms}/U] = 0.015$) and non-dimensional root mean square of pressure fluctuations $C_{p,rms}$ for Base, B, E and BE planforms at $Re = 3.5 \times 10^4$ for attack angles $\alpha = 6$ deg and $\alpha = 16$ deg.

CHAPTER 7

EFFECT OF FLEXION RATIO ON FLOW STRUCTURE OVER A NONSLENDER DELTA WING

This chapter presents the results of a bio-inspired passive flow control method, flexion ratio concept, over a 45 deg swept delta wing. In a recent research [98], it is revealed that natural flyers and swimmers exhibit similar bending patterns for their propulsors. The ratio of rigid part length, a , to the propulsors length, S , have a fixed value around 0.7 being independent from the medium of motion or scale of the organism[98]. In this study, it was aimed to apply the same rule on a nonslender delta wing geometry and investigated its effect on flow structures over the planform. To better understand relative effect of a to S ratio, planforms having the ratio of $a/S = 0.7, 0.5$ and 0.3 were produced along with a rigid Base planform. The cross-flow PIV experiments were conducted at $x/C = 0.5$, for a broad range of angle of attacks $8 < \alpha < 30$ deg and Reynolds numbers $10^4 < Re < 10^5$.

7.1 The Effect of Flexion Ratio on Flow Structure at $Re = 10^5$

The effects of flexion ratio on flow structures of 45 deg sweep delta wing were characterized on a planform of $a/S = 0.7$, along with the Base planform at $Re = 10^5$ using PIV at chordwise distance of $x/C = 0.5$. Figures 7-1, 7-2 and 7-3 demonstrate the cross-flow PIV results for the attack angles $\alpha = 12, 24$ and 30 deg, respectively. The figures are constructed using the same approach, where each row represents the time-averaged velocity vectors $\langle V \rangle$, the time-averaged streamline patterns $\langle \Psi \rangle$, and the contours of constant axial non-dimensional vorticity patterns $\langle \omega C/U \rangle$ for the Base and $a/S = 0.7$ planform on right and

left of the figure, respectively. The contours of constant axial non-dimensional vorticity $\langle \omega C/U \rangle$ are illustrated such that solid (dark) and dashed (light) lines indicate, respectively, positive and negative contours, in which the positive orientation corresponds to axial vorticity in the direction of the outward normal. The constant contours of non-dimensional axial vorticity values are set same for all attack angles with absolute minimum and absolute incremental values of 7 and 2 respectively ($[(\omega C/U)]_{min} = 7$ and $[\Delta(\omega C/U)] = 2$). The constant contours of root-mean square of vertical velocity fluctuation values are set same for all attack angles with absolute minimum and absolute incremental values of 0.08 and 0.015 respectively ($[w_{rms}/U]_{min} = 0.08$, $\Delta[w_{rms}/U] = 0.015$).

Fig 7-1 represents the results at attack angle $\alpha = 12$ deg for $Re = 10^5$. Velocity vectors and corresponding streamline patters of Base planform indicate that, the flow separates from the leading edge and attaches to planform at a half way distance to the leading edge from planform symmetry line. The non-dimensional vorticity patters do not have a concentrated pattern, which means that there is no foot print of coherent vortical patterns on the planform. The patterns of time-averaged streamline, velocity vectors, and vorticity contours clearly indicate that modifying wing geometry with $a/S = 0.7$ leads no significant change in flow structures over the planform. Moreover, considering the results at attack angles $\alpha = 24$ and 30 deg, in Figures 7-2 and Figure 7-3, similar results are observed. At attack angle $\alpha = 24$, the velocity vectors and the corresponding streamlines indicate that the flow reattaches to planform in the vicinity of wing symmetry line, which is a clear indication of fully separated flow over the planform. The streamline patterns show no swirling pattern. The corresponding non-dimensional axial vorticity patterns support this observation with a nearly vanished vorticity pattern. At attack angle $\alpha = 30$ deg, the reattachment location of the separated flow is on the symmetry line and quite away from the surface, which may be interpreted as a stalled flow. The streamline patterns form small scale symmetric swirl pattern above the planform on symmetry line axis.

7.2 The Effect of Flexion Ratio on Flow Structure at $Re = 2 \times 10^4$

Further cross-flow PIV experiments were conducted at chordwise distance of $x/C = 0.5$ for the Reynolds number $Re = 2 \times 10^4$, and attack angles $\alpha = 8, 10, 12$ and 14 deg. Figures 7-4, 7-5 and 7-6 and 7-7 demonstrate the cross-flow PIV results for the attack angles $\alpha = 8, 10, 12$ and 14 deg, respectively. The figures are constructed using the same approach, where each row represents the time-averaged velocity vectors $\langle V \rangle$, the time-averaged streamline patterns $\langle \Psi \rangle$, and the contours of constant axial non-dimensional vorticity patterns $\langle \omega C/U \rangle$ for the Base and $a/S = 0.7$ planform on the right and the left of the corresponding figure, respectively. The constant contours of non-dimensional axial vorticity values are set same for all attack angles with absolute minimum and absolute incremental values of 8 and 4, respectively ($[(\omega C/U)]_{min} = 8$ and $[\Delta](\omega C/U)] = 4$).

The corresponding cross-flow patterns for the attack angle $\alpha = 8$ deg are demonstrated in Figure 7-4. Considering the flow patterns on Base planform indicated on the left column, the separated shear reattaches the surface in the vicinity of symmetry line of the wing planform. The vorticity patterns, emanating from the leading edge weakly attaches to surface with apparent concentration, which may be interpreted as footprint of coherent vortical patterns on planform. Moreover time-averaged streamline patterns indicate a dual vortex structure. However, planform $a/S = 0.7$, shows slightly different flow structures. The magnitude of the velocity vectors are smaller, and the spatial extent of the swirl structure is larger compared to Base wing planform, and the streamline patterns show a single focal point. Moreover, the peak value of the maximum vorticity contour in $a/S = 0.7$ planform is slightly higher compared to Base planform.

Figure 7-5 presents the cross-flow PIV results at attack angle $\alpha = 10$ deg. The reattachment location slightly moves inboard, and the spatial extent of the swirl

pattern expands on Base planform compared to $\alpha = 8$ deg. The time averaged streamline patterns have two focal points, which may be an indication of dual vortex structure. On $a/S = 0.7$ planform on the right hand-side of Figure 7-5, the vector field and the vorticity patterns are significantly different compared to Base planform. The peak vorticity value increases over 100 % on left and over 50% on right vorticity concentration. The time-averaged streamlines, however, have single focus and demonstrates a single large scale flow pattern.

Figure 7-6 demonstrates the corresponding cross-flow PIV results at attack angle $\alpha = 12$ deg. Both planforms have quite similar flow patterns. The swirl pattern on planforms expands spatially. Although the time-averaged streamline patterns show different structures, it might be due to mathematical interpretation of vector field. The non-dimensional contours of axial vorticity patterns have no concentrated regions, which may be interpreted as lack of coherent vortical structures. However, the peak values of vorticity concentration regions are 50% higher on $a/S = 0.7$ planform compared to Base planform.

Cross-flow PIV results for attack angle $\alpha = 14$ deg is presented in Figure 7-7. It is evident that the aforementioned discussions of the result for the angle of attack $\alpha = 12$ deg shown in Figure 7-6 are completely valid for this case. The focus of the swirl pattern slightly moves inboard and expands spatially. The peak value of the vorticity concentration increases around 80% on $a/S = 0.7$ planform compared to Base planform without any indication of coherent vortical structure, which means that although the material modification affects the flow structures favorably, the recovery of the vortical structures couldn't be succeeded.

7.3 The Effect of Flexion Ratio on Flow Structure at $Re = 10^4$

PIV experiments at chordwise distance of $x/C = 0.5$, at $Re = 10^4$ for attack angle $\alpha = 12$ deg are conducted for planforms with different flexion ratios,

$a/S = 0.7, 0.5$ and 0.3 to understand the effect of modifying edges of planform at different flexion ratios at low Reynolds number flows. Figure 7-8 is constructed such that each row represents planforms Base, $a/S = 0.7$, $a/S = 0.5$ and $a/S = 0.3$ from top to bottom respectively. The time-averaged velocity vectors $\langle V \rangle$, the time-averaged streamline patterns $\langle \Psi \rangle$, and the contours of constant axial non-dimensional vorticity patterns $\langle \omega C/U \rangle$ for the Base, $a/S = 0.7$, $a/S = 0.5$ and $a/S = 0.3$ planforms are presented from left to right, respectively. The constant contours of non-dimensional axial vorticity values are set same for all attack angles with absolute minimum and absolute incremental values of 5 and 5 respectively ($[(\omega C/U)]_{min} = 5$ and $[\Delta(\omega C/U)] = 5$).

Considering the whole figure, flexion ratio at $Re = 10^4$ seems to be effective in terms of altering the flow field over the planform. The vector field over the Base planform demonstrates that the flow separated from the leading edge, reattaches to planform surface near symmetry plane of the planform, leading a weak reattachment as supported by non-dimensional contours of axial vorticity patters. On $a/S = 0.7$ planform the reattachment location apparently moves towards leading edge with a stronger reattachment, increasing the peak value of vorticity concentration 33%. The spatial extent of the swirl patterns grow compared to Base planform. Planform $a/S = 0.5$ has very similar flow structures with planform $a/S = 0.7$. The reattachment location is slightly moved outwards compared to $a/S = 0.7$ planform and the peak value of vorticity concentration is 66% higher compared to Base planform. Planform $a/S = 0.3$ has a very similar flow field over the planform with Base planform. The reattachment location of the flow is slightly outboard compared to Base planform, with similar vorticity concentration values.

7.4 Additional Discussion on the Results of Flexion Ratio Study

The results and the interpretation of the results of this chapter need more discussion due to several reasons. The main idea of the study was to create a wing planform, which would respond immediately to flow. However, the wing planforms manufactured, even with $50\mu m$ thickness stainless steel did not respond to flow field as expected. At high Reynolds number, i.e., $Re = 10^5$, the wing was deflected and a very low frequency flapping was observed. At lower free stream velocities, i.e. $Re = 10^4$ and $Re = 2 \times 10^4$, the wing deflected barely and small scale oscillations were observed. The deflection modes of the wing are illustrated in a sketch in Figure 7-9. Moreover, the possible effect of thickness differences between the base planform and modified planforms may also lead differences in flow field. Hence, it is important to choose the correct comparison case or cases according to wing response we obtain.

One of the major study that should be considered for discussion and comparison is the study of Taylor et al, who studied lift enhancement by flexible wings over non-slender delta wings[34]. They showed that flexible delta wings delay the stall angle and increase lift force coefficient at post-stall region. Moreover, they concluded that this enhancement occurs only on full wings since they claim that the improvement in aerodynamic characteristics is related to physical phenomenon second-mode asymmetric oscillations of the planform. Since the half wing planforms do not show a second-mode asymmetric oscillations, there should be no improvement in terms of aerodynamic characteristics. For the experiments conducted in this study, the flexible parts laid on both leading edge and the region in-between was rigid. Hence it was not possible to obtain second mode asymmetric oscillation, and this might be the reason for not observing any significant effect at high Re numbers.

Moreover, Cai et al studied [110] leading-edge vortex flaps, which may be used as a comparison case for highly deflected cases of present study, and showed that upward deflected vortex flaps improve lift coefficients at low angle of attack but decrease stall angle and maximum lift coefficient. For downward deflected flaps, poor performance was observed at low angle of attacks, however, stall angle delays and maximum lift coefficient increased. Figure 7-10 shows comparison of base wing to downward deflected flaps (upper row) and downward deflected flaps (bottom row). The deflections of the planforms in this study were upwards, and for $Re = 10^4$ and $Re = 2 \times 10^4$, they didn't flap or oscillate significantly. Although, the geometry was not as sharp as a flap geometry, the results may be compared to upward deflected flaps, where an increase in vorticity levels are expected. Hence the vorticity increase on moderate angle of attacks at $Re = 10^4$ and $Re = 2 \times 10^4$ in this study are well-in-line with the observations of Cai et al.

Yet, the most important parameter in this study was the quality of the response of the wing to flow field. Hence, the problems related to wing response should be improved for future studies. Figure 7-11 illustrates some of the flexible wing applications from literature. Most of the studies are conducted by wings manufactured from carbon/fiber epoxy rods with mylar sheets. Hence, planforms manufactured with above mentioned materials may lead better response to flow field.

7.5 Conclusion

The focus of the present study is to have the basic understanding on the effect of partially flexible wings, i.e. application of flexion ratio concept, on flow structure of a nonslender delta wing. For this purpose, the experiments were conducted in a low speed wind tunnel for a broad range of Reynolds numbers $10^4 \leq Re \leq 10^5$ and attack angles $8 \leq \alpha \leq 30$ deg using five different 45 deg swept delta wing including a base planform. Particle Image Velocimetry technique were employed

to characterize the flow field. The following main conclusions are drawn from the results of the present study:

- 1) For high Reynolds number, i.e. $Re = 10^5$ the application of flexion ratio does not alter the flow field even the wing planform experiences deflection over a wide range of angle attack $12 \leq \alpha \leq 30$ deg .
- 2) For relatively lower Reynolds numbers, i.e. $Re = 10^4$ and $Re = 2 \times 10^4$, at low angle of attacks, i.e., $\alpha \leq 12$, the application of flexion ratio alters the general flow structure slightly with significant increase in the level of vorticity concentrations.
- 3) Since the wing planforms manufactured did not response to flow medium as expected, no strong conclusions should be drawn on the effect of flexion ratio on the flow structure of nonslender delta wings and further investigations need to be carried out.

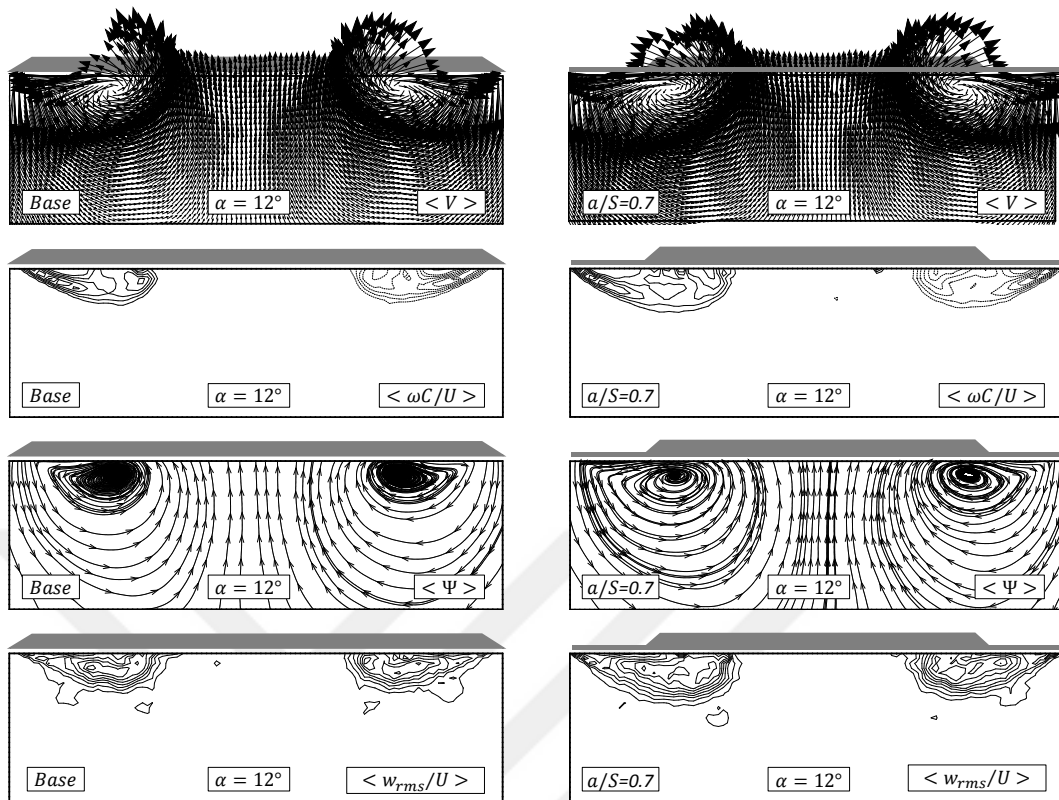


Figure 7-1 Patterns of time-averaged velocity vectors $\langle V \rangle$, streamlines $\langle \Psi \rangle$ and constant contours of non-dimensional axial vorticity $\langle \omega C/U \rangle$ and patterns of constant contours of non-dimensional root mean square of vertical velocity) at angle of attack $\alpha = 12$ deg for $Re = 10^5$: $[|\langle \omega C/U \rangle|]_{min} = 7$, $\Delta[|\langle \omega C/U \rangle|] = 2$, $[w_{rms}/U]_{min} = 0.08$, $\Delta[w_{rms}/U] = 0.015$

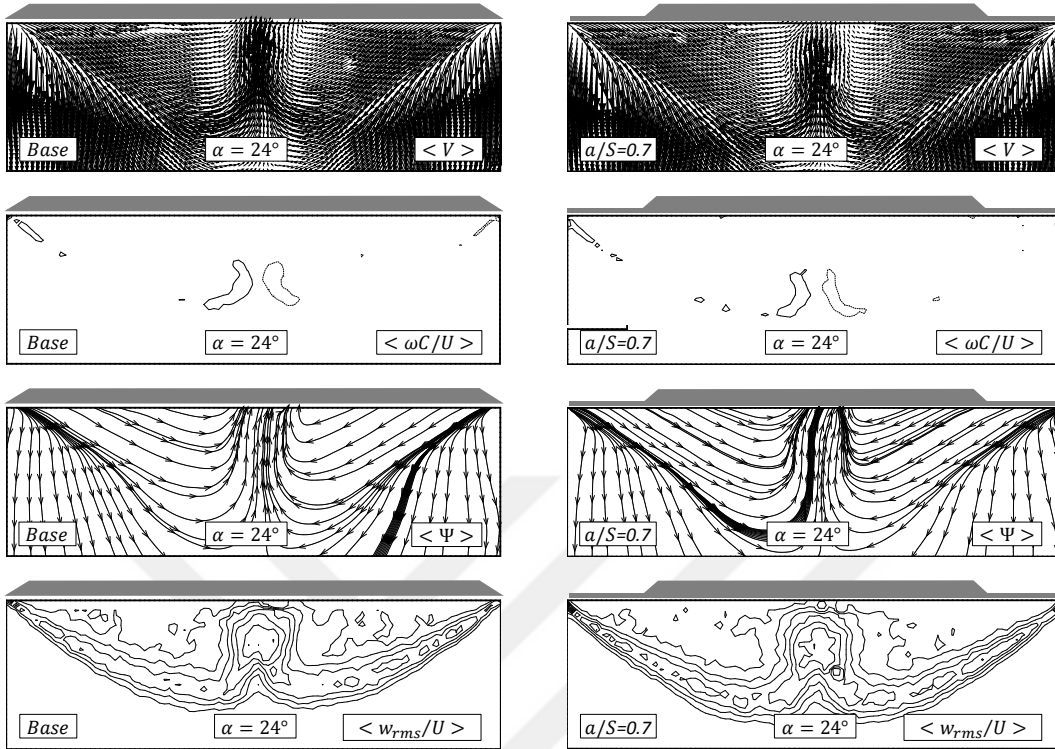


Figure 7-2 Patterns of time-averaged velocity vectors $\langle V \rangle$, streamlines $\langle \Psi \rangle$ and constant contours of non-dimensional axial vorticity $\langle \omega C/U \rangle$ and patterns of constant contours of non-dimensional root mean square of vertical velocity) at angle of attack $\alpha = 24$ deg for $Re = 10^5$: $[|\langle \omega C/U \rangle|]_{min} = 7$, $\Delta[|\langle \omega C/U \rangle|] = 2$, $[w_{rms}/U]_{min} = 0.08$, $\Delta[w_{rms}/U] = 0.015$

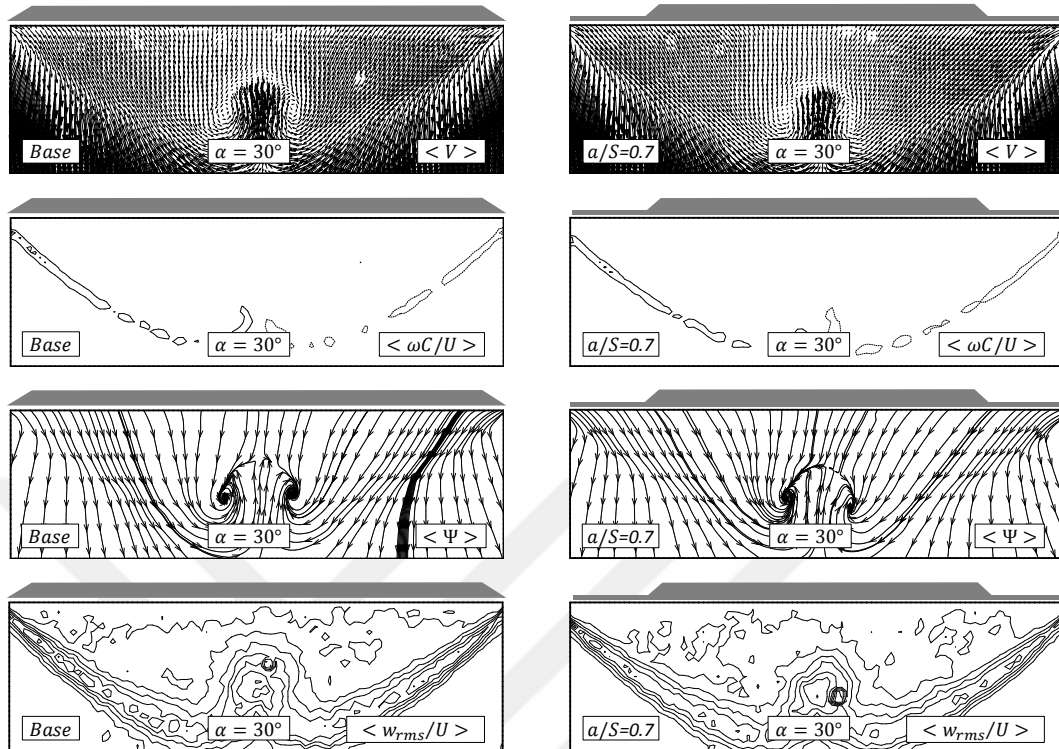


Figure 7-3 Patterns of time-averaged velocity vectors $\langle V \rangle$, streamlines $\langle \Psi \rangle$ and constant contours of non-dimensional axial vorticity $\langle \omega C/U \rangle$ and patterns of constant contours of non-dimensional root mean square of vertical velocity) at angle of attack $\alpha = 30$ deg for $Re = 10^5$: $[|\langle \omega C/U \rangle|]_{min} = 7$, $\Delta[|\langle \omega C/U \rangle|] = 2$, $[w_{rms}/U]_{min} = 0.08$, $\Delta[w_{rms}/U] = 0.015$

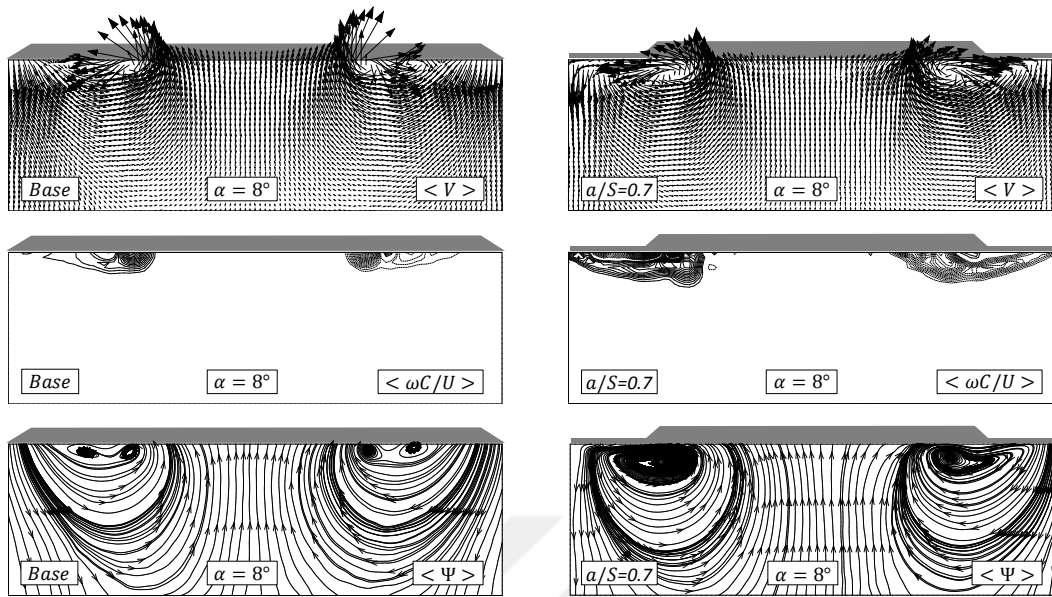


Figure 7-4 Patterns of time-averaged velocity vectors $\langle V \rangle$, streamlines $\langle \Psi \rangle$ and constant contours of non-dimensional axial vorticity $\langle \omega C/U \rangle$ at angle of attack $\alpha = 8$ deg for $Re = 2 \times 10^4$: $[\langle \omega C/U \rangle]_{min} = 8$, $\Delta[\langle \omega C/U \rangle] = 4$

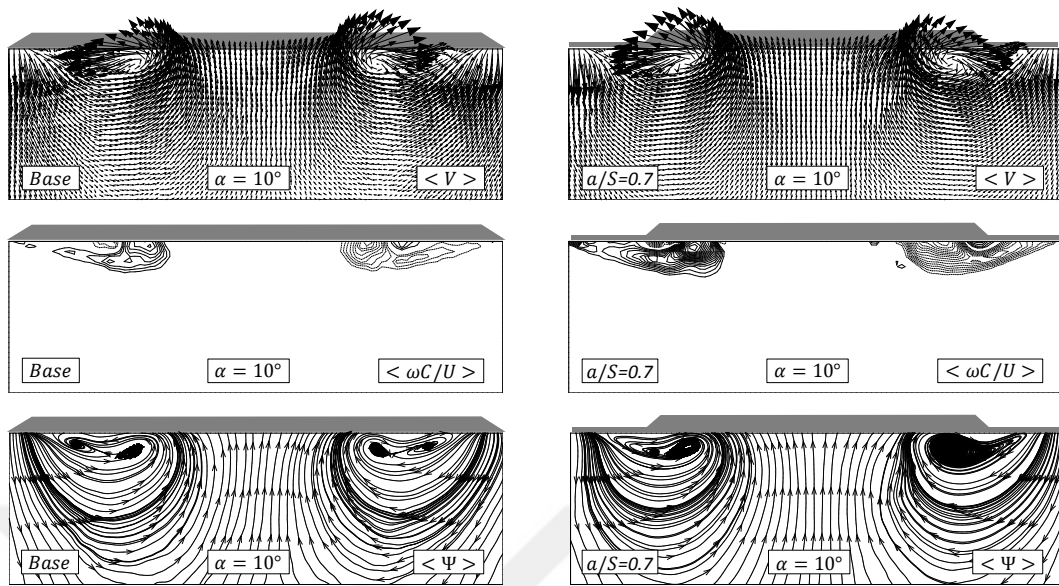


Figure 7-5 Patterns of time-averaged velocity vectors $\langle V \rangle$, streamlines $\langle \Psi \rangle$ and constant contours of non-dimensional axial vorticity $\langle \omega C/U \rangle$ at angle of attack $\alpha = 10$ deg for $Re = 2 \times 10^4$: $[|\langle \omega C/U \rangle|]_{min} = 8$, $\Delta[|\langle \omega C/U \rangle|] = 4$

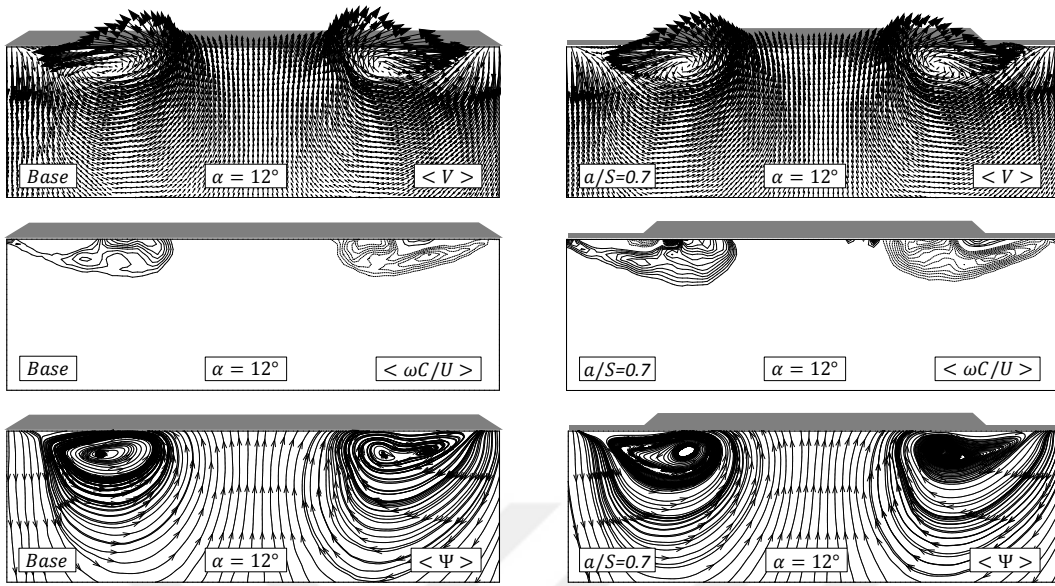


Figure 7-6 Patterns of time-averaged velocity vectors $\langle V \rangle$, streamlines $\langle \Psi \rangle$ and constant contours of non-dimensional axial vorticity $\langle \omega C/U \rangle$ at angle of attack $\alpha = 12$ deg for $Re = 2 \times 10^4$: $[\langle \omega C/U \rangle]_{min} = 8$, $\Delta[\langle \omega C/U \rangle] = 4$

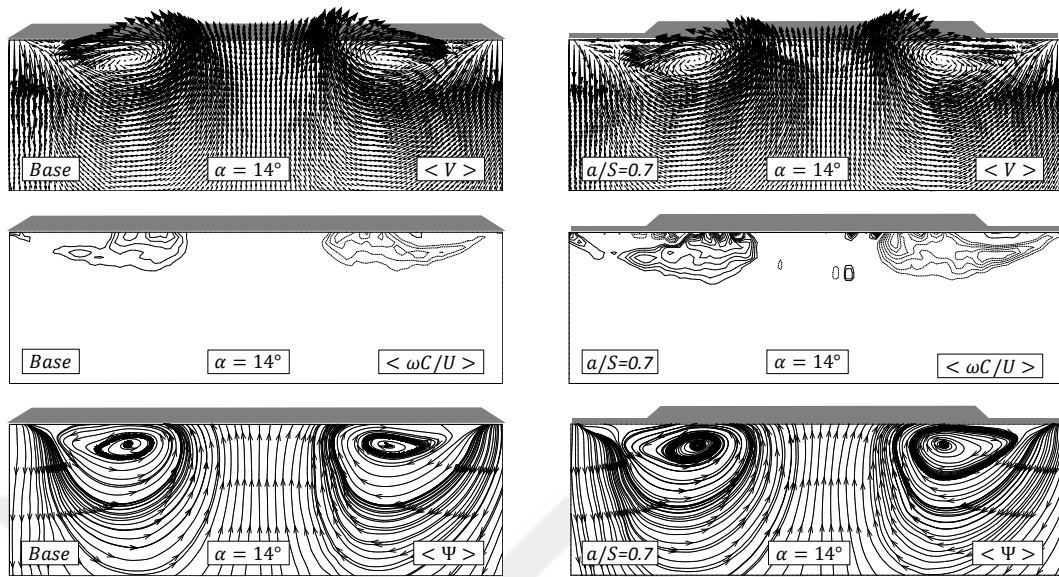


Figure 7-7 Patterns of time-averaged velocity vectors $\langle V \rangle$, streamlines $\langle \Psi \rangle$ and constant contours of non-dimensional axial vorticity $\langle \omega C/U \rangle$ at angle of attack $\alpha = 14$ deg for $Re = 2 \times 10^4$: $[\langle \omega C/U \rangle]_{min} = 8$, $\Delta[\langle \omega C/U \rangle] = 4$

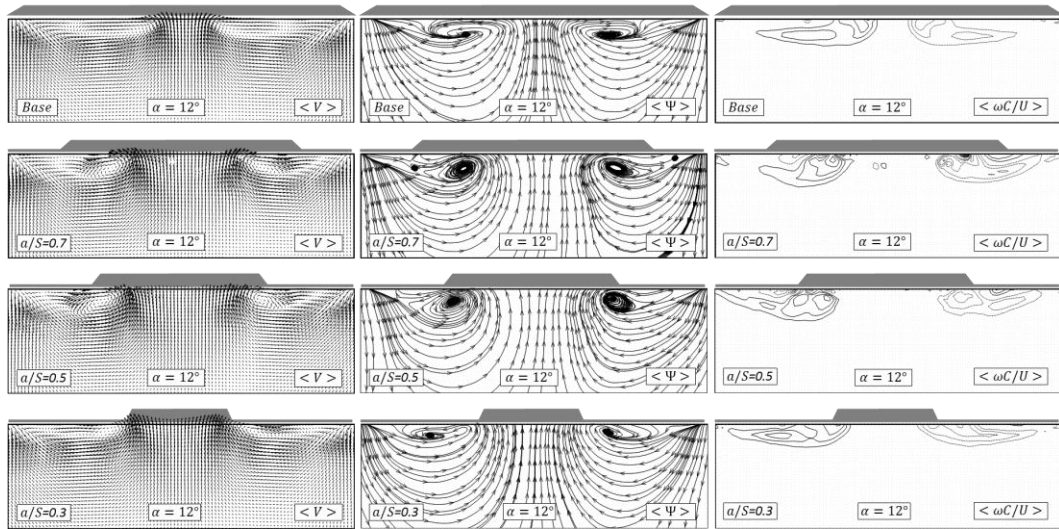


Figure 7-8 Patterns of time-averaged velocity vectors $\langle V \rangle$, streamlines $\langle \Psi \rangle$ and constant contours of non-dimensional axial vorticity $\langle \omega C/U \rangle$ at angle of attack $\alpha = 12$ deg for $Re = 10^4$: $[\langle \omega C/U \rangle]_{min} = 5$, $\Delta[\langle \omega C/U \rangle] = 5$

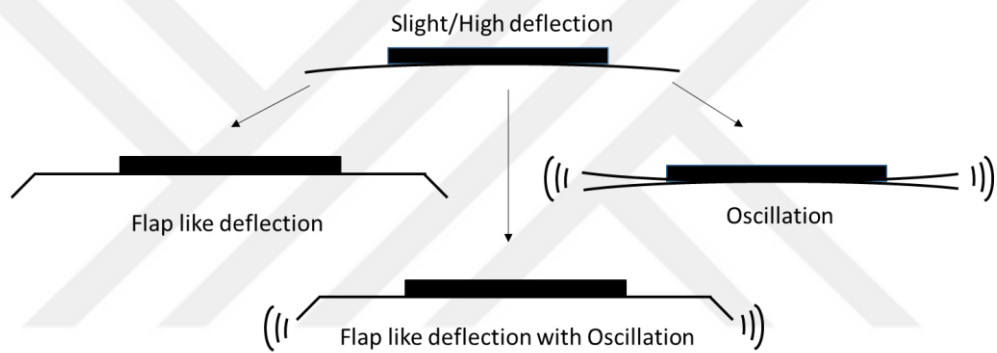
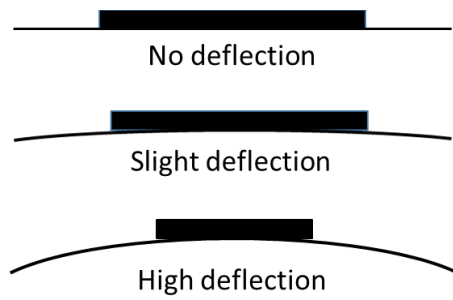


Figure 7-9 Deflection types encountered during experiments.

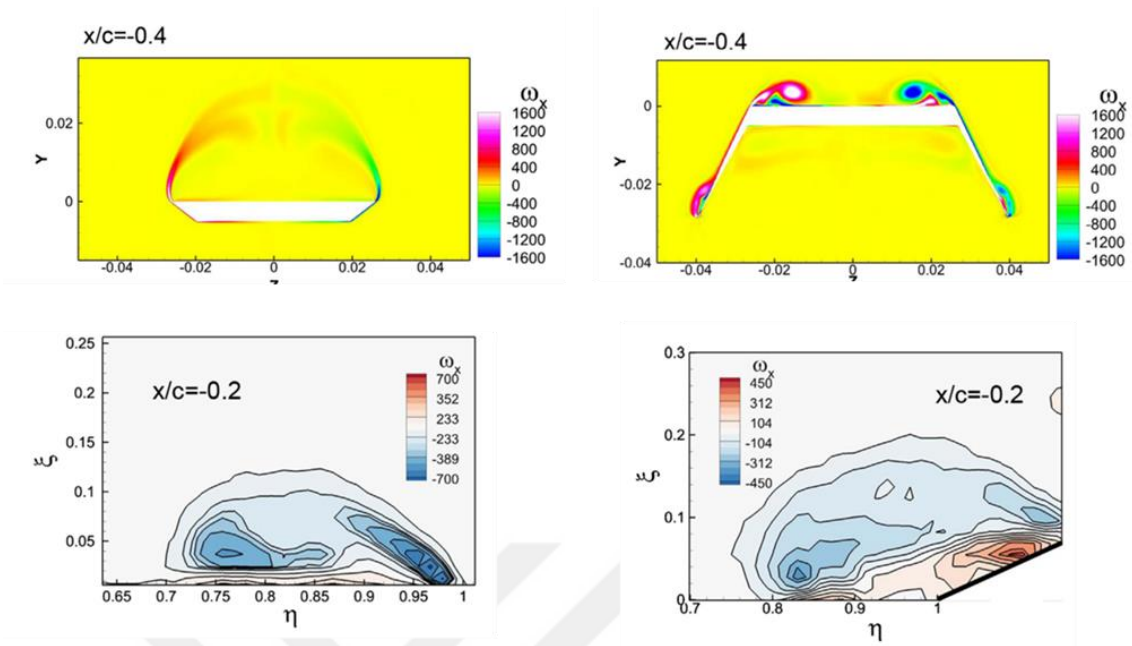


Figure 7-10 Comparison of vorticity levels of base platform to downward deflected flap (upper row) and upward deflected flap (bottom row) [110].

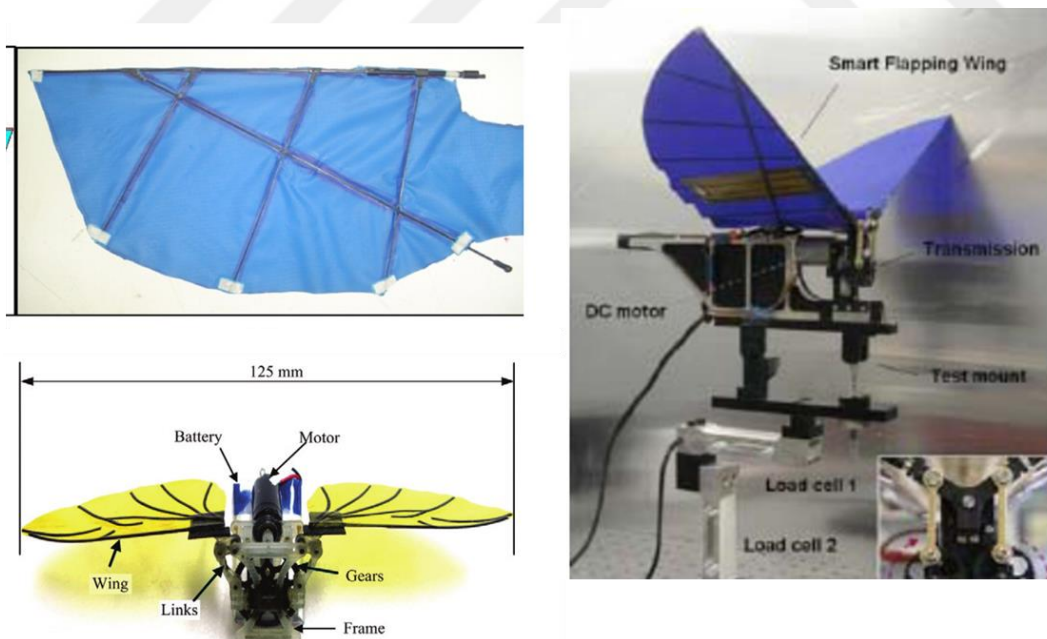


Figure 7-11 Wing with carbon-fiber epoxy rods [111].

CHAPTER 8

CONCLUSION

8.1 Summary and Conclusions

The present study has focused on developing and implementing novel passive flow control strategies to improve pre-to-post stall conditions on nonslender delta wings. Three different novel passive control strategies were developed and implemented which were namely, passive bleeding and bio-inspired modifications including edge modifications and flexibility application. The studies were conducted on 45 deg sweep delta wing for all three control methods. The effects of the performed control strategies were studied via laser-illuminated smoke visualization, unsteady pressure measurements and PIV. Specific experimental matrix and the measurement methods were determined for each control method. Experiments were conducted over a broad range of Reynolds numbers and attack angles for each study which falls into $4^\circ < \alpha < 30^\circ$ for attack angle and $10^4 < Re < 10^5$ for Reynolds number. Five different edge modifications, three different bleeding configurations, and three different partially flexible wings were tested and compared with the base wing.

Based on the results of the current study, the following general conclusions can be drawn:

- The laser illuminated smoke visualization experiments showed that the geometric modification of the leading edge and the trailing edge of a 45 deg swept delta wing based on biomimicking the fluke geometry of a white-sided dolphin is quite effective on altering the whole flow field over

the planform. Firstly, the leading edge and the trailing edge of the base planforms were modified to obtain a fluke like geometry. Then the modifications were performed separately in order to identify the possible effects of each edge. Experiments were conducted at attack angles $\alpha = 4, 6, 8, 10$ and 12 deg and Reynolds numbers $Re = 10^4, 1.5 \times 10^4, 2 \times 10^4$ and 2.5×10^4 . Contrary to expectations, Base planform performed better under all test conditions in terms of controlling three-dimensional surface separation and delaying stall. Moreover, trailing edge modifications are identified as the major contributor to deterioration the flow structures over the planform.

- Passive bleeding, directing the high-pressure air from the pressure side of the wing to suction side of the wing without any energy input to control the flow structures over a 45 deg nonslender delta wing was studied. Three different bleeding strategies were developed and investigated on a base planform via laser illuminated smoke visualization, unsteady pressure measurements and PIV. At high Reynolds numbers ($Re = 3.5 \times 10^4$ $Re = 10^5$), and high angle of attacks ($\alpha = 16$ deg), appropriate passive bleeding strategy is quite effective in terms of eradication of three-dimensional surface separation and delaying stall compared with planform without control. On the contrary, at low Reynolds numbers ($Re = 1 \times 10^4$) and low angle of attack ($\alpha = 6, 10$ deg), all the bleed strategies adversely affect the pressure distribution over the measurement plane, leading a lower $-C_p$ value with lower vorticity concentrations. Yet, laser illuminated flow visualization experiments showed that appropriate bleed strategy may lead a delay in vortex breakdown location even it is beyond the trailing edge. To conclude, the results confirm that the passive bleeding might effectively be used to eliminate the surface separation on nonslender delta wings with proper configuration.

- Application of flexion ratio, the ratio of the length of the rigid part to the length of the semi-span of a planform, on a 45 deg swept nonslender delta wing was investigated as a flow control strategy via PIV for a broad range of angle of attack and Reynolds numbers. The results of the present study showed that flexion ratio of $a/S = 0.7$ might be effective in terms of altering flow structures over nonslender delta wings at low Re numbers ($Re = 10^4$ and $Re = 2 \times 10^4$). The peak vorticity levels increase at a significant level and the velocity vector fields change significantly. On the contrary, at high Reynolds numbers ($Re = 10^5$), the flow structures showed no significant change on controlled planform compared to base planform. Moreover, the experiments conducted at $Re = 10^4$ showed that decreasing the flexion ratio (increasing the flexible part) affected the flow structures adversely. However, the interpretation of the results in this investigation might be misleading due to inadequate response of the flexible parts of the wing to the flow field. The improvements observed might be resulted from the thickness variations. Yet, for the current set of applications, flexion ratio application affects the flow field over the planform favorably at low Reynolds numbers at low angle of attacks, and had no significant result for high Reynolds numbers.

8.2 Recommendations for Future Work

The present investigation proposed, developed and implemented novel passive strategies for flow control over nonslender delta wings. Since the majority of the applications were novel, most of the effort in this thesis was devoted to understand the major effects of the performed control strategy and the physical reasons behind these effects. The strategies tested in the current study have great potentials for further improvements, optimizations and applications.

Below are the possible further investigation topics based on the results of this research:

- Before all, the experiments conducted in this thesis are based on pressure measurements, laser-illuminated flow visualization and PIV. Although the effects of performed flow control strategies can be characterized, their effect on aerodynamics forces are missing. Force measurements for all the conducted experiments in this study would help to understand the aerodynamic effects of the applied control strategies thoroughly.
- The edge modification experiments based on mimicking the geometry of a white-sided dolphin yielded unexpected results with a deterioration of flow structures over the planform. The physical differences of a dolphin fluke from bio-inspired delta wing geometry such as lateral and transverse flexibility, cross-section geometry, lateral and transverse thickness variation, and surface roughness are among the parameters that should be considered for future studies. Moreover, the sole effect of geometry modification based on white-sided dolphin turns out to be unsuccessful considering the stall performance for studied cases, however, its effect on unsteady cases such as pitching or rolling, which are commonly experienced in nature, should also be studied. One another parameter that may be effective and may be a topic of possible research is the effect of tail on fluke aero/hydrodynamics. Literature involves studies of intervening the flow field from the apex of the wing. Hence, designing the fore of the planform considering the studies in literature and tail-fluke relationship is another issue to be studied.
- To the best of authors' knowledge, this is the first study for application of passive bleeding on nonslender delta wings. Hence there is an enormous

unexplored territory to be studied in this field. Even only the optimization of the hole locations, hole shapes and hole angles may require a vast amount of study. Passive bleeding transforms the flow structures over the planform in a quite unique way. For low angle of attacks, multiple vortical structures are observed accompanying with a loss in suction pressure. Since the potential of altering the flow field is extremely high, unexpected results may be obtained for unsteady conditions such as pitching and rolling. Moreover, not only passive bleeding, but passive porosity, which is studied in literature for flow control applications, may also be a possible research topic for flow control over slender and nonslender delta wings.

- To the best of authors' knowledge this is the first study involving application of flexion ratio concept on nonslender delta wings as a flow control method. Since the response of the wing was unsatisfactory, the wing response to the flow field should be increased. One of the alternative method is using carbon/epoxy rods and mylar to manufacture flexible wings. Moreover, a deflected rigid planform at maximum flexion angle may be manufactured to study the sole effect of shape change, which is the result of maximum response of flexible wing to fluid medium, disregarding the effects of flapping.



REFERENCES

- [1] Earnshaw, P. B., Lawford, J. A., “Low-Speed Wind-Tunnel Experiments on a Series of Sharp-Edged Delta Wings,” Ministry of Aviation Aeronautical research Council Reports and Memoranda 3424, London, 1966.
- [2] Gad-El-Hak, M., Blackwelder, R. F., “The Discrete Vortices from a Delta Wing,” *AIAA Journal*, Vol. 23, no. 6, pp. 961–962, 1985.
- [3] Gursul, I., Gordnier, R., Visbal, M. , “Unsteady Aerodynamics of Nonslender Delta Wings,” *Progress in Aerospace Sciences*, Vol. 41, no. 7, pp. 515–557, Oct. 2005.
- [4] Gursul, I., Taylor, G., Wooding, C., “Vortex Flows over Fixed-Wing Micro Air Vehicles,” *40th AIAA Aerospace Sciences Meeting & Exhibit*, Reno, January, 2002.
- [5] Gordnier, R. E., Visbal, M. R., “Compact Difference Scheme Applied to Simulation of Low-Sweep Delta Wing Flow.,” *AIAA Journal*, Vol. 43, no. 8, pp. 1744–1752, Aug. 2005.
- [6] Gursul, I., Wang, Z., Vardaki, E., “Review Of Flow Control Mechanisms of Leading-Edge Vortices,” *Progress in Aerospace Sciences*, Vol. 43, no. 7–8, pp. 246–270, Oct. 2007.
- [7] Yavuz, M. M., Elkhoury, M., Rockwell, D., “Near-Surface Topology and Flow Structure on a Delta Wing,” *AIAA Journal.*, Vol. 42, no. 2, pp. 332–340, 2004.
- [8] Goruney, T., Rockwell, D., “Effect of Pitch Rate on Near-Surface

- Topology on a Delta Wing,” *AIAA Journal.*, Vol. 48, no. 6, pp. 1207–1220, 2010.
- [9] Wang, J., Zuo, L. X., Feng, L. H., “Influence of Reynolds Number on Vortex Flow over a Non-slender Delta Wing,” *AIAA Journal*, Vol. 48, no. 12, pp. 2831–2839, Dec. 2010.
- [10] Verhaagen, N. G., “Leading-Edge Radius Effects on Aerodynamic Characteristics of 50-Degree Delta Wings,” *Journal of Aircraft*, Vol. 49, no. 2, pp. 521–531, Mar. 2012.
- [11] Sahin, B., Yayla, S., Canpolat, C., Akilli, H., “Flow Structure over the Yawed Nonslender Diamond Wing,” *Aerospace Science and Technology*, Vol. 23, no. 1, pp. 108–119, Dec. 2012.
- [12] Çelik, A., Yavuz, M. M., “Effect of Edge Modifications on Flow Structure of Low Swept Delta Wing,” *AIAA Journal*, Vol. 54, no. 5, pp. 1789–1797, 2016.
- [13] Yayla, S., Canpolat, C., Sahin, B., Akilli, H., “Yaw Angle Effect on Flow Structure over the Nonslender Diamond Wing,” *AIAA Journal*, Vol. 48, no. 10, pp. 2457–2461, Oct. 2010.
- [14] Yavuz, M. M., “Transformation of Flow Structure on a Delta Wing of Moderate Sweep Angle During Pitch-Up Maneuver,” *Journal of Fluids and Structures*, Vol. 33, pp. 59–69, Aug. 2012.
- [15] Gursul, I., “Review of Unsteady Vortex Flows over Slender Delta Wings,” *Journal of Aircraft*, Vol. 42, no. 2, pp. 299–319, 2003.
- [16] Taylor, G. S., Gursul, I., “Buffeting Flows over a Low-Sweep Delta Wing,”

AIAA Journal, Vol. 42, no. 9, pp. 1737–1745, 2004.

- [17] Polhamus, E. C., “Predictions of Vortex-Lift Characteristics by a Leading-Edge Suction Analogy,” *Journal of Aircraft*, no. 4, pp. 193–199, 1971.
- [18] Payne, F. M., Ng, T. T., Nelson, R. C., Schiff, L.B., “Visualization and Wake Surveys of Vortical Flow over a Delta Wing,” *AIAA Journal*, Vol. 26, no. 2, pp. 137–143, 1988.
- [19] Escudier, M., “Vortex Breakdown: Observations and Explanations,” *Progress in Aerospace Sciences*, Vol. 25, no. 2, pp. 189–229, 1988.
- [20] Wentz Jr., W. H., Kohlman, D. L., “Wind Tunnel Investigations of Vortex Breakdown on Slender Sharp-Edged Wings,” *NASA Contract. Rep.*, Vol. 98737, 1969.
- [21] Delery, J. M., “Aspects of Vortex Breakdown,” *Progress in Aerospace Sciences*, Vol. 30, no. 1, pp. 1–59, Jan. 1994.
- [22] Gu, W., Robinson, O., Rockwell, D., “Control of Vortices on a Delta Wing by Leading-Edge Injection,” *AIAA Journal*, Vol. 31, no. 7, 1993.
- [23] Lucca-Negro, O., O’Doherty, T. “Vortex breakdown: A review,” *Progress in Energy and Combustion Sciences*, Vol. 27, no. 4, pp. 431–481, 2001.
- [24] Hall, M. G., “Vortex Breakdown,” *Annual Review of Fluid Mechanics*, Vol. 4, no. 1, pp. 195–218, 1972.
- [25] Payne, F. M., Ng, T. T., Nelson, R. C., Schiff, L. B., “Visualization and Wake Surveys of Vortical Flow over a Delta Wing,” *AIAA Journal*, Vol. 26, no. 2, pp. 137–143, 1988.

- [26] Lambourne, N. C., Bryer, D. W., "The Bursting of Leading-Edge Vortices-Some Observations and Discussion of the Phenomenon," *Aeronautical Research Council Reports and Memoranda*, London, no. 3382, 1961.
- [27] Visbal, M. R., "Computed Unsteady Structure of Spiral Vortex Breakdown on Delta Wings," *AIAA Fluid Dynamics Conference*, Vol. 2074, no. June, pp. 96–2074, 1996.
- [28] Lawson, M. V., Riley, A. J., "Vortex Breakdown Control by Delta Wing Geometry," *Journal of Aircraft*, Vol. 32, no. 4, pp. 832–838, 1995.
- [29] Gursul, I., Xie, W., "Buffeting Flows over DeltaWings," *AIAA Journal*, Vol. 37, no. 1, 1999.
- [30] Taylor, G. S., Gursul, I., "Buffeting Flows over a Low-Sweep Delta Wing," *AIAA Journal*, Vol. 42, no. 9, pp. 1737–1745, 2004.
- [31] Ozgoren, M., Sahin, B., Rockwell, D., "Vortex Breakdown from a Pitching Delta Wing Incident Upon a Plate: Flow Structure as the Origin of Buffet Loading," *Journal of Fluids and Structures*, Vol. 16, no. 3, pp. 295–316, 2002.
- [32] Mitchell, A. M., Détery, J., "Research into Vortex Breakdown Control," *Progress in Aerospace Sciences*, Vol. 37, no. 4, pp. 385–418, 2001.
- [33] Yaniktepe, B., Rockwell, D., "Flow Structure on Diamond and Lambda Planforms : Trailing Edge Region," *AIAA Journal*, Vol. 43, no. 7, 2005.
- [34] Taylor, G., Wang, Z., Vardaki, E., Gursul, I., "Lift Enhancement over Flexible Non slender Delta Wings," *AIAA Journal*, Vol. 45, no. 12, pp. 2979–2993, Dec. 2007.

- [35] Greenwell, D. I., “Gurney Flaps on Slender and Nonslender Delta Wings,” *Journal of Aircraft*, Vol. 47, no. 2, pp. 675–681, Mar. 2010.
- [36] Collins, F. G., “Boundary-Layer Control on Wings Using Sound and Leading-Edge Serrations,” *AIAA Journal*, Vol. 19, no. 2, pp. 129–130, 1981.
- [37] Hsiao, F. B., Shyu, J. Y., Liu, C.F., “Control Of Wall-Separated Flow by Internal Acoustic Excitation,” *AIAA Journal*, Vol. 28, no. 8, pp. 1440–1446, Aug. 1990.
- [38] Zaman, K. B. M. Q., “Effect Of Acoustic Excitation on Stalled Flows over an Airfoil,” *AIAA Journal*, Vol. 30, no. 6, pp. 1492–1499, Jun. 1992.
- [39] Wood, N. J., Roberts, L., Celik, Z., “Control of Asymmetric Vortical Flows over Delta Wings at High Angles of Attack,” *Journal of Aircraft*, Vol. 27, no. 5, pp. 429–435, 1990.
- [40] Greenwell, D. I., Wood, N. J., “Roll Moment Characteristics of Asymmetric Tangential Leading-Edge Blowing on a Delta Wing,” *Journal of Aircraft*, Vol. 31, no. 1, pp. 161–168, 1994.
- [41] Ferman, M. A., Huttsell, L. J., Turner, E. W., “Experiments with Tangential Blowing to Reduce Buffet Response on an F-15 Model,” *Journal of Aircraft*, Vol. 41, no. 4, pp. 903–910, Jul. 2004.
- [42] Williams, N. M., Wang, Z., Gursul, I., “Active Flow Control on a Nonslender Delta Wing,” *Journal of Aircraft*, Vol. 45, no. 6, pp. 2100–2110, Nov. 2008.
- [43] Kölzsch, A., Breitsamter, C., “Vortex-Flow Manipulation on a Generic

- Delta-Wing Configuration,” *Journal of Aircraft*, Vol. 51, no. 5, pp. 1380–1390, Sep. 2014.
- [44] Vorobieff, P. V., Rockwell, D. O., “Vortex Breakdown on Pitching Delta Wing: Control by Intermittent Trailing-Edge Blowing,” *AIAA Journal*, Vol. 36, no. 4, pp. 585–589, Apr. 1998.
- [45] Yavuz, M. M., Rockwell, D., “Control of Flow Structure on Delta Wing with Steady Trailing-Edge Blowing,” *AIAA Journal*, Vol. 44, no. 3, pp. 493–501, 2006.
- [46] Jiang, P., Wang, Z., Gursul, I., “Effects of Unsteady Trailing-Edge Blowing on Delta Wing Aerodynamics,” *Journal of Aircraft*, Vol. 47, no. 2, pp. 591–602, Mar. 2010.
- [47] Johari, H., Olinger, D. J., Fitzpatrick, K. C., “Delta Wing Vortex Control via Recessed Angled Spanwise Blowing,” *Journal of Aircraft*, Vol. 32, no. 4, pp. 804–810, 1995.
- [48] Johari, H., Moreira, J., “Delta Wing Vortex Manipulation Using Pulsed and Steady Blowing During Ramp-Pitching,” *Journal of Aircraft*, Vol. 33, no. 2, pp. 304–310, 1996.
- [49] Sreenatha, A. G., Ong, T. K., “Wing Rock Suppression Using Recessed Angle Spanwise Blowing,” *Journal of Aircraft*, Vol. 39, no. 5, pp. 900–903.
- [50] Cui, Y. D., Lim, T. T., Tsai, H. M., “Control of Vortex Breakdown over a Delta Wing Using Forebody Spanwise Slot Blowing,” *AIAA Journal*, Vol. 45, no. 1, pp. 110–117, Jan. 2007.

- [51] Kuo, C. H., Lu, N. Y., Lin, D. C., “Evolution of Vortical Structure over Delta-Wing with Transient Along-Core Blowing,” *AIAA Journal*, Vol. 35, no. 4, pp. 617–624, Apr. 1997.
- [52] Parmenter, K., Rockwell, D., “Transient Response of Leading Edge Vortices to Localized Suction,” *AIAA Journal*, Vol. 28, no. 6, pp. 1131–1133, 1990.
- [53] McCormick, S., Gursul, I., “Effect of Shear-Layer Control on Leading-Edge Vortices,” *Journal of Aircraft*, Vol. 33, no. 6, pp. 1087–1093, 1996.
- [54] Badran, B., McCormick, S., Gursul, I., “Control of Leading Edge Vortices with Suction,” *Journal Aircraft*, Vol. 35, no. 1, pp. 163–165, 1997.
- [55] Helin, H. E., Watry, C. W., “Effects of Trailing-Edge Jet Entrainment on Delta Wing Vortices,” *AIAA Journal*, Vol. 32, no. 4, pp. 802–804, Apr. 1994.
- [56] Wang, Z. J., Jiang, P., Gursul, I., “Effect of Thrust-Vectoring Jets on Delta Wing Aerodynamics,” *Journl of Aircraft*, Vol. 44, no. 6, pp. 1877–1888, Nov. 2007.
- [57] Hong, J. S., Celik, Z. Z., Roberts, L., “Effects of Leading Edge Lateral Blowing on Delta Wing Aerodynamics,” *AIAA Journal*, Vol. 34, no. 12, pp. 2471–2478, Dec. 1996.
- [58] Bradley, R. G., Wray, W. O., “A Conceptual Study of Leading-Edge-Vortex Enhancement by Blowing,” *Journal of Aircraft*, Vol. 11, no. 1, pp. 33–38, 1974.
- [59] Mitchell, A. M., Barberis, D., Molton, P., Jean, D., “Oscillation of Vortex

- Breakdown and Blowing Control of Time-Averaged Location,” *AIAA Journal*, Vol. 38, no. 5, pp. 793–803, 2000.
- [60] Klute, S. M., Rediniotis, O. K., Telionis, D. P., “Flow Control over a Maneuvering Delta Wing at High Angles of Attack,” *AIAA Journal*, Vol. 34, no. 4, pp. 662–668, Apr. 1996.
- [61] Deng, Q., Gursul, I., “Vortex Breakdown over a Delta Wing with Oscillating Leading Edge Flaps,” *Experiments in Fluids*, Vol. 23, no. 4, pp. 347–352, Aug. 1997.
- [62] Wang, J. J., Li, Y. C., Choi, K. S., “Gurney Flap—Lift Enhancement, Mechanisms and Applications,” *Progress in Aerospace Sciences*, Vol. 44, no. 1, pp. 22–47, Jan. 2008.
- [63] Kearney, J. M., Glezer, A., “Aerodynamic Control Using Distributed Bleed,” *6th AIAA Flow Control Conference*, 2012, no. June, pp. 1–17.
- [64] Lachmann, G., “Results of Experiments with Slotted Wings,” *Technical Memorandums National Advisory Committee for Aeronautics*, no. 232 1924.
- [65] Tanner, M., “Reduction of Base Drag,” *Progress in Aerospace Sciences*, Vol. 16, no. 4, pp. 369–384, 1975.
- [66] Hunter, C. A., Viken, S. A., Wood, R. M., Bauer, S. X. S., “Advanced Aerodynamic Design of Passive Porosity Control Effectors,” in *39th AIAA Aerospace Sciences Meeting & Exhibit*, 2001, no. January.
- [67] Carpenter, P. W., Porter, L. J., “Effects of Passive Porous Walls on Boundary-Layer Instability,” *AIAA Journal*, Vol. 39, no. 4, pp. 597–604, 2001.

- [68] Hemscht, M. J., Bauer, S. X. S., “Alleviation of Side Force on Tangent-Ogive Forebodies Using Passive Porosity,” *Journal of Aircraft*, Vol. 31, no. 2, pp. 354–361, 1994.
- [69] Hu, T., Wang, Z., Gursul, I., “Passive Control of Roll Oscillations of Low-Aspect-Ratio Wings Using Bleed,” *Experiments in Fluids*, Vol. 55, no. 6, 2014.
- [70] Bhushan, B., “Biomimetics: Lessons from Nature-an Overview,” *Philosophical Transactions of the Royal Society A: Mathematical, Physical and Engineering Sciences*, Vol. 367, no. 1893, pp. 1445–1486, 2009.
- [71] Shyy, W., Lian, Y., Tang, J., Vheru, D., Liu, H., “Aerodynamics of Low Reynolds Number Flyers,” Cambridge Univ Press, 2008.
- [72] Fish, F. E. , “Biomechanical Perspective on the Origin of Cetacean Flukes,” *Advances in Vertebrate Paleobiology*, Springer US, 1998, pp. 303–324.
- [73] Triantafyllou, M. S., Triantafyllou, G. S., “An Efficient Swimming Machine,” *Scientific American*, pp. 64–71, 1995.
- [74] Fish, F. E., Rohr, J. J., “Review of Dolphin Hydrodynamics and Swimming Performance,” *SPAWAR Systems Center Technical Report*, no. 1801, San Diego, 1999.
- [75] Vogel, S., “Life in Moving Fluids- The Physical Biology of Flow,” Princeton University Press, 1994.
- [76] Alexander, R. M., “Principles of animal locomotion,” Princeton University Press, 2013.

- [77] Miklosovic, D. S., Murray, M. M., Howle, L. E., Fish, F. E., “Leading-edge tubercles delay stall on humpback whale (*Megaptera novaeangliae*) flippers,” *Physics of Fluids*, Vol. 16, no. 5, p. L39, 2004.
- [78] Miklosovic, D. S., Murray, M. M., Howle, L. E., “Experimental Evaluation of Sinusoidal Leading Edges,” *Journal of Aircraft*, Vol. 44, no. 4, pp. 1404–1408, Jul. 2007.
- [79] Goruney, T., Rockwell, D., “Flow Past a Delta Wing with a Sinusoidal Leading Edge: Near-Surface Topology and Flow Structure,” *Experiments in Fluids*, Vol. 47, no. 2, pp. 321–331, May 2009.
- [80] Chen, H., Wang, J. J., “Vortex Structures for Flow over a Delta Wing with Sinusoidal Leading Edge,” *Experiments in Fluids*, Vol. 55, pp. 1761-1770, Jun. 2014.
- [81] Triantafyllou, M. S., Techet, A. H., Hover, F. S., “Review of Experimental Work in Biomimetic Foils,” *IEEE Journal of Oceanic Engineering*, Vol. 29, no. 3, pp. 585–594, 2004.
- [82] Fish, F. E., Nusbaum, M. K., Beneski, J. T., Ketten, D. R., “Passive Cambering and Flexible Propulsors : Cetacean Flukes,” *Bioinspiration & Biomimetics*, Vol. 1, no. 4, 2006.
- [83] Fish, F. E., Lauder, G. V., “Passive and Active Flow Control By Swimming Fishes and Mammals,” *Annual Review of Fluid Mechanics*, Vol. 38, no. 1, pp. 193–224, Jan. 2006.
- [84] Fish, F. E., Howle, L. E., Murray, M. M., “Hydrodynamic Flow Control in Marine Mammals.,” *Integrative and Comparative Biology*, Vol. 48, no. 6, pp. 788–800, Dec. 2008.

- [85] Fontanella, J. E., Fish, F. E., Rybczynski, N., Nweeia, M. T., Ketten D. R., “Three-Dimensional Geometry of the Narwhal (*Monodon Monoceros*) Flukes in Relation to Hydrodynamics,” *Marine Mammal Science*, Vol. 27, no. 4, pp. 889–898, Oct. 2011.
- [86] Gursul, I., Cleaver, D. J., Wang, Z., “Control of Low Reynolds Number Flows by Means of Fluid–Structure Interactions,” *Progress in Aerospace Sciences*, Vol. 64, pp. 17–55, 2014.
- [87] Fish, F. E., Howle, L. E., Murray, M. M., “Hydrodynamic Flow Control in Marine Mammals,” *Integrative and Comparative Biology*, Vol. 48, no. 6, pp. 788–800, Dec. 2008.
- [88] Katz, J., Weihs, D., “Hydrodynamic Propulsion by Large Amplitude Oscillation of an Airfoil with Chordwise Flexibility,” *Journal of Fluid Mechanics*, Vol. 88, no. 3, pp. 485–497, 1978.
- [89] Bose, N., Lien, J., “Propulsion of a Fin Whale (*Balaenoptera physalus*): Why the Fin Whale is a Fast Swimmer,” *Proceedings of the Royal Society B: Biological Sciences*, Vol. 237, no. 1287, 1989.
- [90] Swartz, S. M., Bennett, M. B., Carrier, D. R., “Wing Bone Stresses in Free Flying Bats and the Evolution of Skeletal Design for Flight,” *Nature*, Vol. 359, no. 6397, pp. 726–729, Oct. 1992.
- [91] Muijres, F. T., Johansson, L. C., Barfield, R., Wolf, M., Spedding, G. R., Hedenström, A., “Leading-Edge Vortex Improves Lift in Slow Flying Bats,” *Science*, Vol. 319, 2008.
- [92] Leylek, E. A., Manzo, J. E., Garcia, E., “Bat-Inspired Wing Aerodynamics and Optimization,” *Journal of Aircraft*, Vol. 47, no. 1, pp. 323–328, 2010.

- [93] Song, A., Tian, X., Israeli, E., Galvao, R., Bishop, K., Swartz, S., Breuer, K., “Aeromechanics of Membrane Wings with Implications for Animal Flight,” *AIAA Journal*, Vol. 46, no. 8, pp. 2096–2106, 2008.
- [94] Rojratsirikul, P., Wang, Z., Gursul, I., “Unsteady Aerodynamics of Membrane Airfoils,” *46th AIAA Aerospace Sciences Meeting and Exhibit*, Reno, 2008.
- [95] Stanford, B., Ifju, P., Albertani, R., Shyy, W., “Fixed Membrane Wings for Micro Air Vehicles: Experimental Characterization, Numerical Modeling, and Tailoring,” *Progress in Aerospace Sciences*, Vol. 44, no. 4, pp. 258–294, 2008.
- [96] Heathcote, S., Wang, Z., Gursul, I., “Effect of Spanwise Flexibility on Flapping Wing Propulsion,” *Journal of Fluids and Structures*, Vol. 24, no. 2, pp. 183–199, 2008.
- [97] Gray, J., Gursul, I., Butler, R., “Aeroelastic Response of a Flexible Delta Wing due to Unsteady Vortex Flows, AIAA 2003-1106,” *41th AIAA Aerospace Sciences Meeting and Exhibit*, Reno, 2003.
- [98] Lucas, K. N., Johnson, N., Beaulieu, W. T., Cathcart, E., Tirrell, G., Colin, S. P., Gemmell, B. J., Dabiri, J. O., Costello, J. H., “Bending Rules for Animal Propulsion,” *Nature Communications*, Vol. 5, no. May 2013, p. 3293, Jan. 2014.
- [99] Gursul, I., “Origin of Vortex Wandering over Delta Wings,” *Journal of Aircraft*, Vol. 37, no. 2, pp. 1996–1998, 1999.
- [100] Nelson, R. C., Pelletier, A., “The Unsteady Aerodynamics of Slender Wings and Aircraft Undergoing Large Amplitude Maneuvers,” *Progress in*

Aerospace Sciences, Vol. 39, no. 2–3, pp. 185–248, Feb. 2003.

- [101] Fish, F. E., “Biomechanical Perspective on the Origin of Cetacean Flukes,” *Advances in Vertebrate Paleobiology*, Vol. 1, J. G. M. Thewissen, Ed. Springer US, 1998, pp. 303–324.
- [102] Waszak, M. R., Jenkins, L. N., Ifju, P., “Stability and Control Properties of an Aeroelastic Fixed Wing Micro Aerial Vehicle,” *Atmospheric Flight Mechanics Conference and Exhibit*, Montreal, Aug. 2001.
- [103] Adrian, R. J., “Particle-Image Techniques for Experimental Fluid Mechanics,” *Annu. Rev. Fluid Mech.*, Vol. 23, pp. 261–304, 1991.
- [104] Tropea, C., Yarin, A., Foss, J. F., Eds., “*Springer Handbook of Experimental Fluid Mechanics*, ” 1st ed. Springer-Verlag Berlin Heidelberg, 2007.
- [105] Ozgoren, M., Sahin, B., Rockwell, D., “Perturbations of a Delta Wing : Control,” *Journal of Aircraft*, Vol. 38, no. 6, pp. 1040–1050, 2001.
- [106] Kline, S. J., McClintock, F. A., “Describing Uncertainties in Single-Sample Experiments,” *Mechanical Engineering*, Vol.75, no. 1, pp. 3-8, Jan. 1953.
- [107] Bose, N., Lien, J., Ahia, J., “Measurements of the Bodies and Flukes of Several Cetacean Species,” *Proceedings of the Royal Society B: Biological Sciences*, Vol. 242, no. 1305, pp. 163–173, Dec. 1990.
- [108] Yaniktepe, B., Rockwell, D., “Flow Structure on a Delta Wing of Low Sweep Angle,” *AIAA Journal*, Vol. 42, no. 3, pp. 513–523, Mar. 2004.

- [109] Zharfa, M., Ozturk, I., Yavuz, M. M., “Flow Structure on Nonslender Delta Wing: Reynolds Number Dependence and Flow Control,” *AIAA Journal*, pp. 1–18, 2016.
- [110] Cai, J., Pan, S., Li, W., Zhang, Z., “Numerical and Experimental Investigations of a Nonslender Delta Wing with Leading-Edge Vortex Flap,” *Computers & Fluids*, Vol. 99, pp. 1–17, Jul. 2014.
- [111] Massey, K., Flick, A., Jadhav, G., “Force Measurements and Flow Visualization for a Flexible Flapping Wing Mechanism,” *47th AIAA Aerospace Sciences Meeting Including The New Horizons Forum and Aerospace Exposition*, Orlando, 2009.

APPENDIX A

PIV RESULTS FOR BLEED EXPERIMENTS AT $Re = 3.5 \times 10^4$

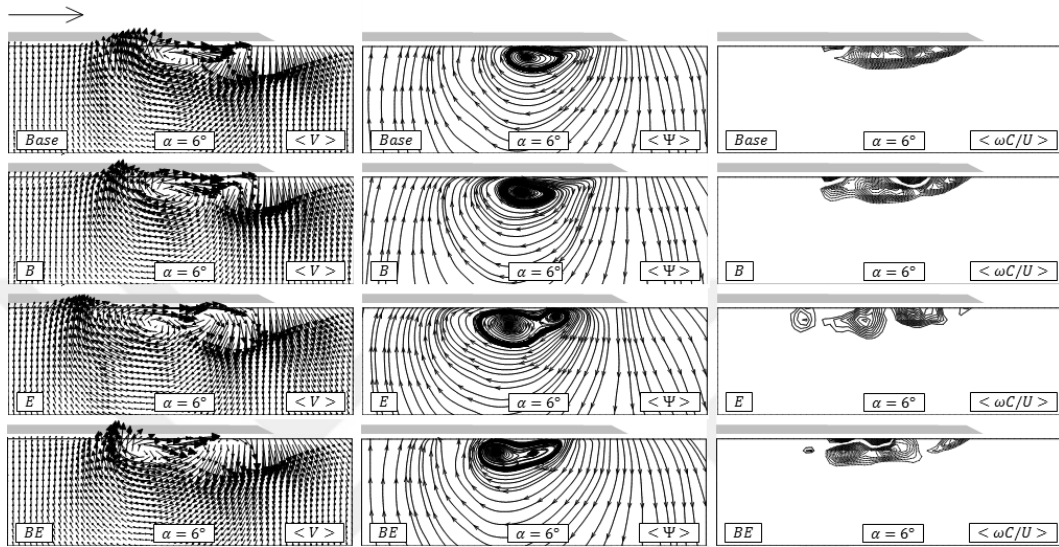


Figure A 1 Patterns of time-averaged velocity vectors $\langle V \rangle$, streamlines $\langle \Psi \rangle$ and constant contours of non-dimensional axial vorticity $\langle \omega C/U \rangle$ at angle of attack $\alpha = 6$ deg for $Re = 3.5 \times 10^4$: $[\langle \omega C/U \rangle]_{min} = 7$, $\Delta[\langle \omega C/U \rangle] = 2$.

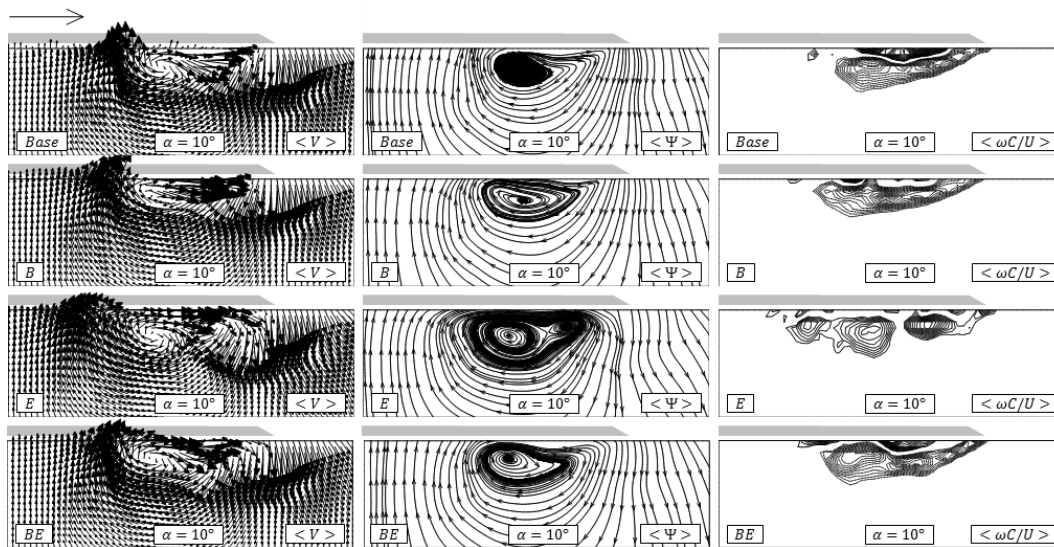


Figure A 2 Patterns of time-averaged velocity vectors $\langle V \rangle$, streamlines $\langle \Psi \rangle$ and constant contours of non-dimensional axial vorticity $\langle \omega C/U \rangle$ at angle of attack $\alpha = 10$ deg for $Re = 3.5 \times 10^4$: $[\langle \omega C/U \rangle]_{min} = 7$, $\Delta[\langle \omega C/U \rangle] = 2$.

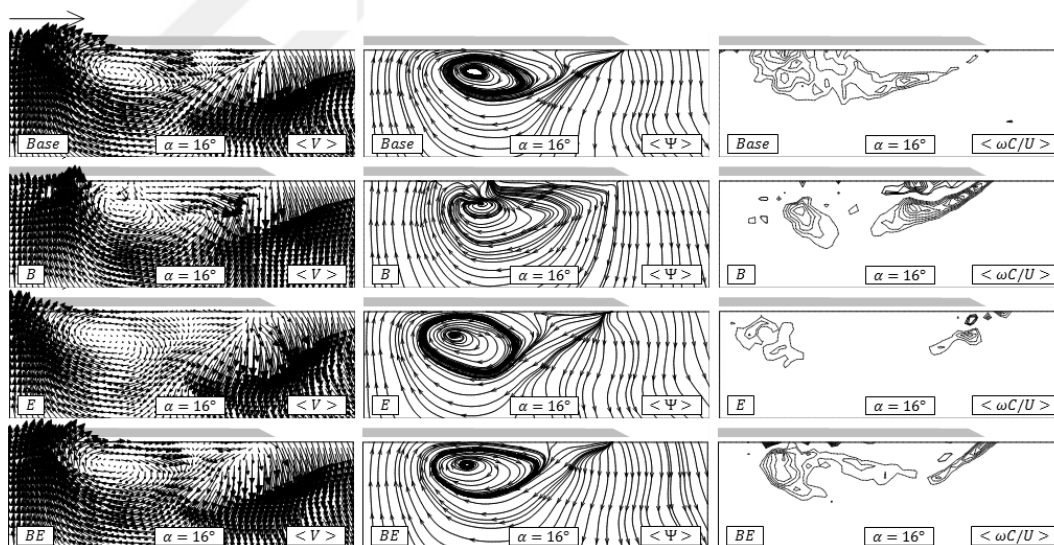


Figure A 3 Patterns of time-averaged velocity vectors $\langle V \rangle$, streamlines $\langle \Psi \rangle$ and constant contours of non-dimensional axial vorticity $\langle \omega C/U \rangle$ at angle of attack $\alpha = 16$ deg for $Re = 3.5 \times 10^4$: $[\langle \omega C/U \rangle]_{min} = 7$, $\Delta[\langle \omega C/U \rangle] = 2$.

APPENDIX B

PRESSURE MEASUREMENT RESULTS FOR BLEED EXPERIMENTS

AT $Re = 1.5 \times 10^4, 2 \times 10^4, 5 \times 10^4$ AND 7.5×10^4

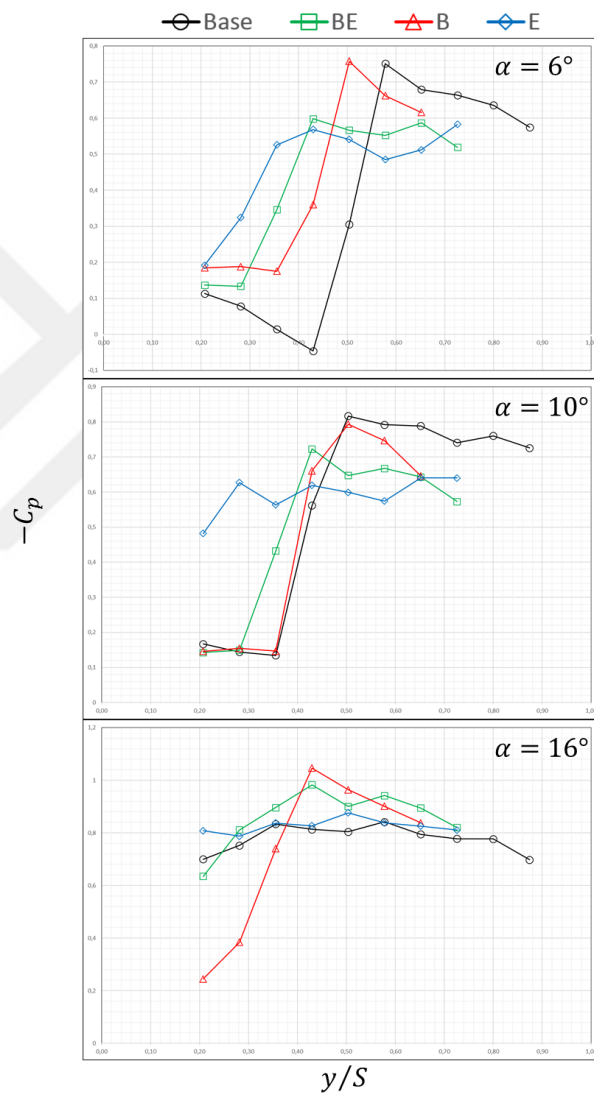


Figure B 1 $-C_p$ distributions of half span Base, B, E and BE planforms at angle of attacks $\alpha = 6, 10$ and 16 deg at $Re = 1.5 \times 10^4$.

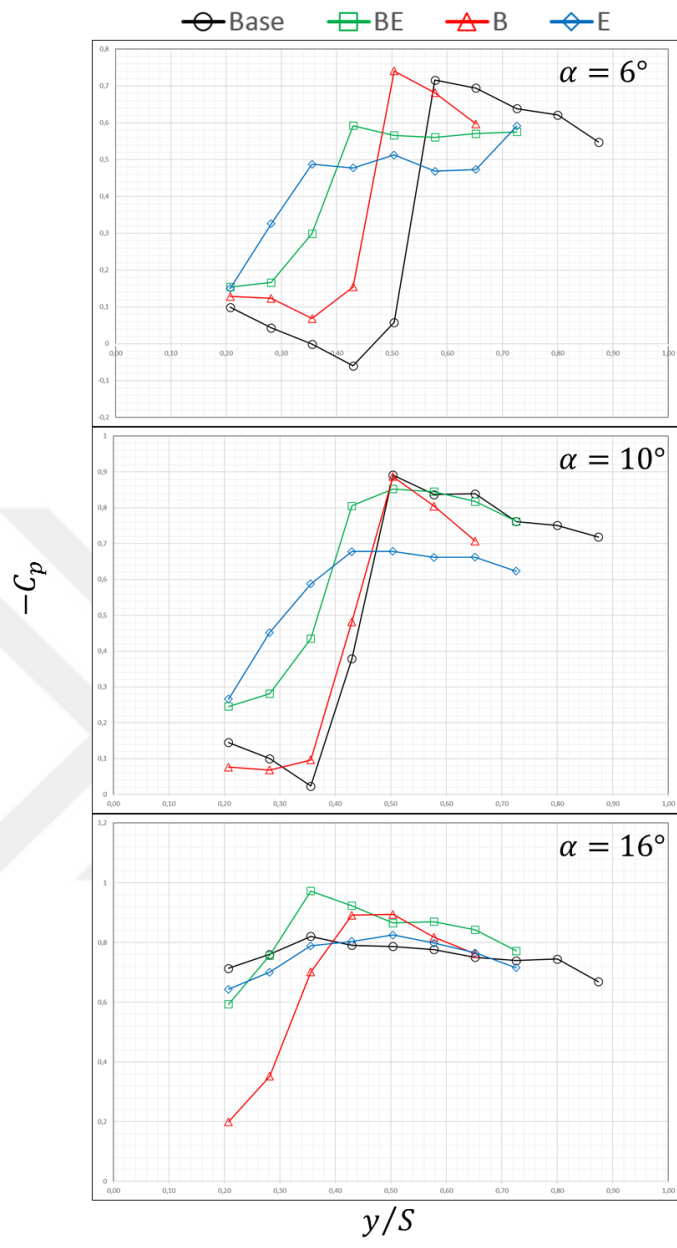


Figure B 2 $-C_p$ distributions of half span Base, B, E and BE planforms at angle of attacks $\alpha = 6, 10$ and 16 deg at $Re = 2 \times 10^4$.

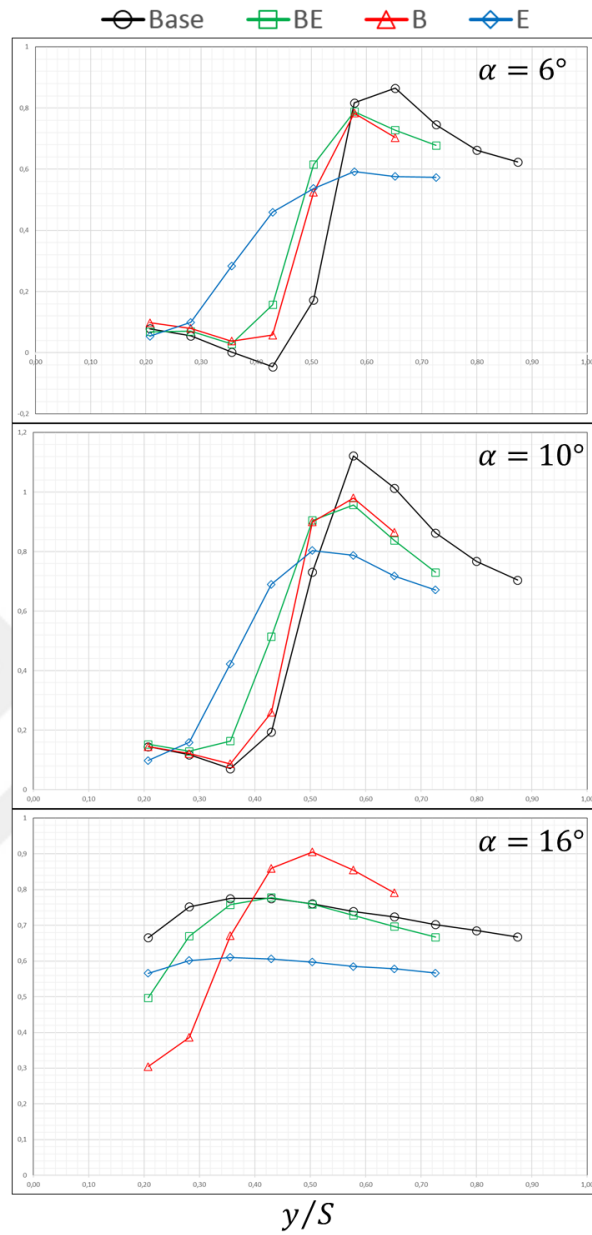


Figure B 3 $-C_p$ distributions of half span Base, B, E and BE planforms at angle of attacks $\alpha = 6, 10$ and 16 deg at $Re = 5 \times 10^4$.

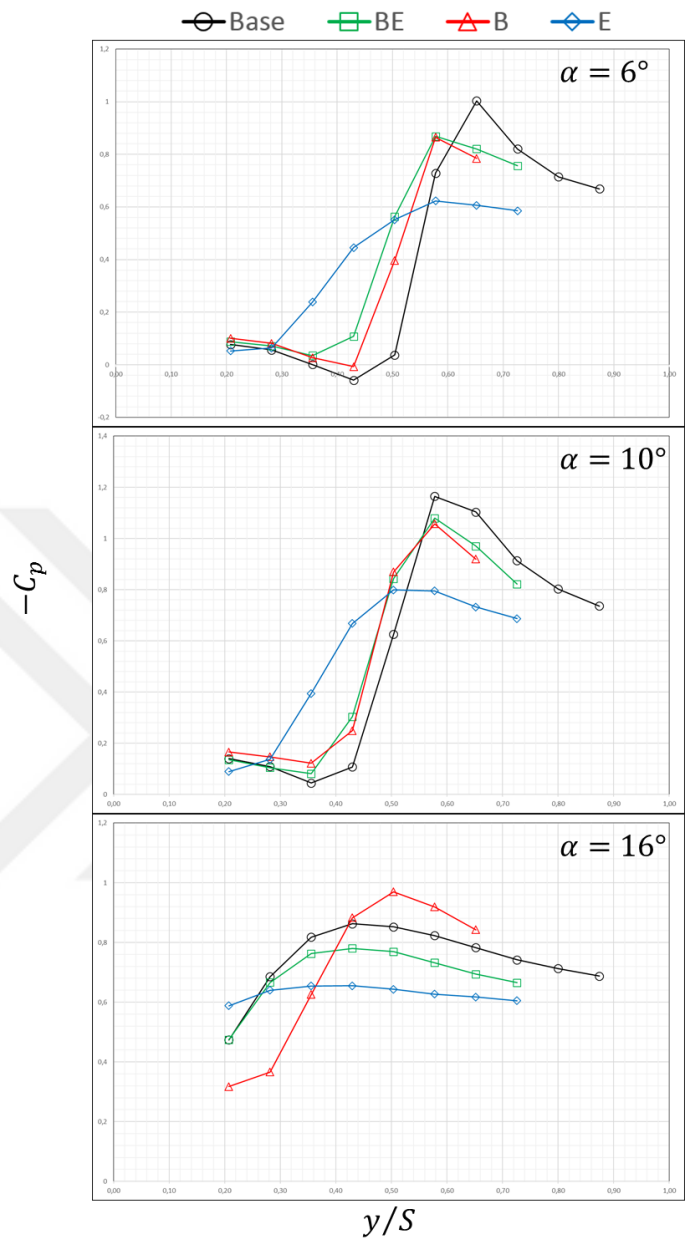


Figure B 4 $-C_p$ distributions of half span Base, B, E and BE planforms at angle of attacks $\alpha = 6, 10$ and 16 deg at $Re = 7.5 \times 10^4$.

APPENDIX C

SOURCE CODES FOR PRESSURE COEFFICIENT CALCULATION

```
clear all;
close all;
clc;
addpath ./TestFilesBase
%=====
%=====
MS = 12; FS =20; LW =2.0;
% Number of Samples for the DataSet
NSamples = 2;
% %

[Channel] = ReadChannelInfoBase();

ChannelMax = max(Channel.Number);
% %

alpha = [10];
Reynolds = [20,35,50,75,100];
Cu = [0];
% % %
% NoiseBase61 = ReadData(6,0,0,1);
% NoiseBase62 = ReadData(6,0,0,2);
NoiseBase101 = ReadData(10,0,0,1);
NoiseBase102 = ReadData(10,0,0,2);
% NoiseBase161 = ReadData(16,0,0,1);
% NoiseBase162 = ReadData(16,0,0,2);

% MNBase61 = mean(NoiseBase61(:,2:end),1);
% MNBase62 = mean(NoiseBase62(:,2:end),1);
% NFBase6=(MNBase61+MNBase62)/2;

MNBase101 = mean(NoiseBase101(:,2:end),1);
MNBase102 = mean(NoiseBase102(:,2:end),1);
NFBase10=(MNBase101+MNBase102)/2;

% MNBase161 = mean(NoiseBase161(:,2:end),1);
% MNBase162 = mean(NoiseBase162(:,2:end),1);
% NFBase16=(MNBase161+MNBase162)/2;
% % %

Na = length(alpha);
Nr = length(Reynolds);
Nc = length(Cu);
```

```

% %
ETot = NSamples*Na*Nr*Nc ;
% %

for i=1:Na
    for j=1:Nr
        for k=1:Nc

            for s = 1:NSamples
%
                a = alpha(i);
                r = Reynolds(j);
                c = Cu(k);
%
                fprintf('Reading Alpha = %d\tReynolds=%d\t Cu=%d\t Sample =
%d \n', a,r,c, s);
                DataBase = ReadData(a,r,c,s);

                if (a==6)
                    DataMean = mean(DataBase(:,2:end),1) - NFBase6;
                elseif (a==10)
                    DataMean = mean(DataBase(:,2:end),1) - NFBase10;
                elseif (a==16)
                    DataMean = mean(DataBase(:,2:end),1) - NFBase16;
                end

                % % % %
                DATABase{i,j,k}.Mean(s,:) = DataMean;
                if(s==1)
                    DATABase{i,j,k}.MeanTotal = DataMean;
                else
                    DATABase{i,j,k}.MeanTotal =
DATABase{i,j,k}.MeanTotal + DataMean;
                end

            end

            DATABase{i,j,k}.MeanTotal =
DATABase{i,j,k}.MeanTotal/ NSamples;

            MeanTotal = DATABase{i,j,k}.MeanTotal;

            for dataDotBase=1:ChannelMax
                DATABase{i,j,k}.Cp(dataDotBase) = (
MeanTotal(ChannelMax+1)- MeanTotal(dataDotBase) )...
                / (
MeanTotal(ChannelMax+2)- MeanTotal(ChannelMax+1) );
            end
        end
    end
end
end

```

```

end
% % % % % % % % % % % % % % % % % % % % % % % % % % % % % %
% % % % % % %

Station1 = Channel.Station == 1;
% Station2 = Channel.Station == 2;
% % %
% % % % % % % % % % % % % % % % % % % % % % % % % % % % % %
% % % % % % %

% % % % % % % % % % % % % % % % % % % % % % % % % % % % % %
% % % % % % %
%Symbols = ['d','o','s','v'];
linestyles = cellstr(char('-', '-', '-', '-', '-'));
n=length(alpha) ;
MarkerEdgeColors=jet(n); % n is the number of different
items you have
Markers=['o','d','v','s','*'];
Color=['b','b','b','b','b'];
% % % % % % % % % % % % % % % % % % % % % % % % % % % % % %
% % % % % % %
fgh = figure (1);
title('Station-1/ Effect of Bleeding at Different Angle of
Attacks at Re=8000')
fs=20;
% Specify Size of Figure
FigureSize = [4.0,4.0,16.0,16.0];
set(fgh,'Units','centimeters ');
set(fgh, 'Position', FigureSize);
% Set X axis Limit
set(gca,'XLim',[0.0 1]);set(gca,'FontSize',fs-4);
set(gca,'YLim',[-0.5 4]);
% set(gca,'YTick',[-0.2:0.2:2.0]);
% set(gca,'YTickLabel',[-0.2:0.2:2.0]);
xlabel('$$\bf{y/s}
}$$','interpreter','latex','FontSize',fs+2);
ylabel('$$\bf{-C_p}
}$$','interpreter','latex','FontSize',fs+2);

hold on;
for a=1:length(Reynolds)
plot(Channel.x(Station1),
DATABase{1,a,1}.Cp(Station1),[linestyles{a} Markers(a)
Color(a)], 'MarkerSize',MS,'LineWidth',LW);
end

linestyles = cellstr(char('--', '--', '--', '--', '--'));
Color=['r','r','r','r','r'];

```

```

% for a=1:length(alpha)
% plot(Channel.x(Station1),
DATABase{a,1,1}.Cp(Station1),[linestyles{a} Markers(a)
Color(a)], 'MarkerSize',MS, 'LineWidth',LW);
% end
% % % % % % % % % % % % % % % % % % % % % % % % % % % % %
% % % % % %
DATABase{2,1,1}.Cp(Station1)
DATABase{2,2,1}.Cp(Station1)
DATABase{2,3,1}.Cp(Station1)
DATABase{2,4,1}.Cp(Station1)
DATABase{2,5,1}.Cp(Station1)

% fgh = figure (2);
% title('Station-2/ Effect of Bleeding at Different Angle of
Attacks at Re=8000')
% fs=20;
% % Specify Size of Figure
% FigureSize = [4.0,4.0,16.0,16.0];
% set(fgh, 'Units', 'centimeters ');
% set(fgh, 'Position', FigureSize);
% % Set X axis Limit
% set(gca, 'XLim', [0.0 0.8]);set(gca, 'FontSize', fs-4);
% set(gca, 'YLim', [-0.5 1.5]);
% % set(gca, 'YTick', [-0.2:0.2:2.0]);
% % set(gca, 'YTickLabel', [-0.2:0.2:2.0]);
% xlabel('$$\bf{y/s}
$$', 'interpreter', 'latex', 'FontSize', fs+2);
% ylabel('$$\bf{-C_p}
$$', 'interpreter', 'latex', 'FontSize', fs+2);
% Color =['b', 'b', 'b', 'b', 'b'];
% hold on;
% for a=1:length(alpha)
% plot(Channel.x(Station2),
DATA{a,1,1}.Cp(Station2), [linestyles{a} Markers(a)
Color(a)], 'MarkerSize',MS, 'LineWidth',LW);
% end
%
% linestyles = cellstr(char('--', '--', '--', '--', '--'));
% Color=['r', 'r', 'r', 'r', 'r'];
%
% for a=1:length(alpha)
% plot(Channel.x(Station2),
DATA{a,1,2}.Cp(Station2), [linestyles{a} Markers(a)
Color(a)], 'MarkerSize',MS, 'LineWidth',LW);
% end

```

```
pause(0.5);
```

```
Channel
```

```
function [Channel] = ReadChannelInfoBase()  
%===== %  
% TODO  
skData = 1;  
    [fid, message]=fopen('Channels_BASE.txt','r');  
    %  
    for i =1:1  
        line = fgetl(fid);  
    end  
    %  
    sk=1;  
    line = fgetl(fid);  
    while(line~-=-1)  
        line = str2num(line);  
        %  
        Data(sk,:) = line;  
        sk = sk+1;  
        line = fgetl(fid);  
    end  
    % %  
    [r, c] = size(Data);  
    Nc = r;  
  
    Channel.Station = Data(:,1);  
    Channel.Number = Data(:,2);  
    Channel.x = Data(:,3);  
  
end
```

```
DATA
```

```
function [Data] = ReadData(a,r)  
% %  
as = num2str(a);  
rs = num2str(r);  
% rs = num2str(r);  
% cs = num2str(c);
```

```

% m öss = num2str(s);
% %

B000000.T000.D000.P000.H000.L.vec

filename = strcat('B00000',as, '.T000.D000.P000.H000.L.vec');

[fid, message]=fopen(filename,'r');
%
for i =1:14
    line = fgetl(fid);
end
%

sk=1;
line = fgetl(fid);
while(line~-=-1)
    line = strrep(line, ',', '.'); line =
str2num(line);
%
    Data(sk,:) = line;
    sk = sk+1;
    line = fgetl(fid);
end
fclose(fid);
end

```

SOURCE CODES FOR VRMS CALCULATION

```
clear all
clc
addpath ./TestFilesBase

fileNumber = 0:199;

str1 = 'BE000';
str2 = '.T000.D000.P000.H000.L.vec';
str0 = '0';

for i=1:200
    if i<11
        fileNames{i} =
strcat(str1,str0,str0,num2str(fileNumber(i)),str2);
    end

    if i>10 && i<101
        fileNames{i} =
strcat(str1,str0,num2str(fileNumber(i)),str2);
    end

    if i > 100
        fileNames{i} =
strcat(str1,num2str(fileNumber(i)),str2);
    end
end

for i=1:200
    [fid, message]=fopen(fileNames{i},'r');
    %
    line = fgetl(fid);
    %
    sk=1;
    line = fgetl(fid);
    while(line~=-1)
        line = strrep(line, ',',' '); line = str2num(line);
        %
        Data(i,sk,:) = line;
        sk = sk+1;
        line = fgetl(fid);
    end
    fclose(fid);
end
```

```

for i=1:size(Data,2)
    meanUV(i,1) = mean(Data(:,i,3)); % u'nun mean'i
    meanUV(i,2) = mean(Data(:,i,4)); % v'nin mean'i
end

for i=1:size(Data,1)
    DataDiff(i,:,1) = Data(i,:,3)-meanUV(:,1)'; %difference
u-u_mean
    DataDiff(i,:,2) = Data(i,:,4)-meanUV(:,2)'; %difference
v-v_mean
end

for i=1:size(Data,1)
    DataDiffSquare(i,:,1) = DataDiff(i,:,1).^2;
%square(difference u-u_mean)
    DataDiffSquare(i,:,2) = DataDiff(i,:,2).^2;
%square(difference v-v_mean)
end

for i=1:size(Data,2)
    rmsUV(i,1) = (1/size(Data,1)) *
(sum(DataDiffSquare(:,i,1)));
    rmsUV(i,2) = (1/size(Data,1)) *
(sum(DataDiffSquare(:,i,2)));
end

figure(1)
plot(rmsUV(:,1))
figure(2)
plot(rmsUV(:,2))

count = 1;
for i=1:59
    for j=1:19
        field_rmsU(Data(1,i,j),i,j) = rmsUV(count,1);
        field_rmsV(Data(1,i,j),i,j) = rmsUV(count,2);
        count = count + 1;
    end
end

figure(3)
surf(field_rmsU)
figure(4)
surf(field_rmsV)

```

SOURCE CODES FOR VRMS CALCULATION_Converting to Tecplot File

```
function [] = TecplotWriter(X,Y,A, name,II,JJ)

U = A(:,1);
V = A(:,2);

% U = reshape(U, II, JJ);
% V = reshape(V, II, JJ);
% X = reshape(X, II, JJ);
% Y = reshape(Y, II, JJ);

file = fopen(strcat(name,'_RMS.dat'), 'w');
% %
fprintf(file, '%s %s %s', 'TITLE = "', name, '"');
fprintf(file, '%s', 'VARIABLES = "x", "y", "Urms", "Vrms"');
fprintf(file, '%s %s %i %s %i %s\n', 'ZONE T="ZONE 001"', ' ',
I=',II,', J=', JJ, ', F=POINT');

% for i = 1:II
%     for j=1:JJ
%         fprintf(file,
'%.10f\t%.10f\t%.10f\t%.10f\n',X(i,j),Y(i,j),U(i,j),V(i,j));
%     end
% end

for i = 1:II*JJ
    fprintf(file,
'%.10f\t%.10f\t%.10f\t%.10f\n',X(i),Y(i),U(i),V(i));
end

fclose(file);

end
```



CURRICULUM VITAE

CONTACT INFORMATION

Address : Mechanical Eng Department / METU

Mobile Phone : +90 537 672 21 59

E-mail : alper.celik@metu.edu.tr

EDUCATION

2012-2017 PhD, METU- Mechanical Engineering Department

Development and Implementation of Novel Flow Control Techniques on Nonslender Delta Wings

2008-2011 MSc, METU- Mechanical Engineering Department

Experimental and Numerical Investigation on Fire in Tunnels

2003-2008 BS, METU- Mechanical Engineering Department

JOURNAL PUBLICATIONS

- 1- **Çelik, A.**, Yavuz, M. M.,” Effect of Edge Modifications on Flow Structure of Low Swept Delta Wing”, *AIAA Journal Vol. 54, No.5, 2016.*
- 2- **Çelik, A.**, Çetin, C., Yavuz, M. M., “Effect of Passive Bleeding on Flow Structure over a Nonslender Delta Wing”, *In print -AIAA Journal.*
- 3- Çetin, C., **Çelik, A.**, Yavuz, M. M., “Control of Flow Structure over a Nonslender Delta Wing Using Periodic Blowing”, *under review- AIAA Journal.*

- 4- **Çelik, A.**, Yavuz, M.M., “Flow Control on Nonslender Delta Wings by Bio-inspired Flexion Ratio Applications”, in preparation.

PRESENTATIONS

- 1- **Çelik, A.**, Öztürk, I., Tunc, H. C. and Yavuz, M. M., 2012, “Flow Structure on a Delta Wing of Moderate Sweep Angle During and After Pitch-Up Maneuver”, APS 2012, San Diego, CA, US.
- 2- Yavuz, M. M., **Çelik, A.**, Çetin, C., “Control of Flow Structure on Non-Slender Delta Wing: Bio-inspired Edge Modifications, Passive Bleeding, and Pulsed Blowing”, APS 2016, Portland, OR, US.

NATIONAL CONFERENCE

- 1- Öztürk, I., **Çelik, A.**, Tunc, H. C. and Yavuz, M. M., 2012, “Orta Süpürme Açısına Sahip Delta Kanat Üzerindeki Akış Yapısının Kalkış Manevrası Sırasında Değişimi”, UHUK 2012 (National Aeronautical and Aerospace Conference), Istanbul.
- 2- **Çelik, A.**, Çetin, C., Yavuz, M. M., “Kenar Değişikliklerinin Düşük Ok Açılı Delta Kanat Üzerindeki Akış Yapılarına Etkileri”, UHUK 2016, (National Aeronautical and Aerospace Conference), Kocaeli.
- 3- **Çelik, A.**, Çetin, C., Yavuz, M. M., “Düşük Ok Açılı Delta Kanat Üzerindeki Akışın Pasif Akıtma Yöntemiyle Kontrolü”, UHUK 2016 (National Aeronautical and Aerospace Conference), Kocaeli.
- 4- Çetin, C., **Çelik, A.**, Yavuz, M. M., “ Düşük Ok Açılı Delta Kanat Akışının Zamana Bağlı Üfleme Tekniği İle Kontrolü”, UHUK 2016 (National Aeronautical and Aerospace Conference), Kocaeli.

WORK EXPERIENCE

- 1- Senior Researcher at Tübitak UZAY (The Scientific and Technological Research Council of Turkey- Space Technologies Research Institute) since May 2015. Responsible for thermal testing and thermal design of high resolution camera.
- 2- Teaching and Research Assistant at METU Mechanical Engineering from 2008 to 2013. Some of the courses assisted are: *Fluid Mechanics I-II, Steam Power and Heat Exchanger Design, Thermodynamics, Turbulence and Its Measurement.*
- 3- Instructor of Computer Aided Drawing for three semesters at METU Mechanical Engineering Department.
- 4- Research associate for 1 and a half year (from 2008 to 2010) for a private company (Taru Coop.) at METU Techno polis, and involved in following projects;
 - a. “Performance Evaluation of Axial Fans and Fan Selection Software” for Emtesa Coop.(Ankara, Turkey),2009
 - b. İzmir Metro Systems (Bornova to Center Station) Emergency Ventilation System and Piston Effect Evaluation,2009
 - c. Piston effect evaluation tests in Hastane Station (in Ankara Metro System), 2008
- 5- Involved in Tubitak(The Scientific and Technological Research Research Council of Turkey) Project “Control of Flow Structure on Low Swept Delta Wing with Steady Active Flow Control Techniques”.